INFLUENCE OF MEAN STATE ON CLIMATE VARIABILITY AT

INTERANNUAL AND DECADAL TIME SCALES

A Dissertation

by

XIAOJIE ZHU

Submitted to the Office of Graduate Studies of
Texas A&M University
in partial fulfillment of the requirements for the degree of

DOCTOR OF PHILOSOPHY

Chair of Committee,	Ramalingam Saravanan
Committee Members,	Ping Chang
	Gerald R. North
	Courtney Schumacher
Head of Department,	Ping Yang

August 2013

Major Subject: Atmospheric Sciences

ABSTRACT

This dissertation reports on studies on the role of the mean state in modulating climate variability at interannual and decadal time scales. In the atmosphere, the nonlinear superposition of mean flow and anomalous flow has important implications for many phenomena associated with variables that are nonlinear by definition, such as the vertical wind shear and surface wind speed.

In the first part of this dissertation, the influence of mean flow and anomalous flow on vertical wind shear variability is studied in observations and numerical model simulations. At interannual timescales, the ENSO-shear relationship is compared between observations and numerical model simulations. It is shown that there is strong influence of mean flow on the ENSO-shear relationship. For same anomalous flow, different mean flows could give rise to a different ENSO-shear relationship. The nonlinear superposition of mean flow and anomalous flow also helps explains the dipole mode of tropical Atlantic vertical wind shear variability seen in observations and models, which implies opposite variation of vertical wind shear over the two sides of the tropical Atlantic. This has important implications for predicting phenomena such as Atlantic hurricanes, whose variations are modulated by vertical shear variability.

The dissertation also addresses the role of the mean surface wind in decadal variability and predictability, as manifested through the Wind-Evaporation-SST (WES) feedback. The nonlinear superposition of anomalous surface wind on the mean trade wind can give rise to a positive WES feedback, which can amplify tropical climate

variability. To study this feedback, we carried out ensembles of decadal climate predictions using the CAM3 atmospheric model coupled to a slab ocean model (CAM3-SOM) with prescribed ocean transport and simple extrapolative prescriptions of future external forcings. Mechansitic sensitivity runs using the CAM3-SOM were also carried out, where the WES feedback was switched off by prescribing climatological surface wind. Results suggest that switching off the WES feedback enhances the prediction skill over some regions, especially over the eastern tropical Pacific, by increasing the signal-to-noise ratio. To address the issue of cold bias noted in the decadal prediction experiments, we carried out additional sensitivity experiments where we used an *adaptive* formulation for the prescribed oceanic heat transport (Q-flux) in the slab ocean. The results from these experiments demonstrate that the mean oceanic heat transport plays a crucial role in influencing decadal predictability, by helping improve predictions of the trend component of decadal variations.

DEDICATION

To my family

ACKNOWLEDGEMENTS

I would like to give my most grateful thanks to my advisor, Dr. Saravanan, who has been a mentor for both science and scientific conduct all these years. He has been very patient in giving expert suggestions and inspirational ideas, and has always been very kind and understanding.

I would like to thank my committee members, Dr. Chang, Dr. North, and Dr. Schumacher, for their guidance and support throughout the course of this research. I would also like to thank Dr. Ji and Dr. Mahajan, who helped me at various points during my period of study.

Thanks also to my friends and colleagues and the department faculty and staff for making my time at Texas A&M University a great experience. I also want to extend my gratitude to the National Education Foundation, which provided the survey instrument, and to all the Texas elementary teachers and students who were willing to participate in the study.

Finally, last but not the least, I would like to thank my husband Bo Chen for his encouragement and love. Also I would like to thank my parents, Benqiang Zhu and Suhuai Lu, and my parents-in-law, Lejun Chen and Xiuying Zhou, for their unconditional support.

TABLE OF CONTENTS

LIST OF FIGURES

LIST OF TABLES

CHAPTER I

INTRODUCTION

There is a saying that 'Climate is what you expect and weather is what you get'. The climate describes the statistics of atmospheric variables over a long period, which can be decomposed into two parts: the climate mean and the climate variability. The climate mean, or climatology, refers to the mean state of the atmosphere over a certain time interval. For example, the winter climate in the northern hemisphere is dominated by a subpolar low-pressure belt, which includes the Icelandic low and the Aleutian low, whereas the summer climate in the northern hemisphere is dominant by subtropical anticyclones (Wallace and Hobbs, 2006). Moreover, for the precipitation averaged over decades, there is a strong precipitation belt – the InterTropical Convergence Zone (ITCZ)- over the tropical Pacific (Xie and Philander, 1994). The ITCZ is one upward branch for the Hadley circulation, which redistributes excessive heat in the tropics poleward.

Climate variability refers to the change in the mean state within a specified time interval of interest. Climate variability has been studied from intraseasonal, interannual, decadal to century timescales. At the intraseasonal time scale, the Madden-Julian Oscillation (MJO) is a dominant feature in the tropical atmosphere, which occurs at 30-60 days time scale (Madden and Julien, 1994; Wheeler and Hendon, 2004). At the interannual time scale, the Southern Oscillation, together with the El Nino and La Nina events over the ocean, describes fluctuations between the western tropical Pacific and

the southeastern tropical Pacific (Philander, 1990). The El Nino - Southern Oscillation (ENSO) phenomenon is known to have a remote influence on hurricanes (Pielke and Landsea, 1999; Tang an Neelin, 2004, Smith et al. 2007) and drought over the north America (Ropelewski and Halpert, 1986, Cole and Cook, 2012). Furthermore, at decadal to multidecadal times cales, the ocean plays an important role in sustaining long-term variations, such as the Pacific Decadal Oscillation (PDO) and the Atlantic Multidecadal oscillation (AMO). The multidecadal variations in the atmosphere, such as the multidecadal variation of hurricane activity, have been shown to have close relationship with the AMO (Goldenberg et al. 2001).

In the literature, there are many studies about the mean state and its influence on climate variability, such as the aforementioned relationship between the AMO and hurricane activity. It is found that the Icelandic Low controls the surface air temperature in the Gulf of Lion, and further affects the intermediate water formation (Jordi and Hameed, 2009). Zhu et al. (2007) studied the interaction between the Aleutian Low and the synoptic cyclones over the north Pacific at interannual time scales. Moreover, there is an interannual seesaw between the Icelandic low and the Aleutian low, which exhibits multidecadal modulations and affects the surface temperature as well as ocean-atmosphere exchange of heat and moisture (Honda et al., 2005). Hence, a better understanding of the mean state and its interaction with variability can help improve short-term climate predictions as well as projections of future climate change.

For linear variables such as air temperature and wind velocity, it is often convenient to separate the climate mean from the climate perturbations and apply

powerful techniques of linear statistical methods. However, the atmosphere is a chaotic system, characterized by unpredictable weather noise and complexities arising from nonlinearity. Philip and Van Oldenborgh (2009) find that nonlinear atmospheric response, such as the response of mean wind stress to SST, is a dominant term influencing the ENSO cycle. Furthermore, in the atmosphere, there are many inherently nonlinear variables, such as the *vertical wind shear*, which plays an important role to modulating hurricane activity, and the *surface wind speed*, which affects surface fluxes of heat, moisture, and momentum. For these nonlinear variables, it is not possible to easily separate the climate mean from the climate perturbations. The nonlinear superposition of mean flow and anomalous flow needs to be taken account in any analysis. In this dissertation, we explore some of the interesting complexities that arise when considering the influence of the mean state on the variability of vertical wind shear and heat fluxes at the air-sea interface.

As the vertical wind shear is an important factor modulating hurricane activity, the mean state of vertical wind shear is compared among observations, coupled model and uncoupled model simulations. The variation of vertical wind shear over the tropical Atlantic is further analyzed. Furthermore, the ENSO-shear relationship is revisited in the observations and compared between coupled model simulations and uncoupled model simulations. It is found that the superposition of mean flow and anomalous flow is important for explaining the spatial structure of vertical wind shear and its variation. In contrast to temperature or wind anomalies, different mean flows superposed on the same anomalous flow can cause opposite changes of vertical wind shear. The influence of the

mean wind on the ENSO-shear relationship and variation of tropical Atlantic vertical wind shear at different timescales are discussed in chapters II and III respectively.

Decadal climate predictions fill the gap between interannual climate prediction, which is dominated by natural modes of variability, and centennial climate projections, where external forcings dominate. By considering both natural variability and external forcings, climate prediction can provide societally useful information on the decadal timescale. The spatial patterns of surface winds are an important factor affecting climate variability and prediction (Richter and Xie 2008; Richter et al. 2012). In addition to helping drive the ocean currents, surface wind speed also affects the latent heat flux exchange by modulating surface evaporation, which can further influence the sea surface temperature (SST), a mechanism referred to as the Wind-Evaporation-SST (WES) feedback. It has been shown that the WES feedback modulates the displacement of ITCZ (Xie and Philander, 1994; Xie, 1999), the meridional propagation of SST anomalies (Chiang and Bitz, 2005; Mahajan et al. 2008,2010) and the tropical Atlantic "dipole mode" (Chang et al. 1997,Saravanan and Chang, 1999, 2004). In Chapter IV, we investigate the influence of the WES feedback on decadal prediction, by carrying out numerical experiments using an atmospheric general circulation (AGCM) model coupled to a slab ocean model where this feedback is mechanistically suppressed. Our investigation of the role of the WES feedback turned up some unexpected results that pointed to the important role played by the mean ocean heat transport in decadal predictions using a slab ocean model.

The use of the slab ocean model mitigates the problem of climate drift in coupled general circulation models (CGCMs), and reduces the effect of initial condition errors in the ocean, thus enabling us to make improved decadal predictions. The effect of missing ocean dynamics in the slab ocean model is prescribed as a constant flux correction term, representing the divergence of mean ocean heat transport. Temporal variations in the ocean heat transport are neglected in standard configuration of the slab ocean model. In Chapter V, we use alternate configurations of the slab ocean model to investigate how changes in the mean ocean heat transport affect decadal prediction skill.

CHAPTER II

MEAN WIND SHEAR AND ENSO-SHEAR RELATIONSHIP[*]

II.A. Introduction

Vertical wind shear has been shown to have a very close relationship to hurricanes (Gray 1984; Demaria 1996; Frank and Ritchie, 2001,). For hurricane development, tremendous energy is needed in the early developing stage. However, strong vertical wind shear causes strong energy dissipation, and further provides a non-favorable condition for hurricane development. Hence, the stronger the vertical wind shear is, the weaker the hurricanes are. Hurricanes over the North Atlantic demonstrate interannual variations, which are strongly correlated with the El Nino and Southern Oscillation (ENSO) (Goldenberg and Shapiro, 1996; Shaman et al. 2009). Consistent with the interannual variation of hurricanes, vertical wind shear over the North Atlantic is stronger during El Nino events and weaker during La Nina events (Goldenberg et al., 2001; Shaman et al., 2009).

The relationship between ENSO and vertical wind shear has been studied in observations, coupled model and uncoupled model simulations (Goldenberg et al., 2001; Shaman et al. 2009; Tang and Neelin 2004; Donnelly and Woodruff 2007; Aiyyer and Thorncroft 2011). It has been shown that during El Nino events, there is an enhanced Pacific Walker circulation, which causes anomalous westerly flow over the tropical

---

[*] Part of the data reported in this chapter is reprinted with permission from "Influence of mean flow on the ENSO-vertical wind shear relationship over the northern tropical Atlantic" by X. Zhu, R. Saravanan and P. Chang, 2012, 25, 858-864, copyright [2012] by American Meteorological Society.

Atlantic. As a result, tropical Atlantic vertical wind shear is enhanced, and leads to reduced hurricane activity. Therefore, better simulation of this ENSO-shear relationship can lead to better prediction of hurricane activity in numerical models.

Having established the importance of the relationship between hurricanes and vertical wind shear, in this chapter, we address the following questions: How well do numerical model simulate the vertical wind shear? Are there any differences in this ENSO-shear relationship between the coupled and uncoupled models? The datasets used in our analysis are described in section B. Prior to evaluating the ENSO-shear relationship, the simulated vertical wind shear in coupled models and uncoupled models are compared with the observations in section C. In section D, the relationship between vertical wind shear over the tropical Atlantic and ENSO are compared among observations, coupled models and uncoupled models. The differences between the simulations in coupled models and that in uncoupled models lead to a discussion of the importance of mean flow on the ENSO-shear relationship in section E. Finally, conclusions are drawn in Section F.

II.B. Datasets

In the case of individual hurricanes, vertical wind shear between different vertical levels can have different effects on the tropical storm's intensity (DeMaria, 1996; Black et al. 2002; Zeng et al. 2010). But for hurricane climatology, the magnitude of wind vector difference between 850hPa and 200hPa captures much of the influence of vertical wind shear on hurricanes (Vecchi and Soden 2007). Following the literature, we define

the *vertical wind shear* as, $|\vec{V}_{200} - \vec{V}_{850}|$ (Gray 1984, Goldenberg et al., 2001, Zhang and Deltworth, 2006, Vecchi and Soden, 2007, Wang et al., 2008).

For the wind observations from 1950 to 2008, two reanalysis datasets are used to assess the observational uncertainty. The first dataset is the National Centers for Environmental Prediction/National Center for Atmospheric Research (NCEP/NCAR) reanalysis dataset (Kalnay et al. 1996). And the second is the European Center for Medium-Range Weather Forecasts (ECMWF) 40 years reanalysis (ERA40) dataset from 1958 to 2003 (Uppala et al. 2005). Both datasets are monthly in the resolution of 2.5° latitude by 2.5° longitude. The Sea Surface Temperature (SST) datasets, starting from 1958, are the Hadley Center Sea Surface Temperature dataset (HadISST, (Rayner et al. 2003)) on 1° longitude by 1° latitude grid, and the Extended Reconstructed SST dataset (ERSST) (Smith et al. 2008) on 2° longitude by 2° latitude grid.

In addition to the above observational datasets, coupled model simulations of historical vertical wind shear are investigated in this chapter. The simulations of 20th century are chosen from the Intergovenmental Panel on Climate Change 4th Assessment Report (IPCC-AR4). There are 17 models used in our study shown in Table 2.1 and Table 2.2. The same period for the 20th century simulation, from 1958 to 1999, is chosen among all simulations for comparisons between observations and numerical model simulations.

Table 2.1 Summary of models

	Model	Experiment	Time	Ensemble size
Coupled models	CCCMA	20th century simulation	1850-2000	5
	CCSM3	20th century simulation	1870-1999	2
	CNRM	20th century simulation	1860-1999	1
	CSIRO	20th century simulation	1871-2000	3
	GFDL cm2.0	20th century simulation	1861-2000	3
	GFDL cm2.1	20th century simulation	1861-2000	3
	GISS E-H	20th century simulation	1870-2000	5
	GISS E-R	20th century simulation	1870-2000	9
	HADCM3	20th century simulation	1860-1999	2
	HADGEM1	20th century simulation	1860-1999	2
	IAP	20th century simulation	1850-1999	3
	INMCM	20th century simulation	1870-1999	1
	IPSL	20th century simulation	1860-2000	1
	MIROC Medium	20th century simulation	1900-2000	3
	MIROC High	20th century simulation	1900-2000	1
	MPI	20th century simulation	1860-2100	4
	MRI	20th century simulation	1851-2000	5
Uncoupled models	CCSM3	AMIP	1978-2000	1
	GFDL cm2.1	AMIP	1980-1999	1
	CAM3	Forced with observed SST from 1950 to 2000	1951-2000	5

Table 2.2 Abbreviations of coupled models

Acronym	Models
CCCMA	Canadian Centre for Climate modeling and analysis model
CCSM3	Community Climate System Model, version 3
CNRM	Centre National de Recherches Meteorologiques model
CSIRO	Commonwealth Scientific and Industrial Research Organization model
GFDL	Geophysical Fluid Dynamics Laboratory model
GISS	Goddard Institute for Space Studies
HADCM3	Hadley center Coupled ocean-atmosphere model version 3
HADGEM1	Hadley center Global Environment Model version 1
IAP	Institute of Atmospheric Physics model
INMCM	Institute for Numerical Mathematics Climate Model
IPSL	L'Institute Pierre-Simon Laplace model
MIROC	Model for Interdisciplinary Research on Climate
MPI	Max Planck institute for Meteorology model
MRI	Meteorological Research Institute model

To study the impact of coupling, two uncoupled simulations using the CCSM3 and GFDL models from the Atmospheric Model Intercomparison Project (AMIP) are also analyzed for the last 2 decades of the 20th century. In order to increase the sample size for the uncoupled simulation analysis, an additional 5-member ensemble integration using the Community Atmosphere Model, version 3 (CAM3) was carried out with observed monthly SST boundary conditions from 1951 to 2000.

II.C. Observed and simulated vertical wind shear

In order to evaluate numerical model simulations of vertical wind shear, the NCEP-NCAR reanalysis dataset and ECMWF ERA40 reanalysis dataset were used for validation from 1958 to 2000. As vertical wind shear is an important factor affecting hurricane genesis and development, we focus on the North Atlantic hurricane season, which lasts from July to October (JASO). In observations, the JASO mean vertical wind shear in both the reanalysis datasets are similar. Hence, Figure 1a shows the vertical wind shear averaged over the two reanalysis datasets. Climatologically, there is strong vertical wind shear from the Caribbean to northwestern Africa (Fig. 2.1a). Over the Main Development Region (MDR), the MDR average vertical wind shear is about 10m/s, which is considered as a favorable condition for hurricane development. But there is stronger vertical wind shear in the northern MDR and weaker vertical wind shear in the southern MDR. The 10m/s contour of vertical wind shear lies along the 15°N latitude over the MDR, which divides the MDR into a strong shear region to the north and a weak shear region to the south. This is consistent with the estimate, based on the best track datasets for Atlantic hurricanes occurring over the MDR from 1958 to 2008, that 20% of the tropical cyclones developed over the northern MDR, and 80% developed over the southern MDR.

Compared to the observations, the 17-model ensemble-mean JASO average vertical wind shear shows a fairly realistic spatial pattern (Fig. 2.1b). There is strong vertical wind shear extending from the Caribbean to the northwestern Africa. And to the south of this strong vertical wind shear, there is weak vertical wind shear. However, the

11

magnitude of simulated vertical wind shear is stronger than that in the observations. The ensemble averaged vertical wind shear exceeds 10m/s over the entire MDR (Fig. 2.1b). In general, the simulated vertical wind shear is about 2-4m/s stronger than that in the observations.

In contrast to the overestimated vertical wind shear in coupled models, the MDR average vertical wind shear simulated in the uncoupled simulations shows about the same magnitude as the observations, which is around 10m/s in regional average. However, there are biases in the spatial pattern of the vertical wind shear for the uncoupled simulations (Fig. 2.1c). Unlike the observations and coupled simulations, the western tropical Atlantic, especially the Caribbean and western MDR, is dominated by weak vertical wind shear, and the eastern MDR is dominated by strong vertical wind shear.

In the literature, SST variability has been shown to affect the vertical wind shear over the northern tropical Atlantic (Latif et al., 2007; Vecchi and Soden, 2007). Moreover, the simulated SST in coupled models often has biases, causing it to deviate from the observations. To identify the possible causes for the stronger vertical wind shear over the northern tropical Atlantic in the simulations, Singular Value Decomposition (SVD) analysis is carried out between the coupled model SST bias and the vertical wind shear biases in coupled models is presented in Figure 2.2. (Note that the independent variable in this SVD analysis is the model itself.)

(a) Observation

(b) Coupled models
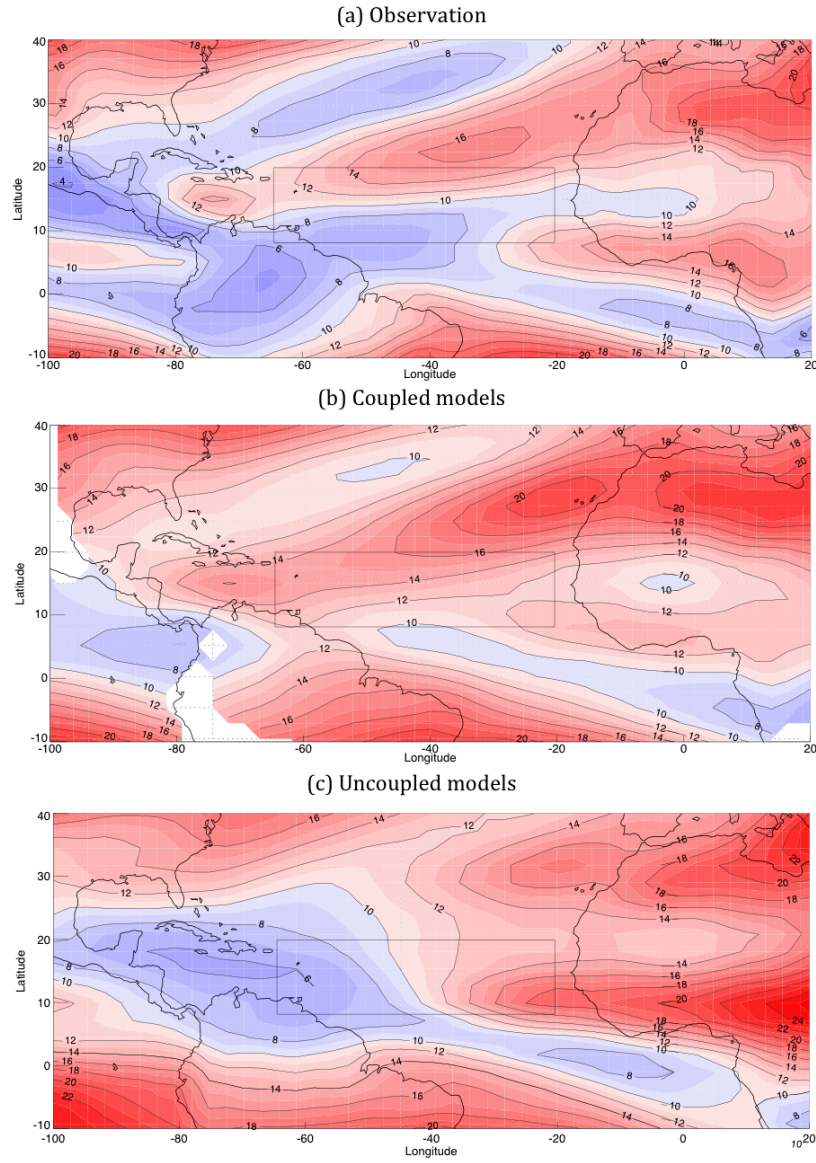
(c) Uncoupled models

Figure 2.1. The JASO mean vertical wind shear in (a) observations (average of NCEP and ECMWF), (b) 17 model coupled ensemble average and (c) 3 model uncoupled ensemble average. Units: m/s

The first leading SVD mode explains about 71% of the total covariance between

the SST biases and the vertical shear biases. In addition, the expansion coefficients of vertical wind shear biases are significantly correlated to that of SST bias, with the correlation coefficient reaching 0.95 (Fig. 2.2b). This indicates that the vertical wind shear biases are significantly correlated with the SST biases in the coupled models. When the SST biases are larger, the vertical wind shear biases tend to be larger as well.

The spatial structure of this SST-shear relationship is captured by the heterogeneous regression of vertical wind shear biases on the first SVD expansion coefficients for the SST biases (Fig. 2.2a). Over the northern tropical Atlantic, especially over the MDR, there are positive vertical wind shear biases with maximum amplitude larger than 3m/s. This overestimated vertical wind shear extends from the Caribbean to the northwestern Africa, with most of the region exceeding the 95% significance level.

Associated with this positive vertical wind shear bias over the north Atlantic (Fig.2.2a), there are warm SST biases over the tropical Pacific, Indian Ocean and south Atlantic, and cold SST biases over the north Atlantic in coupled models (Fig. 2.2c). The warmer eastern Pacific SST contributes to the stronger north Atlantic vertical wind shear through the anomalous Walker Circulation (Goldenberg et al. 2001; Vecchi and Soden 2007b). Moreover, the cooler north Atlantic SST, the warmer Indian ocean SST and the warmer south Atlantic SST also contribute to the stronger MDR vertical wind shear (Zhang and Delworth 2006; Latif et al. 2007). Therefore, SST biases in the coupled model simulations are associated with stronger vertical wind shears over the northern tropical Atlantic.

14

Figure 2.2. (a) Heterogeneous regression of vertical wind shear biases (Unit: m/s) and (c) homogenous regression of SST biases (Unit: °C) on the normalized first SVD expansion. Shading depicts 95% significance level. (b) Normalized first SVD expansion coefficients for vertical wind shear biases and SST biases.

II.D. Observed and simulated ENSO-shear relationship

The ENSO-shear relationship is illustrated by the regression of the JASO mean tropical Atlantic vertical wind shear on the NINO3 index in the observations (Fig. 2.3a). When warming occurs over the NINO3 region (5°S − 5°N, 90°W − 150°W), the Pacific Walker circulation becomes weaker, which further causes westerly anomalies at 200hPa over the tropical Atlantic. Hence, the vertical wind shear increases during the El Nino events from the Caribbean to the West Africa. Over the MDR, an increased vertical wind

shear during the El Nino events is evident over the western side of MDR, indicating unfavorable conditions for hurricane development. As a result, despite the warmer Atlantic SST anomalies associated with the El Nino events, fewer hurricanes develop over the tropical Atlantic during warm ENSO events, especially over the western Atlantic warm pool.
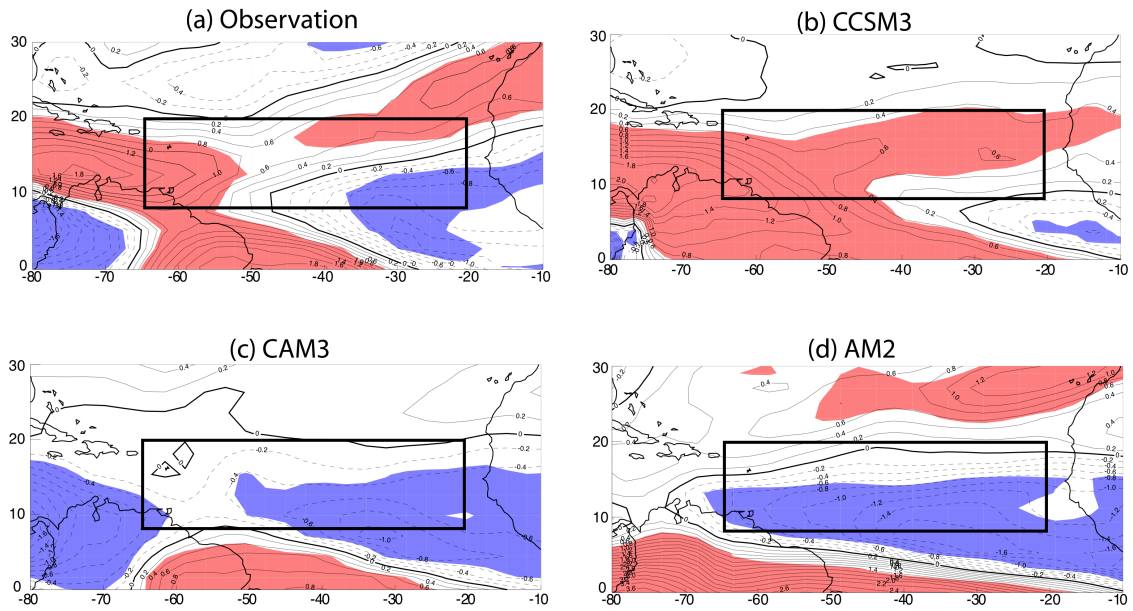
Figure 2.3. Regression between vertical wind shear and the NINO3 index during the JASO for (a) observations, (b) CCSM3 coupled 20th century integration, (c) CAM3 AMIP integration and (d) GFDL AM2 AMIP integrations. Units: m/s. The shaded region represents the 95% significance level.

The regression between the NINO3 index and the vertical wind shear over the northern tropical Atlantic is shown in Figure 2.3b for the coupled CCSM3 integration. The coupled model is fairly successful in capturing the positive regression between ENSO and shear over the MDR region and the Caribbean. The coupled GFDL CM2.1 integration shows similar results as the observations and the CCSM3 simulations (Figure not shown). However, when we compute the same ENSO-shear regression in the uncoupled CAM3 integration, we obtain a relationship of the opposite sign (Fig. 2.3c), with warm ENSO events corresponding to decreased wind shear over the entire region between 10°N and 20°N. The uncoupled GFDL AM2.1 also predominantly exhibits a weakening of shear over the MDR region, although not over the Caribbean (Fig. 2.3d), indicating that this "counterintuitive" ENSO-shear relationship may have somewhat complex origins. We investigate this issue further in the following section.

II.E. Importance of mean flow on the ENSO-shear relationship

In studies of the ENSO-shear relationship, the vertical wind shear over the tropical Atlantic has been linked to the shift of equatorial convection in the Pacific and changes in the Pacific Walker circulation, with an increased shear associated with decreased Walker circulation (Pielke and Landsea 1999; Vecchi and Soden 2007). The main contribution to this increased vertical wind shear is from the upper tropospheric zonal wind anomalies. With stronger convection over the eastern Pacific, there is stronger outflow at upper levels and hence enhanced westerlies over the tropical Atlantic (Klein et al. 1999). Therefore, we computed the regression of the zonal wind against the NINO3

index. At the 200hPa pressure level, we note that warm ENSO events are associated with anomalous westerlies over much of the tropical Atlantic in observations (Fig. 2.4a). The regression for the uncoupled CAM3 integration also shows westerly anomalies at 200hPa associated with warm ENSO events, although the amplitudes are weaker. Regression analysis for the lower tropospheric 850hPa zonal wind indicates increased westward trade wind anomalies, consistent with a decreased Pacific Walker circulation. In summary, observations and the CAM3 simulations both agree on there being an upper level westerly anomaly and a weaker lower level easterly anomaly associated with warm ENSO events.

Even though the observations and the uncoupled CAM3 simulation agree on anomalous response to ENSO, they disagree on the change in the total wind shear. Since vertical wind shear is a nonlinear measure, one needs to superpose the anomalous winds over the background winds before computing the shear. To underscore this point, we examined the mean 200hPa zonal wind in observations and the CAM3 model during the hurricane season (Figs 2.4c, d). In observations, the meridional extent of the mean easterly at 200hPa over tropical Atlantic is about 10° latitude, extending from the equator to 10°N. Over the northwestern MDR and the Caribbean, the mean flow at 200hPa in observation becomes westerly (Fig.2.4c). While in the CAM3 simulation, the background flow at 200hPa is strong easterly from equator to 20°N, with maximum speed reaching 24m/s (Fig. 2.4d). Both the meridional extent and strength of the simulated zonal flow at 200hPa are twice of that in the observations. Hence, instead of westerlies at 200hPa over the Caribbean and the northwestern MDR, there are strong

18

easterlies simulated in the CAM3. Similar to the uncoupled CAM3 simulation, easterlies are also overestimated in the uncoupled GFDL AM2.1 simulation. This difference between the simulated mean flow and the observations indicates that differences in the simulated ENSO-shear relationship may be explained through the nonlinear superposition of the ENSO-induced anomalous flow and the mean flow in the tropical Atlantic, especially over the western Atlantic warm pool.

Figure 2.5 gives a schematic illustration of the influence of mean flow on the ENSO-shear relationship. The ENSO-shear relationships in observations and the uncoupled model simulations are a result of the superposition of mean flow and anomalous flow (Fig. 2.5). The mean winds over the northern tropical Atlantic are controlled by local parameters such as the distribution of Atlantic SST and large-scale jets structures, such as the subtropical jet and the tropical easterly jet. This local flow pattern is modulated by the remote influence of ENSO, which affects the Walker circulation. The observed mean upper tropospheric flow is westerly and the lower tropospheric flow is easterly. The positive SST anomaly associated with a warm ENSO event induces an anomalous Walker circulation, which strengthens the upper level westerlies as well as the lower level easterlies, leading to increased vertical wind shear (Fig. 2.3a). However, in the CAM3 simulation, the simulated mean upper level flow is easterly. The upper level westerly anomalies associated with a warm ENSO event weaken the upper level easterlies in the CAM3 simulation, whereas the lower level easterlies increase slightly. Thus, a warm ENSO even is associated with reduced vertical wind shear in the CAM3 (Fig. 2.3c).

Figure 2.4. Regression of zonal wind at 200hPa with the NINO3 index during the JASO for (a) observations and (b) the uncoupled CAM3 simulation. Shaded region represents 95% significance level. JASO mean zonal wind at 200hPa for (c) NCEP and (d) the uncoupled CAM3 simulation. Units: m/s.
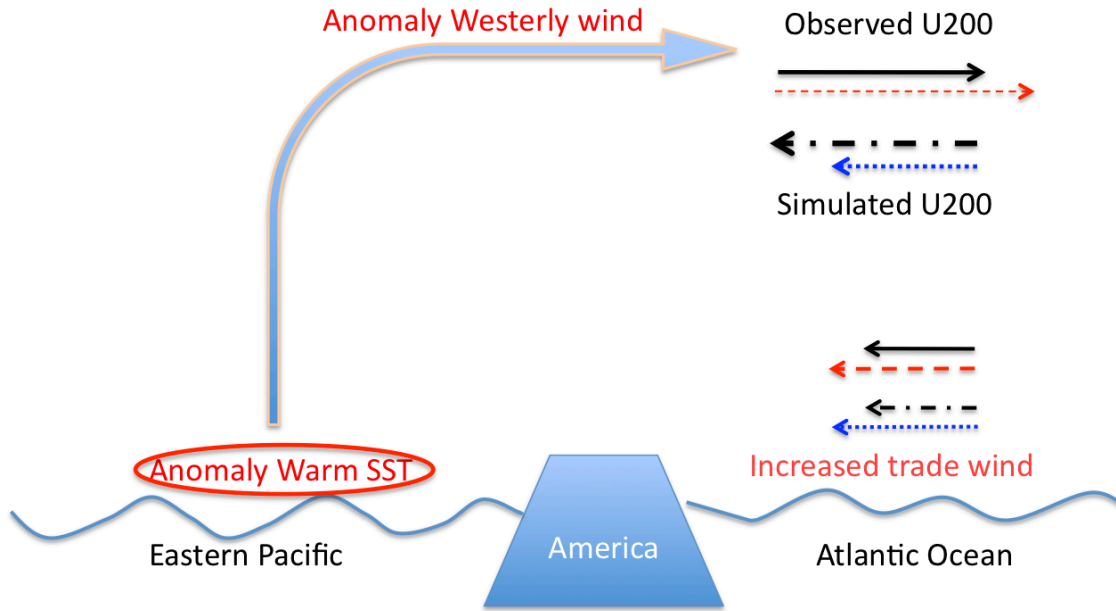
Figure 2.5. Schematic longitude-height section illustrating the nonlinear interaction between the remote influence of ENSO and the mean zonal wind over the western portion of the northern tropical Atlantic region (during the hurricane season). Solid arrows denote the 200hPa and 850hPa mean zonal winds in observations. The dashed arrows denote the zonal winds during a warm ENSO event in observations. The dash-dotted arrows denote the 200hPa mean zonal winds in the CAM3 simulation, and the dotted arrow denotes the zonal wind during a warm ENSO event, as simulated by CAM3. Note that the warm event leads to increased shear in observations but decreased shear in the CAM3 simulation, because of the easterly bias in the simulation of the upper level zonal wind.

To quantitatively verify the mechanism illustrated in Fig. 2.5, we constructed a regression model to estimate the vertical shear anomalies associated with ENSO. As the zonal wind component makes the largest contribution to vertical wind shear, we computed the vertical wind shear as $|U_{200} - U_{850}|$, using only the zonal component. Next, we decomposed the upper level zonal wind U_{200} into contributions from the mean flow and the ENSO-induced anomaly $U_{200} = U_{200}^{mean} + U_{200}^{ENSO}$. We estimated U_{200}^{ENSO} by computing the linear regression between mean zonal wind (U_{200}) and the NINO3 index, separately for the observations and the CAM3 integrations.

Comparing the influence of ENSO on zonal wind at the two levels, we find that the magnitude of anomalous wind at upper level is about 1m/s, which is five times larger than that at lower level. Therefore, we neglect variations in the lower level wind associated with ENSO. With these approximations, the total vertical shear associated with a warm ENSO even can be expressed as $|U_{200}^{mean} + U_{200}^{ENSO} - U_{850}^{mean}|$. Finally, the ENSO-induced vertical shear anomaly is computed as the difference between above value and the mean state vertical shear ($|U_{200}^{mean} - U_{850}^{mean}|$).

Fig. 2.6a shows the ENSO-induced vertical shear anomaly as computed using the regression model for observations. The regression model compares fairly well with the observed ENSO-shear relationship (Fig. 2.3a). In particular, the positive correlation in the western portion of the MDR and the Caribbean is captured well by this regression model. When we apply the regression model to the CAM3 simulations (Fig. 2.6b), again we find good agreement with the corresponding direct estimate of the ENSO-shear relationship (Fig. 2.3c). The regression model demonstrates a weaker vertical wind shear

during warm ENSO events, especially over the Caribbean and much of the MDR region. The simple regression model is also able to reproduce ENSO-shear relationship seen in the uncoupled GFDL model integration (Fig. 2.6c).
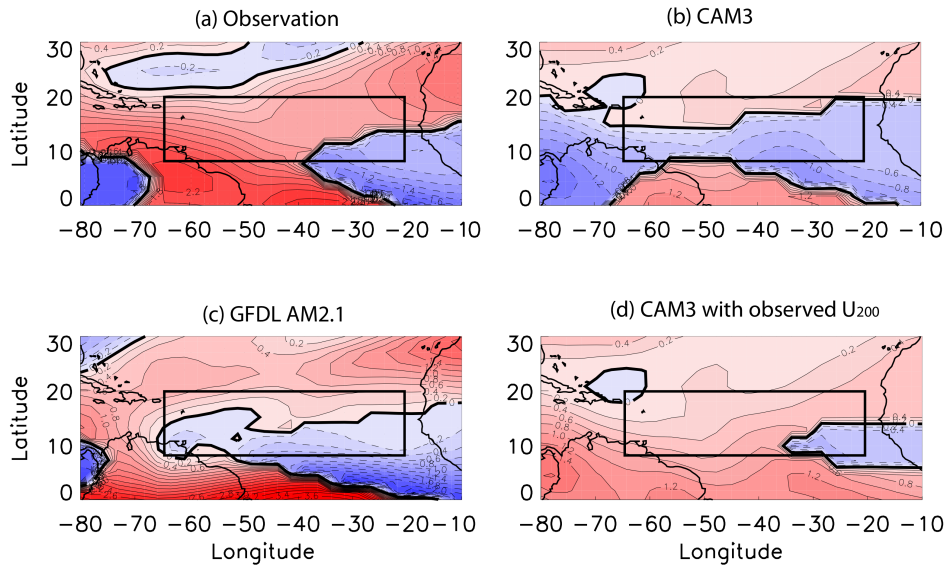
Figure 2.6. Regression model estimation of ENSO-induced vertical wind shear anomaly in (a) observation, (b) the CAM3, (c) the GFDL AM2 and (d) the CAM3 with observed climatology westerlies. Units: m/s

In order to directly identify the influence of the mean flow, we use the observed mean flow and simulated anomalous flow to evaluate the ENSO-shear relationship in the simple regression model (Fig. 2.6d). After replacing the simulated climatology easterlies in CAM3 with observed climatology westerlies, the ENSO-shear relationship evaluated in the simple regression model indicates increased vertical wind shear during El Nino

(Fig. 2.6d), which is same as the observation (Fig. 2.6a). The success of the simple regression model confirms the mechanism for nonlinear superposition between mean flow and anomalous flow schematically illustrated in Fig. 2.5.
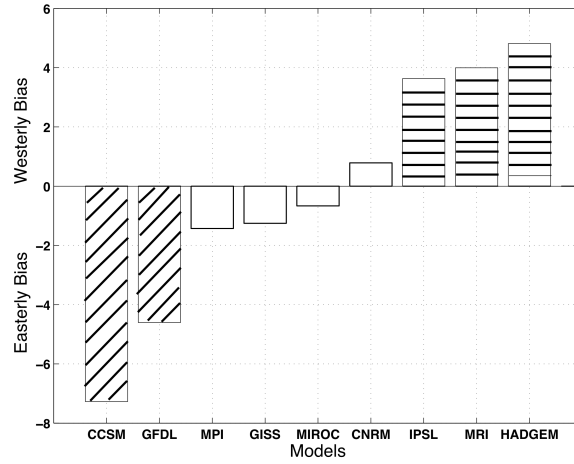
Figure 2.7. Histogram of biases of mean zonal wind at 200hPa (in m/s) averaged over the MDR, for 9 IPCC model AMIP simulations. Slanted-line shading indicates significant negative ENSO-shear correlation over the MDR and parallel-line shading indicates significant positive ENSO-shear correlation (no shading indicates weak correlations)

To further validate the influence of mean flow on ENSO-shear relationship, other AMIP-style experiments from IPCC-AR4 were analyzed. There are 9 models that have uncoupled AMIP simulations available, which are the CCSM, the CNRM, the GFDL, the GISS, the HADGEM, the MIROC, the MPI, the MRI and the IPSL. With realistic

ENSO signals present in all these AMIP experiments, biases of mean flow at 200hPa vary across the models (Fig. 2.7). Some models, such as the CCSM and the GFDL, have strong easterly biases, which leads to a significant negative ENSO-shear correlation over the MDR (Fig. 2.7), while some other models, such as the IPSL, the MRI and the HADGEM, tend to have strong westerly biases. Hence, the ENSO-shear relationship simulated by them over the MDR exhibits counter-intuitive positive correlations, like those seen in the uncoupled CAM3 simulations.

II.F. Conclusions

In this chapter, the JASO mean vertical wind shear over the northern tropical Atlantic is compared among observations, coupled model and uncoupled model simulations. Both the NCEP and the ERA40 reanalysis show similar vertical wind shear climatology, i.e., stronger vertical wind shear to the north of 15°N latitude and weaker vertical wind shear to the south of 15°N latitude. As a result, more hurricanes develop over the southern MDR than the northern MDR. Similar to the observations, the 17 coupled models from IPCC AR4 simulate a realistic spatial pattern of vertical wind shear. However, the magnitudes of the simulated vertical wind shear are stronger than those in observations, with a bias of about 2−4m/s. Compared to the coupled simulations, the simulated MDR vertical wind shear in the uncoupled simulations are of the same magnitude as that in observation, but the spatial pattern of differs from the observations.

We further investigated the causes of the overestimated vertical wind shear in

coupled models using SVD analysis, using the models themselves as the independent variable. The SVD analysis between the vertical wind shear bias and the SST bias demonstrates that the vertical wind shear bias is highly correlated with the SST bias in coupled simulations. Compared to the observations, there is warm tropical SST, warm Indian Ocean SST bias and cold north Atlantic SST bias in the coupled model simulations. According to the literature, these SST biases contribute to stronger vertical wind shear over the northern tropical Atlantic (Latif et al. 2007; Vecchi and Soden, 2007).

Furthermore, we analyzed the ENSO-shear relationship over the northern tropical Atlantic simulated by coupled and uncoupled models, as well as observations. Surprisingly, the uncoupled CAM3 and GFDL AM2 atmospheric models forced with observed SST produced an incorrect simulation of the ENSO-shear relationship, with decreased vertical wind shear during the warm phase of the El Nino, in contrast to both observations and coupled models simulations. In observations, stronger vertical wind shear associated with El Nino events occurs from the Caribbean to the West Africa, which is controlled by the westerlies at the upper level. In AMIP-style experiments using CAM3 and GFDL AM2 forced with observed SST, the ENSO-induced flow anomalies are the same as those in the observations. But the simulated mean zonal wind at the upper level has an easterly bias in both CAM3 and GFDL AM2 over the Caribbean and western MDR regions. In these regions, where the upper level easterlies are overestimated, the relationship between vertical wind shear and ENSO in the uncoupled model simulations turns out to be opposite to that in the observations and the coupled

model simulations.

The difference between uncoupled model simulations and observation indicates that although there is a strong remote influence of ENSO on vertical wind shear, the local background mean flow may alter the sign of the ENSO-shear relationship, as schematically illustrated in Fig. 2.5. We constructed a simple linear regression model that was able to capture the important features of the ENSO-shear relationship both in observations and the uncoupled CAM3 simulations. The success of simple regression model further validates the nonlinearity of the superposition of mean flow and anomalous flow.

The nonlinear superposition of mean flow and anomalous flow suggests that the climatological mean state can have a large influence on the simulated vertical wind shear variability. In addition to ENSO, phenomena such as the Atlantic Multidecadal Oscillaiton (AMO) may lead to interdecadal modulations of the mean flow over the northern tropical Atlantic (Knight et al. 2006; Wang et al. 2008), and further influence the decadal variability of vertical wind. In the context of climate change, there is considerable interest in the trends in vertical wind shear over the northern tropical Atlantic region (Vecchi and Soden 2007). Our study suggests that biases in the mean states can have a large influence on the simulated shear anomalies. Therefore, climate models with significant errors in the mean flow simulations may need to be excluded from projected estimates of vertical wind shear variation.

CHAPTER III

VERTICAL WIND SHEAR VARIATION AT INTERANNUAL AND MULTI-

DECADAL TIME SCALES

III.A. Introduction

Vertical wind shear plays an important role in tropical cyclogenesis: the stronger the vertical wind shear, the weaker the hurricane activity (Gray 1984; DeMaria 1996). Among the important factors affecting cyclogenesis, vertical wind shear lower than 10m/s is considered as a favorable condition for hurricane development (Gray 1968; Goldenberg and Shapiro 1996; Gray 1998). Hence, the variation of tropical cyclones over the tropical Atlantic is closely related to the variation of vertical wind shear from interannual to multi-decadal time scales (Aiyyer and Thorncroft, 2006, 2011; Wang et al., 2008). In climate model projections of the global warming scenario, warmer equatorial SST (Liu et al., 2005; Zhu et al., 2009) and increased tropical Atlantic vertical wind shear (Vecchi and Soden 2007) are predicted. Based on the fact that warmer SST gives more favorable conditions for hurricane genesis, an increase of tropical storms is expected. However, with a stronger vertical wind shear over tropical Atlantic under the global warming scenario (Vecchi and Soden 2007b), there may be a reduction in the number of tropical storms (Bengtsson et al. 2007; Emanuel et al. 2008).

The interannual to multidecadal variability of vertical wind shear over the tropical Atlantic has been related to the variations of tropical Pacific SST (Goldenberg and Shapiro 1996), the Atlantic Multi-decadal Oscillation (AMO) (Zhang and Delworth

2006; Wang et al. 2008), the Atlantic Meridional Mode (AMM) (Smirnov and Vimont, 2010) and global spatial SST patterns (Latif et al. 2007; Vecchi and Soden 2007a). On shorter time scales, a robust seasonal variation of vertical wind shear occurs over the tropical Atlantic, due to the seasonal intrusion and retreat of upper level jets (Aiyyer and Thorncroft 2006).

Besides the seasonal cycle, the vertical wind shear over the tropical Atlantic also exhibits interannual variability, which is strongly related to the ENSO events, with a warm ENSO event being associated with stronger vertical wind shear and vice versa (Goldenberg and Shapiro 1996; Pielke and Landsea 1999; Elsner et al. 2001; Tang and Neelin 2004; Donnelly and Woodruff 2007; Aiyyer and Thorncroft 2011). It has been noted that warmer eastern Pacific SST results in a weaker Pacific Walker circulation, leading to anomalous westerly flow in the upper troposphere over the Atlantic (Klein et al. 1999). This teleconnection between the Pacific ocean and the Atlantic ocean results in stronger vertical wind shear occurring during El Nino events (Aiyyer and Thorncroft 2006).

The vertical wind shear over the northern tropical Atlantic also demonstrates a multi-decadal variation, which contributes to the multi-decadal variations in tropical Atlantic hurricane activity (Goldenberg et al. 2001; Knight et al. 2006a; Aiyyer and Thorncroft 2006; Zhang and Delworth 2006; Latif et al. 2007; Wang et al. 2008). At the multi-decadal time scale, it is found that there is weaker tropical Atlantic vertical wind shear during the warm phases of AMO and stronger shear during the cold phases of AMO.

It is interesting to note that the relationship between vertical wind shear and ENSO over the eastern tropical Atlantic is opposite to that over the western tropical Atlantic (Zhu et al., 2012). Similarly, the relationship between the tropical Atlantic shear and AMM over the eastern tropical Atlantic is also opposite to that over the western tropical Atlantic (Smirnov and Vimont 2010). Hence, the first objective of this chapter is to understand the spatial patterns associated with the variability of tropical Atlantic vertical wind shear. Another objective of this chapter is to identify the important factors that contribute to wind shear variability.

Considering the strong coupling between the atmosphere and the tropical oceans, variation of vertical wind shear is often related to the boundary SST forcing in the literature. By forcing an Atmospheric General Circulation Model with observed SST from 1870 to 2003, Latif et al. (2007) found that individual ocean basins make different contributions to the vertical wind shear over the Main Development Region (MDR). Warmer northern tropical Atlantic SST reduces the MDR vertical wind shear, while warmer SST over the tropical Pacific and tropical Indian Ocean increases the MDR vertical wind shear. Latif et al. (2007) hence conclude that increased SST difference between the Atlantic and Indo-Pacific basins leads to reduced tropical Atlantic vertical wind shear. Also, under the global warming scenario, Vecchi and Soden (2007a) find that both local SST anomalies and spatial gradients in the SST warming trend could affect the tropical cyclone activities over the tropical Atlantic.

In addition to the SST forcing on the vertical wind shear, the mean flow plays an important role in modulating the ENSO-shear relationship, as discussed in the previous

chapter (Zhu et al., 2012). The mean flow structure could significantly alter the shear anomalies due to ENSO. Hence, the influence of mean flow on the variation of tropical Atlantic shear is also studied in this chapter.

The datasets used and the methodologies are described in Section B. Section C highlights some statistical properties of vertical wind shear. In section D, the spatial patterns of vertical wind shear variability are analyzed, along with a discussion of SST forcing. In addition, the origin of the dominant spatial pattern of vertical wind shear variability is discussed in section E. Finally, the role of mean state on vertical wind shear variability is summarized in section F.

III.B. Datasets and methodology

Using the best track data (Landsea et al. 2004), hurricane genesis locations from 1958 to 2008 are shown in Figure 3.1, with total 554 tropical storms observed between July and October. There are two main regions for tropical cyclogenesis: (i) the western Atlantic warm pool and the Gulf of Mexico, which includes the Shear Enhanced Region (SER) described in Vecchi and Solden (2007); and (ii) the Main Development Region (MDR, 8°N-20°N, 20°W-65°W), which has been studied extensively in the literature (Goldenberg et al. 2001; Wang et al. 2008; Emanuel 2005; Donnelly and Woodruff 2007; Vecchi and Soden 2007b; Shaman et al. 2009; Garner et al. 2009; Zhang and Delworth 2006; Vecchi and Knutson 2008; Saunders and Lea 2008). In this study, we focus on the northern tropical Atlantic during the period from July to October (JASO).

31
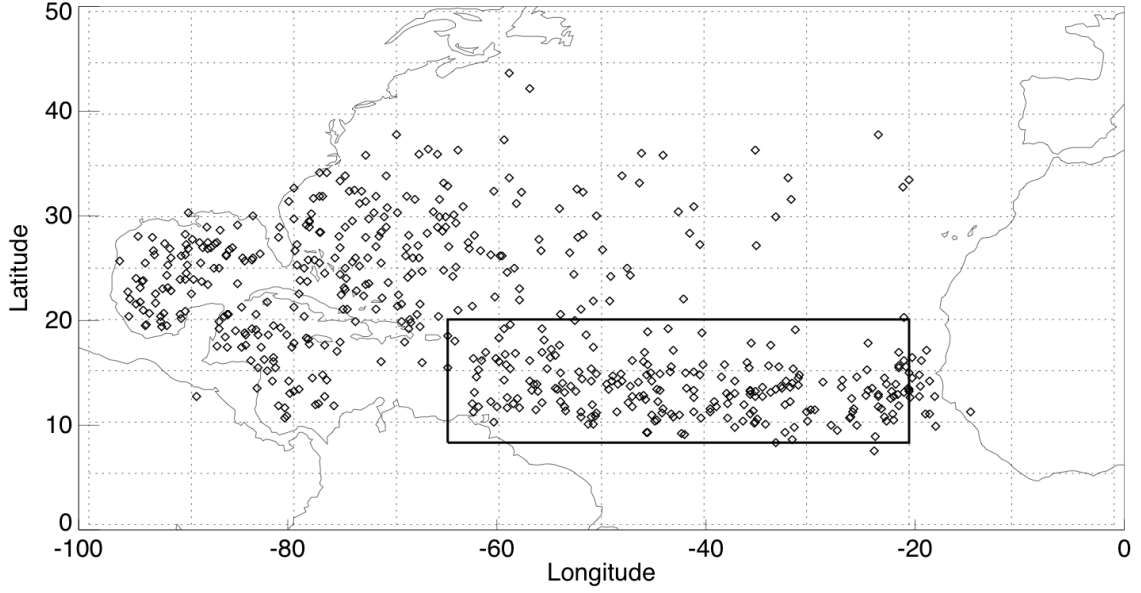
Figure 3.1. Cyclonegenesis locations for tropical storms from 1958 to 2008 (the rectangle represents the MDR).

Following the literature, we define the vertical wind shear as the magnitude of wind vector difference between 850hPa and 200hPa ($|\vec{V}_{200} - \vec{V}_{850}|$). We should note, however, that the vertical wind profile averaged over the MDR shows the maximum amplitude of vertical wind vector difference between the 700hPa and 150hPa levels. However, Vecchi and Soden (2007b) found that using an alternative definition of vertical wind shear, the magnitude of wind vector difference between 700hPa and 150hPa, has results equivalent to the traditional definition of vertical shear using the 850hPa and 200hPa levels.

For observations of wind and SST, the same datasets are used as in Chapter II. For the wind observations from 1958 to 2008, we use the NCEP reanalysis dataset and the ECMWF ERA40 datasets. For SST, we use the HadISST and the ERSST datasets, starting from 1958. Beside these datasets, the 4x daily NCEP reanalysis datasets are used to study the statistical properties of vertical wind shear, at 2.5° latitude by 2.5° longitude resolution. In addition to the observational data, we analyze simulations from of historical vertical wind shear from 17 coupled models, i.e., the 20th Century runs carried out for IPCC AR4, shown in Table 1 of Chapter II.

In addition to the datasets from observations and IPCC AR4, we analyze numerical model simulations using the Community Atmospheric Model, version 3 (CAM3) with T42 spectral resolution. A 5 member ensemble of 50-year integrations was carried out, with CAM3 forced with a repeating annual cycle of climatological SST. We refer to this as the CAM3-climatology-SST run, as there is neither interannual nor multi-decadal variation in the boundary SST. As a result, the SST forcing on the vertical wind shear is completely eliminated in this experiment, allowing us to address the contribution of internal atmospheric variability to vertical wind shear variations.

Several statistical techniques are used to study the variability of vertical wind shear at interannual and multidecadal times cales. In order to identify the dominant modes of vertical wind shear over the northern tropical Atlantic, Empirical Orthogonal Function (EOF) analysis is performed based on the JASO mean vertical wind shear in observations and numerical simulations. In addition, Singular Value Decomposition (SVD) analysis between vertical wind shear and tropical SST is carried out to study the

impact of local and remote SST forcing on the variation of vertical wind shear over the northern tropical Atlantic. As discussed earlier, the vertical wind shear exhibits seasonal, interannual and multi-decadal variations. It would therefore be interesting to analyze the variation of vertical wind shear and its relation with tropical SST on different time scales. Therefore, band pass filtering (2-7 years) and low pass filtering (>7 years) are used to separate the variation of vertical wind shear into interannual and multi-decadal components.

III.C. Statistical properties of vertical wind shear

Before addressing the long-term variability of vertical wind shear, the statistical properties of vertical wind shear are studied, such as the mean, the skewness and the kurtosis, using the following definitions:

$$skewness = \frac{\sum\limits_{1}^{N}(X_i - \overline{X})^3}{(N-1)\sigma^3}; \quad kurtosis = \frac{\sum\limits_{1}^{N}(X_i - \overline{X})^4}{(N-1)\sigma^4} - 3$$

Here, $\overline{X}$ is the mean and σ is the standard deviation.

Note that the definition of vertical wind shear involves a nonlinear combination of wind vectors at different levels. This nonlinearity suggests that using different approaches for calculating the vertical wind shear at different time scales may change the statistical properties of vertical wind shear. There are two possible ways to calculate the vertical wind shear at different time scales. The first method, shown in (1), averages the wind component over certain time scale of interest first, and then computes the vertical wind shear.

$$Vertial\ Wind\ Shear = \sqrt{(\overline{u}_{850} - \overline{u}_{200})^2 + (\overline{v}_{850} - \overline{v}_{200})^2} \qquad (1)$$

The second method, shown in (2), computes the vertical wind shear with 6 hourly intervals first and then averages the calculated shear over time scale of interest.

$$Vertial\ Wind\ Shear = \overline{\sqrt{(_{850} - v_{200})^2 + (v_{850} - v_{200})^2}} \qquad (2)$$

In addition, according to the SST anomaly during the Atlantic hurricane season, we stratified the data into three sample categories. The first group is *the El Nino category*, which contains 10 strong El Nino events (1965, 1972, 1982, 1987, 1991, 1994, 1997, 2002, 2004, and 2006). The second group is *the La Nina category* including ten strong La Nina years (1964, 1970, 1973, 1975, 1988, 1995, 1998, 1999, 2000, and 2007). The last group is *the climatology category*, which contains the total 50 years from 1958 to 2007. Hence, the statistical properties of vertical wind shear can be compared among the three categories.

On the daily time scale, both calculation methods give similar shapes for the Probability Density Function (PDF, Fig. 3.2a and 3.2b). The peak of vertical wind shear is below 10m/s for all three groups. All distributions on the daily timescale skew to the left with positive skewness coefficients. This indicates that the vertical wind shear at daily timescale is not sensitive to the change of calculation methods. Moreover, there are only small differences on the distribution between the El Nino category and the La Nina category. There is less than 1m/s increase of the mean and a slightly fatter tail in the El Nino category. Both distributions of vertical wind shear on the daily timescale have nongaussian shapes, with few differences among different categories.

But at longer times cales, not only do the differences between the El Nino category

and the La Nina category become larger, but the differences between two methods of computing shear also increase. On the monthly time scale, the distribution of vertical wind shear calculated by the first method (Fig. 3.2c) has a flatter distribution than that using the second method (Fig. 3.2d). The distribution of vertical wind shear using the first method (Fig. 3.2c) shows a peak lower than 10m/s during the La Nina years, while the peak value for the El Nino group is above 10m/s. As a result, the difference in the mean of vertical wind shear between the El Nino and the La Nina categories becomes larger (Fig. 3.2c). While using the second method, the distribution show similar peaks for the La Nina group and the El Nino groups and have same mean value as that at daily time scale (Fig. 3.2d).

On the seasonal timescale, using the first method, the PDF for all three categories is even more flatly distributed about the mean value than that at monthly time scales (Fig. 3.2e). The differences of the distribution between the El Nino category and the La Nina category are much larger than that at shorter time scales (Fig. 3.2e). Comparing the El Nino category with the La Nina category, the difference of the mean reaches about 2m/s and the difference of the peak is about 6-7m/s, using the first calculation method (Fig. 3.2e). Furthermore, the skewnesses of the two categories are opposite, with PDF of the El Nino category skewing to the right and distribution of La Nina category skewing to the left (Fig.3.2e). However, using the second method for computing the vertical wind shear, we find smaller differences for the PDF of vertical wind shear at seasonal time scales among the three categories. All distributions skew to the left, with same mean value as for shorter time scales (Fig. 3.2f).
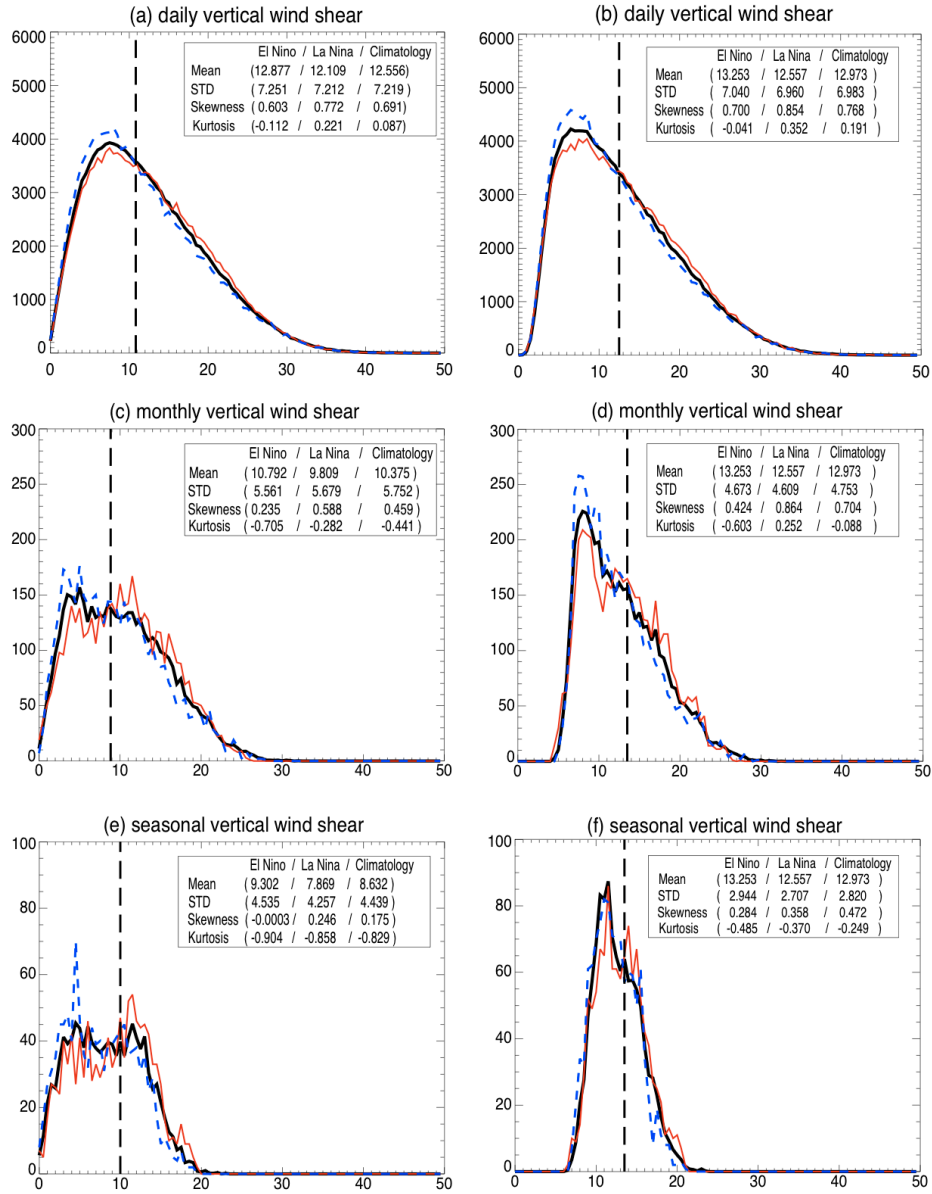
Figure 3.2. The PDF of vertical wind shear over the MDR. The left column is for vertical wind shear calculated with the Method 1 at (a) daily, (c) monthly and (e) seasonal time scales. The right column is for vertical wind shear calculated using Method 2 at (b) daily, (d) monthly and (f) seasonal time scales.

The above comparison indicates that the statistical properties of vertical wind shear are sensitive to the computation methods due to the nonlinearity of vertical wind shear. For individual hurricanes, the vertical wind shear on the daily timescale is important, suggesting that Method 2 should be used to compute the vertical wind shear (DeMaria 1996). However, for climatological analysis, the shear calculated with daily winds and monthly winds have similar results (Vecchi and Soden 2007). Following the literature, we compute the vertical wind shear using Method 1.

III.D. Spatial mode of vertical wind shear variation

In this section, the EOF analysis is used to identify the dominant spatial patterns of vertical wind shear variation over the northern tropical Atlantic, especially over the MDR. In addition, the relationship between tropical SST and tropical Atlantic vertical wind shear's variation is investigated using SVD analysis.

III.D.1.Modes of observed shear variability

The leading EOFs for the monthly NCEP and ECMWF reanalysis data are shown in Fig. 3.3a and Fig. 3.3b. The leading EOFs for both reanalysis data show a *dipole mode* over the northern tropical Atlantic, especially over the MDR. There is a positive region extending eastward from the Caribbean to the west coast of Africa. To the south of this positive region, a negative region extends westward to the southeastern MDR, with minimum values in western Africa. This indicates that the variation of vertical wind

38

shear over the western tropical Atlantic is opposite to that over the eastern tropical Atlantic. When strong vertical wind shear dominates the MDR, the dipole mode is defined to be in a *strong phase* (as shown in figure 3.3). While in a *weak phase* of dipole mode, the MDR is dominated by weak vertical wind shear.
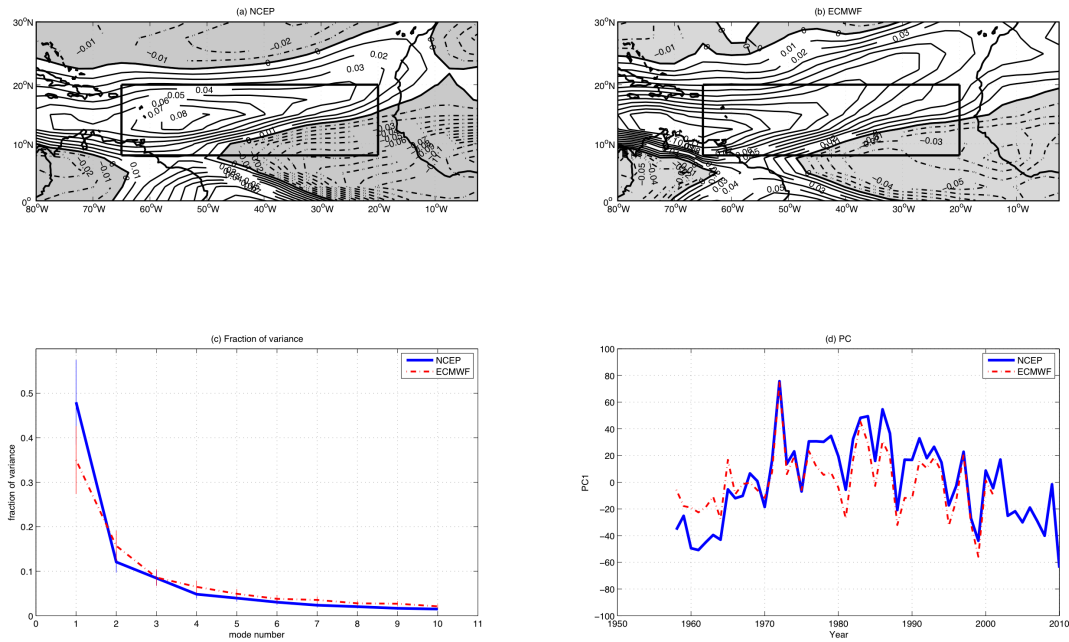
Figure 3.3. The leading EOF mode for (a) the NCEP reanalysis dataset, (b) the ECMWF dataset. Shaded regions represents negative values. (c) The fraction of variance explained by first 10 EOF modes. Vertical lines represent the standard error. (d) The first Principal Component (PC1). The solid lines represent NCEP reanalysis and the dash-dotted lines represent ECMWF reanalysis.

The leading EOF mode accounts for 54.7% of the total variance for the NCEP dataset and 31.6% for the ECMWF dataset. However, the second EOF mode explains less than 20% of the total variance in both datasets (Fig. 3.3c). As per North's criterion (Fig. 3.3c), the first EOF mode is well separated from the other modes and explains most of the variance (North et al. 1982). Furthermore, besides the similarity in spatial patterns (Fig. 3.3a and 3.3b), the temporal variations of dominant EOF of vertical wind shear are also similar in both reanalysis datasets (Fig. 3.3d).

It is interesting to note that the temporal variation of the dipole mode exhibits both interannual and multi-decadal variations. We use band-pass filtering (2-7 year) and low-pass filtering (>7 year) before the EOF analysis to separate the vertical wind shear variation over the northern tropical Atlantic into interannual and multi-decadal times cales. The leading principal components of the band-pass filtered datasets demonstrate a clear interannual variation (Fig. 3.4e). For the low-pass filtered datasets, the multi-decadal timescale dominates the temporal variation of the dipole mode of vertical wind shear (Fig. 3.4f).

In addition, the leading EOF patterns at both interannual and multi-decadal time scales show strong similarities to those in Figures 3.3a and 3.3b, with pattern correlation coefficients exceeding 0.95. There are similar dipole modes of vertical wind shear over the northern tropical Atlantic in the first leading EOF for the band-pass filtered NCEP reanalysis (Fig. 3.4a) and the band-pass filtered ECMWF reanalysis (Fig. 3.4b). Moreover, the first EOF for low-pass filtered NCEP reanalysis (Fig. 3.4c) is similar to the low-pass filtered ECMWF reanalysis (Fig. 3.4d). Once again, based on the North's

criterion, the leading EOFs for the filtered datasets are also clearly separated from the remaining EOFs. This indicates the dipole mode is a robust feature of vertical wind shear variability on both interannual and multi-decadal time scales.
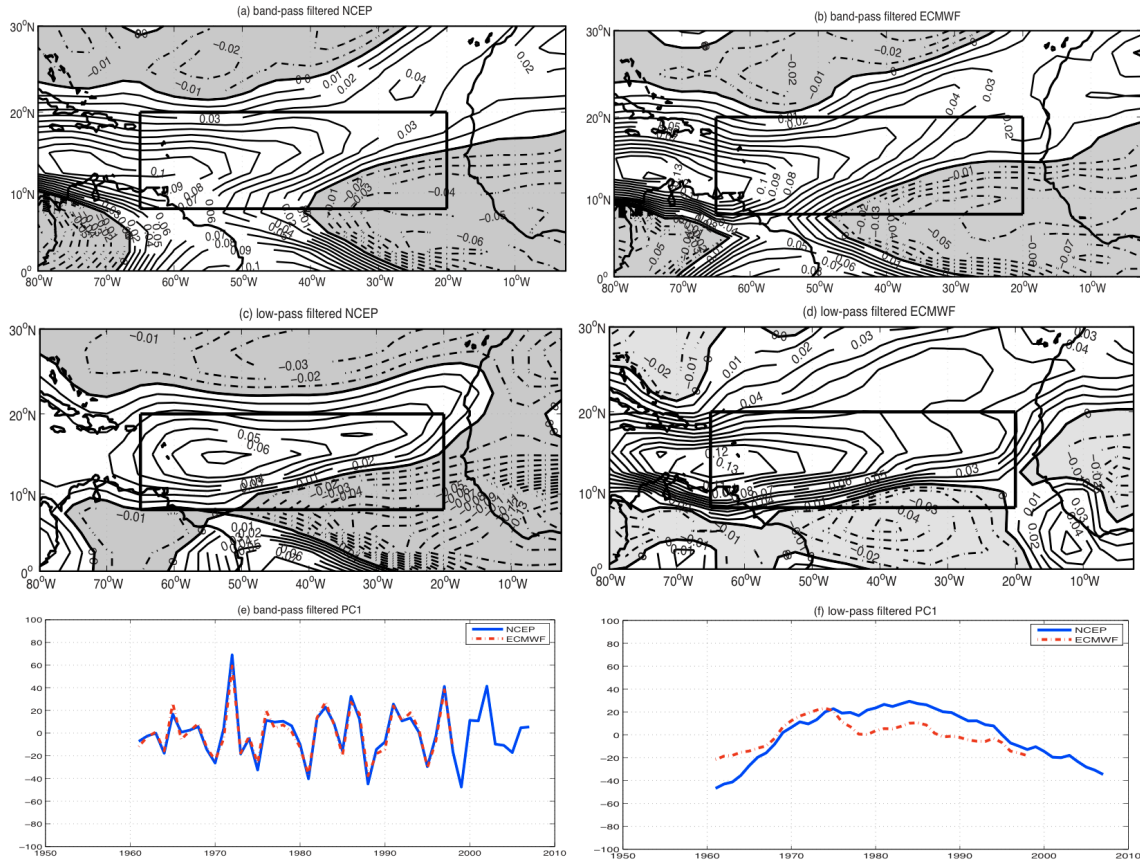
Figure 3.4. The leading EOFs for (a) band-pass filtered NCEP dataset, (b) band-pass filtered ECMWF dataset, (c) low-pass filtered NCEP dataset and (d) low-pass filtered ECMWF dataset. Shading denotes negative values. The leading principal component for (e) band-pass filtered datasets and (f) low-pass filtered datasets. The blue lines represent NCEP reanalysis and the red dash-dotted lines represent ECMWF reanalysis.

III.D.2.Modes of simulated shear variability

Similar to the observed patterns of vertical wind shear variability, the simulations from the 17 coupled models also exhibit a dominant dipole mode as the leading EOF, with percentage of total variance explained ranging from 25% to 68%. Similar to the observed dipole mode, simulated dipole modes also typically have one center located near the northwestern MDR, and the other center located near the southeastern MDR. To quantify the similarity between observed and simulated dipole modes, the spatial pattern correlation coefficients between leading observed and simulated EOF patterns are computed (Figure 3.5). We note that the observed and simulated patterns of variability are quite similar, with correlations exceeding 0.5 for all the models, except the IPSL and INMCM model. (The simulated vertical wind shear in the IPSL and INMCM models still exhibits a dipole mode, but with shifted centers.) We therefore conclude that the dipole mode of vertical shear variability is robust across models and well-simulated when compared to the observations.
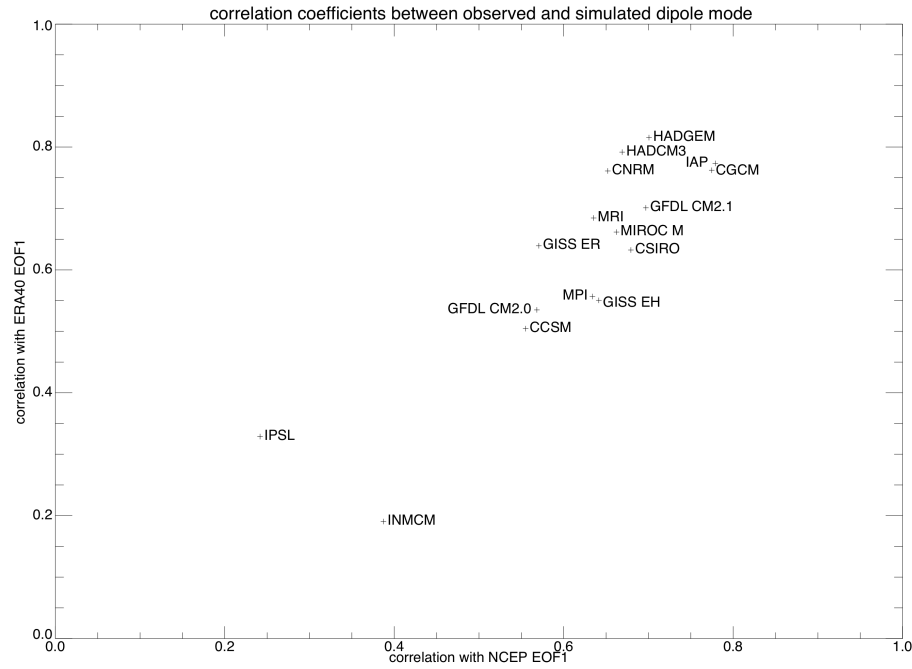
Figure 3.5. Pattern correlation coefficients between leading observed EOF pattern in two reanalysis datasets and the leading simulated EOF pattern in the 17 IPCC models. X-axis is for the NCEP reanalysis and Y-axis is for the ECMWF reanalysis. [Based on a student-*t* test, all simulated modes have significant correlation with observed modes, exceeding 95% significance level (df = 544, p < 0.05).]

III.D.3. SST forcing of the dipole mode at interannual time scale

In order to examine the relationship between SST variability and the dipole mode of vertical wind shear, SVD analysis is performed between the northern tropical Atlantic vertical wind shear and the global tropical SST. This analysis can identify pairs of patterns that maximize the temporal covariance between the two variables (Bretherton et

al. 1992; Wallace et al. 1992). As the dipole mode of vertical wind shear over the northern tropical Atlantic is a robust feature at both internannual and multi-decadal time scales, the influences of tropical SST on the dipole shear mode are also analyzed at both time scales.

For the dominant SVD mode on the interannual timescale, the correlation coefficient between the normalized expansion coefficients for vertical wind shear (Fig. 3.6b) and SST (Fig. 3.6c) is 0.81, which is significant at the 99% level (student-t test, *effective degree of freedom* = 46.4). The squared covariance explained by the leading SVD mode accounts for 94% of the total. This implies that the vertical wind shear over the northern tropical Atlantic is closely related to the global tropical SST variability. Similar to the leading EOF for vertical wind shear, the heterogeneous regression of vertical wind shear anomalies onto the first expansion coefficients for the leading tropical SST SVD pattern also shows a dipole mode (Fig.3.6a). This regression pattern between the vertical wind shear anomalies and the first SVD expansion coefficients for tropical SST is significant at the 95% level (shaded region in Fig. 3.6a), based upon a student-t test.

On the interannual timescale, there is a significant influence of tropical SST anomalies from the Pacific Ocean and Indian Ocean (shaded area in Fig. 3.6d) on tropical Atlantic vertical wind shear anomalies. However, there does not appear to be a significant influence originating from tropical Atlantic SST. The spatial pattern of homogeneous regression of SST on the leading SVD expansion coefficient is dominated by the ENSO signal over the tropical Pacific. There are warmer eastern Pacific SST and

44

cooler western Pacific SST anomalies, which contribute to increased vertical wind shear in the western tropical Atlantic and reduced vertical wind shear in the eastern tropical Atlantic, consistent with the *strong phase* of dipole shear mode. Kossin and Vimont (2007) showed that stronger vertical wind shear due to the El Nino events occurs mainly over western tropical Atlantic, especially over the Caribbean. Hence, with 1°C maximum SST warming at the eastern Pacific, the vertical wind shear increases by about 2 m/s over the Caribbean and decreases about 0.75 m/s over the eastern equatorial Atlantic. This stronger vertical wind shear at the western tropical Atlantic is caused by enhanced westerlies at upper level and enhanced trade winds at the lower level, which is associated with a weakened Pacific Walker circulation during warm ENSO events (Vecchi and Soden 2007b).

Besides tropical Pacific SST anomalies, warmer Indian Ocean SST is also significantly correlated with the dipole shear mode. Warmer Indian ocean SST would weaken the Asian summer monsoon (Yang et al. 2007) and the African summer monsoon (Giannini et al. 2003; Kerr 2003). These changes in the African monsoon are associated with drought in the Sahel region (Palmer 1986; Giannini et al. 2003; Kerr 2003), as well as a weakening of Tropical Easterly Jet (Hastenrath 2000, Yang et al. 2007). As the tropical easterly jet dominates the upper level flow, its weakening may contribute to reduced vertical wind shear over the eastern tropical Atlantic. Therefore, warmer Indian ocean SST is associated with reduced vertical wind shear over the eastern tropical Atlantic.
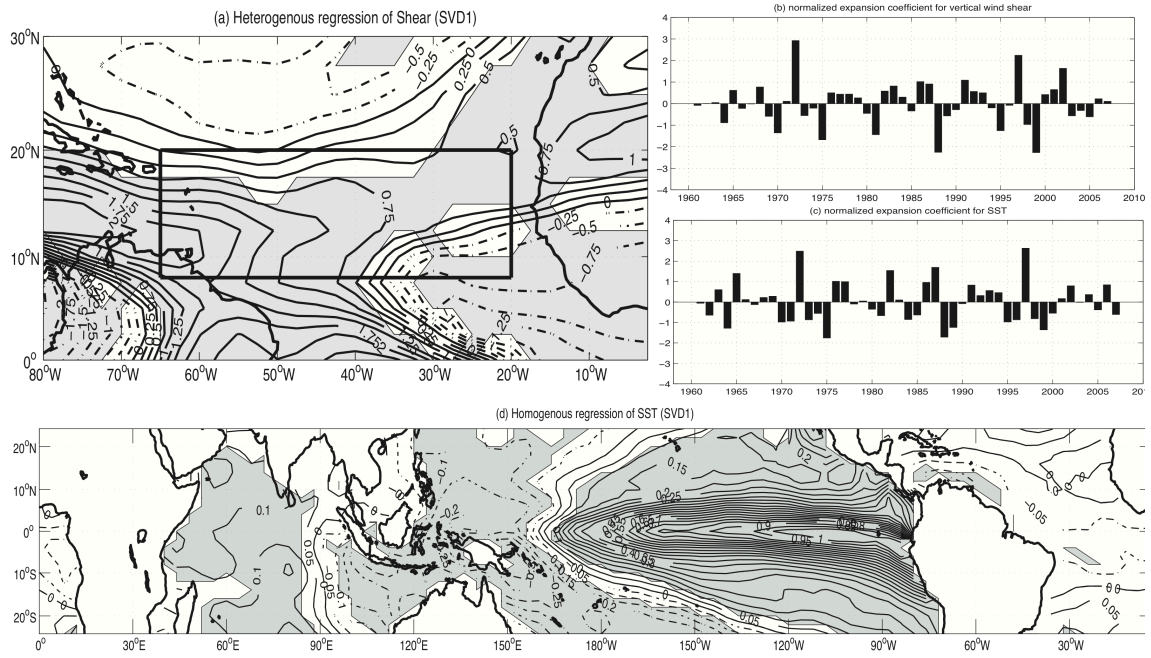
Figure 3.6. SVD analysis for band-pass filtered datasets. (a) Heterogeneous regression of vertical wind shear and (d) homogeneous regression of SST on the normalized first SVD expansion coefficients for SST. Shading denotes the 95% significance level. The normalized first SVD expansion coefficients for (b) vertical wind shear and (c) SST.

III.D.4. SST forcing on dipole mode at multi-decadal time scale

On the multi-decadal timescale, the effect of global SST on the northern tropical Atlantic vertical wind shear is much weaker than on the interannual timescale (Fig. 3.7). Although the significance level is low, the dipole mode of vertical wind shear still can be seen from the heterogeneous regression of vertical wind shear on the leading SVD expansion coefficients for SST (Fig. 3.7a). Examining the leading SVD expansion

coefficients for SST (Fig. 3.7c), we can infer that the vertical wind shear over the northern tropical Atlantic was in the *strong phase* from 1970 to 1995. With stronger vertical wind shear over the northern tropical Atlantic from 1970 and 1995, fewer hurricanes occurred over this period, and vice versa for the decades with weak tropical Atlantic vertical wind shear (Goldenberg et al. 2001). Moreover, the leading SVD mode captures the 92.1% of the total covariance.

There appears to be some relationship between the north Pacific SST and north Atlantic SST and the vertical wind shear over the northern tropical Atlantic. From mid-1970's to mid-1990's, together with the *stronger phase* of dipole mode (Fig. 3.7a), there are colder SST anomalies over the North Pacific and warmer SST anomalies over the eastern tropical Pacific, which resembles the Pacific Decadal Oscillation (PDO) signal (Fig. 3.7d).

In contrast to the remote SST forcing on the dipole shear mode on the interannual timescale, the local north Atlantic SST forcing stands out on the multi-decadal timescale. A colder North Atlantic SST is associated with the *strong phase* of dipole mode (Fig. 3.7d). This SST mode over the northern Atlantic resembles the Atlantic Multidecadal Oscillation (AMO) (Kerr 2000; Knight et al. 2005, 2006b). Before 1970 and after 1995, the North Atlantic is in the *warm phase* of AMO with warmer north Atlantic SST. While from 1970 to 1995, it switches to the *cold phase* of AMO with cooler North Atlantic SST. During the *cold phase* of AMO, the Inter-Tropical Convergence Zone (ITCZ) shifts to the south (Knight et al. 2006b). As a result, the trade wind at lower level increases over the northern tropical Atlantic (Knight et al. 2006b) and the upper level jet

shows westerly anomaly during the *cold phase* of AMO (Kossin and Vimont 2007).
Therefore, during the *cold phase* of AMO, there are stronger trade winds at lower level
and stronger westerlies at upper level over the western tropical Atlantic. As a result, the
northern tropical Atlantic is dominated by strong vertical wind shear during the *cold
phase* of AMO.

Figure 3.7. SVD analysis for low-pass filtered datasets. (a) Heterogeneous regression of
vertical wind shear and (d) homogeneous regression of SST on the normalized leading
SVD expansion coefficients. Shading denotes the 95% significance level. Also, the
normalized leading SVD expansion coefficients for (b) vertical wind shear and (c) SST.
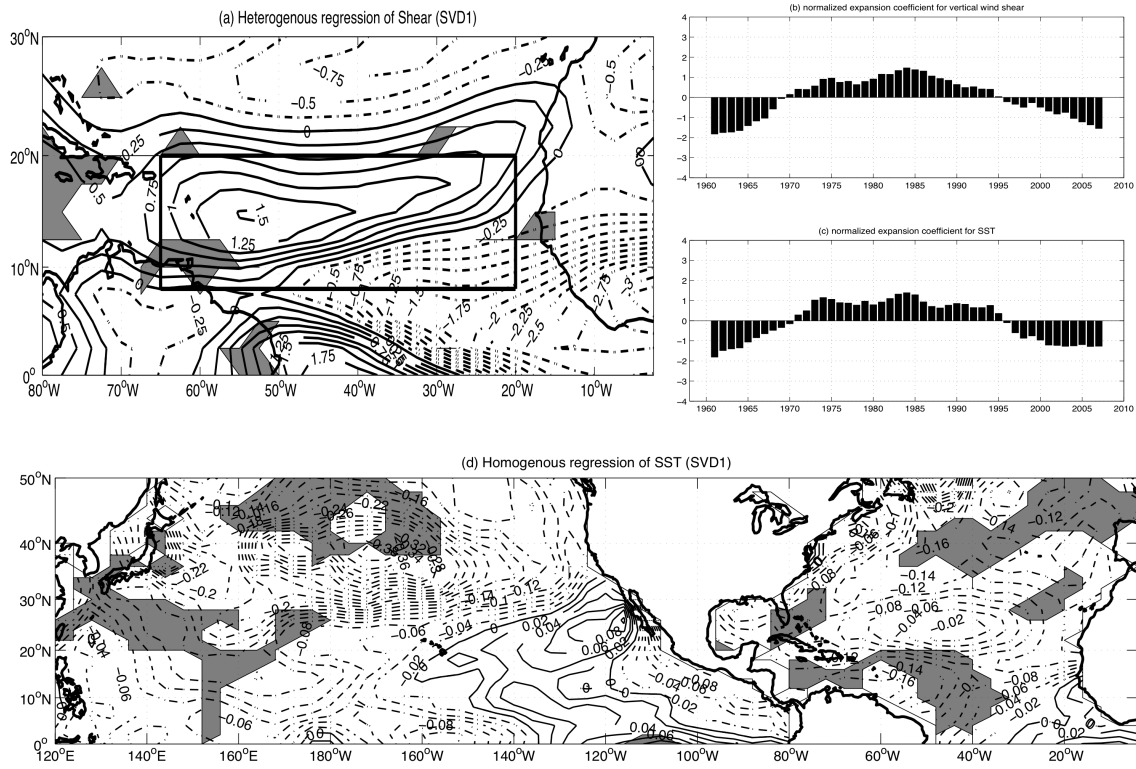
III.E. Internal atmospheric mode

In the previous sections, we found that the variation of vertical wind shear over the northern tropical Atlantic is dominated by a dipole mode. This dipole shear mode covaries with tropical SST on the interannual timescale, and extratropical SST on the multi-decadal timescale. In this section we address the question of whether this dipole shear mode is an internal atmospheric mode, i.e., could it exist in the absence of any boundary SST forcing?

As the Pacific SST is the dominant influence on the tropical Atlantic wind shear, we first attempt to answer this question by analyzing the vertical wind shear during non-ENSO years. Based on the JASO mean Nino3 index from 1950 to 2012, there are 28 non-ENSO years selected with SST anomaly less than 0.5°C (1952, 1953, 1958, 1959, 1960, 1962, 1966, 1968, 1974, 1977, 1978, 1979, 1980, 1981, 1983, 1984, 1986, 1989, 1990, 1992, 1993, 1994, 1996, 1998, 2000, 2001, 2005 and 2011).

For these 28 non-ENSO years, the vertical wind shear variability over the northern tropical Atlantic is characterized by a dipole mode as the leading EOF as well (Fig. 3.8a). Although the influence of ENSO is weak during the non-ENSO years, the vertical wind shear still shows opposite-signed variations over the western and eastern tropical Atlantic. Moreover, this dipole shear mode explains about 50% of the total variance, which is well separated from the higher order modes (Fig. 3.8b). This indicates that even without ENSO forcing, vertical wind shear anomalies over the western tropical Atlantic tend to be anticorrelated with those over the eastern tropical Atlantic.
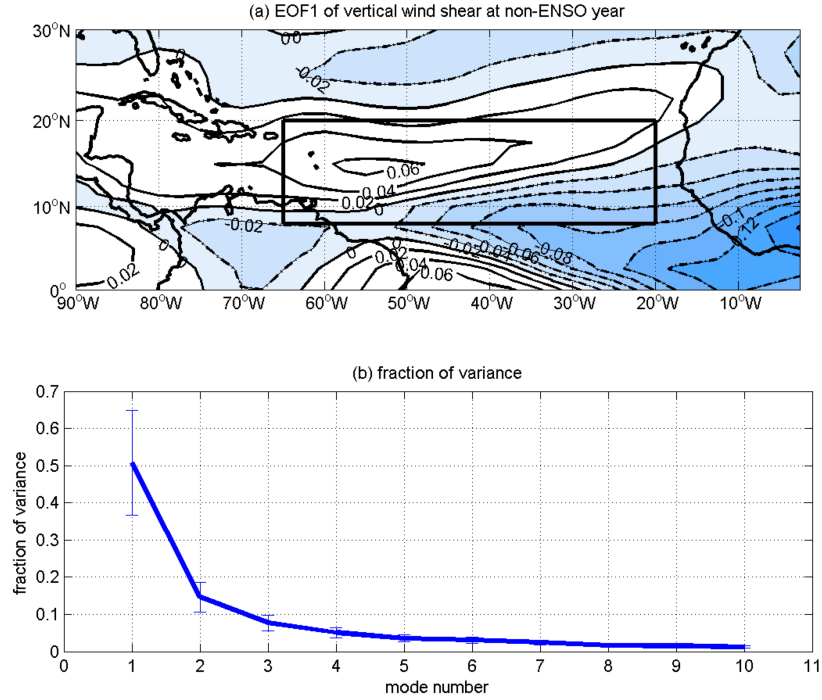
Figure 3.8. (a) The first EOF mode of vertical wind shear during 28 non-ENSO years and (b) the fraction of variance explained by the first 10 EOF modes.

To address the question of internal variability from a modeling perspective, we carried out an uncoupled numerical model experiment by forcing the CAM3 with a repeating climatological annual cycle SST for 50 years (the CAM-Climatology-SST run). (We ignore the first 5 years simulations in our analysis, to account for any possible spin-up effects.) In this experiment, there is no variation in boundary SST other than the seasonal cycle. Hence any variations in the northern tropical Atlantic shear must be associated with internal atmospheric variability.

Figure 3.9 shows the leading EOF mode and principal component for the simulated vertical wind shear in this experiment. The first EOF of vertical wind shear without SST

forcing is well separated from the remaining EOFs, satisfying the North criterion, and accounts for a significant fraction of the variance (Fig. 3.9b). Moreover, as the atmosphere has shorter memory than the ocean, the first principal component exhibits higher frequencies of variability than the observed interannual or multi-decadal variations (Fig. 3.9c).
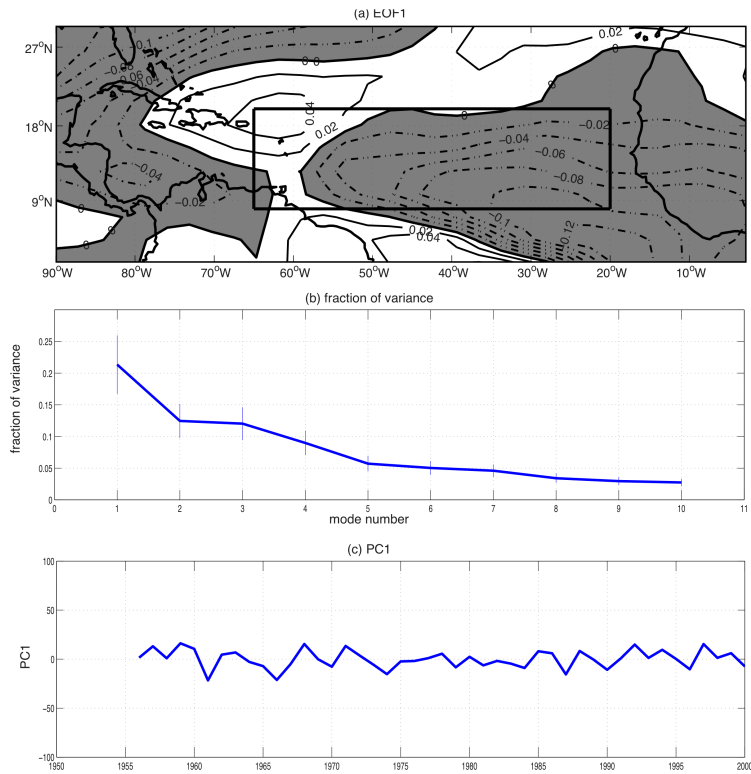
Figure 3.9. (a) The leading EOF mode of vertical wind shear in the CAM3-Climatology-SST experiment, (b) the fraction of variance for the first 10 modes with standard error (vertical lines), and (c) the leading PC.

The leading EOF of simulated vertical wind shear exhibits a dipole structure over the northern tropical Atlantic, but with slightly different spatial pattern as compared to the observed mode (Fig. 3.9a). In the *strong phase* of dipole mode, a strong vertical wind shear belt extends from the Puerto Rico to the Western Sahara. A weak vertical wind shear belt extends from the western Africa to the southeastern MDR. This further indicates that even without boundary SST forcing, the vertical wind shear over the northern tropical Atlantic exhibits a dipolar pattern. However, the detailed spatial structure of this uncoupled dipole shear mode is slightly different when compared to the observed dipole shear mode (Fig. 3.8a). The southern lobe of the dipole is more dominant in the uncoupled case, and the northern lobe is weaker. This suggests air-sea coupling is not required to explain the existence of the dipole mode, but is required to explain the detailed spatial structure of the mode.

In order to further explain the origins of the dipolar spatial structure in vertical wind shear variability, vertical wind profiles over the MDR are compared (Fig. 3.10). The dipole shear mode over the MDR exhibits two centers: one located in the northwestern MDR (12.5°N-20°N, 45°W-65°W) and the other in the southeastern MDR (12.5°N-20°N, 45°W-65°W). The JASO mean zonal wind (u) was averaged over the two centers from 1000hPa to 100hPa (Fig. 3.10). (Compared to the zonal wind, the magnitude of meridional wind and its contribution to vertical wind shear variability is much smaller, and is therefore not shown.) We consider the difference of zonal wind between two centers of the dipole shear mode.

In the climatological mean, the largest difference in the zonal flow between the

northwestern MDR and the southeastern MDR occurs at the upper levels (Fig. 3.10). The zonal wind over the northwestern MDR is eastward, and is controlled by the subtropical westerly jet (Fig. 3.10a). The upper level wind over the southwestern MDR is westward, and is influenced by the tropical easterly jet (Fig. 3.10b). At the lower levels, both regions are characterized by climatological easterly trade winds, although the winds over the southwestern MDR are much weaker below 800hPa (Fig. 3.10b).

In order to analyze variability, 10 ENSO events during the period from 1989 to 2008 are selected to illustrate vertical wind shear variations. There are 5 El Nino events (1991, 1994, 1997, 2002, 2004) and 5 La Nina events (1995, 1998, 1999, 2000, 2007), which are shown as thin blue lines and red lines respectively in Figure 17. On average, at the lower levels, the trade wind increases during the El Nino events and decreases during the La Nina. While at the upper levels, the dominant influence of ENSO causes a westerly anomaly during the El Nino events and an easterly anomaly during the La Nina events.

Considering the mean and anomalous flow together, over the northwestern MDR, the upper level westerlies increase along with the westerly anomaly during the El Nino events (Fig. 3.10a). Hence, the vertical wind shear increases during the El Nino over the northwestern MDR. However, over the southwestern MDR, with a similar westerly anomaly, the upper level easterlies decrease during the El Nino events (Fig. 3.10b). As a result, the vertical wind shear over the southeastern MDR decreases during El Nino events, which is the opposite of that over the northwestern MDR. The opposite holds for the La Nina events.

This implies that under different prevailing jets over the northwestern and the southeastern MDR, the vertical wind shear demonstrates opposite-signed variations. Due to the superposition of mean flow and anomalous flow, even with the same-signed anomalous flow, opposite-signed prevailing mean flows can give rise to opposite-signed vertical wind shear variations at the eastern and western tropical Atlantic. Over the northwestern MDR, the upper level and the low level are controlled by the westerly jet and eaterly trade winds respectively. While over the southeastern MDR, the same trade winds prevail at the lower levels, but an easterly jet prevails at the upper level. As a result, the climatological mean vertical wind shear over the northwestern MDR is stronger than that over the southeastern MDR. Furthermore, assuming we have the same easterly anomaly at the upper level over the entire tropical Atlantic, the westerlies over the northwestern MDR will decrease, while the easterlies over the southeastern MDR will increase. As a result, the vertical wind shear is reduced over the northwestern MDR, but increased over the southeastern MDR. Therefore, the variation of northern tropical Atlantic vertical wind shear shows a dipole mode, as a result of the inherent nonlinearity in the definition of the wind shear.
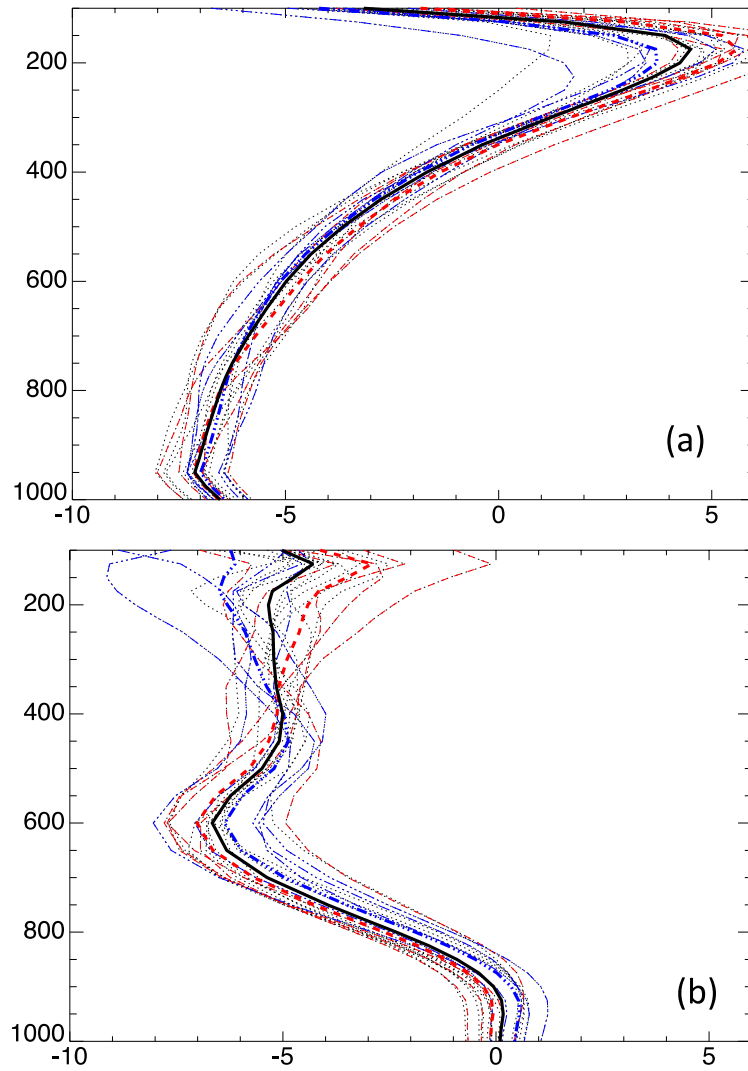
Figure 3.10. The JASO mean vertical wind profile averaged over (a) the northwestern
MDR (12.5°N-20°N, 45°W-65°W) and (b) the southwestern MDR (7.5°N-15°N, 20°W-
40°W) from 1989 to 2009. Thick black lines represent the 21-year climatology, blue
dash-dot lines represent the La Nina events and red dash lines represent the El Nino
events. Blue thick dash-dot lines represent the average of the La Nina events and red
thick dash lines represent the average of the El Nino events.
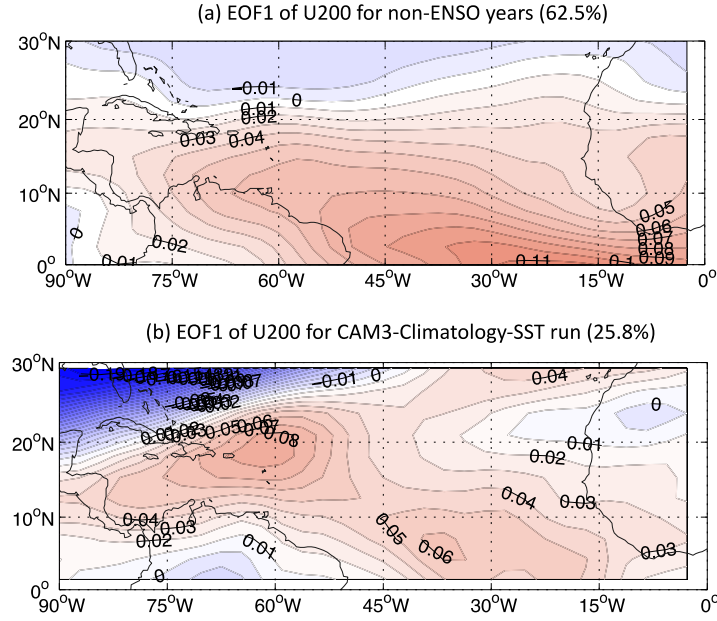
Figure 3.11. The first leading EOF mode of zonal wind at 200hPa (a) for the non-ENSO years and (b) for the CAM3-climatology-SST run.

Now we ask the question of whether this dipole mode of vertical wind shear variation is simply the result of variation of mean flow at 200hPa? To answer it, we computed the dominant EOF modes of zonal wind at 200hPa for the non-ENSO years and for the CAM3-climatology-SST run (Figure 3.11). The leading EOF modes in both cases are well separated from the remaining modes, by North's criterion. The first EOF mode of zonal wind at 200hPa for the non-ENSO year shows a monopolar mode over the northern tropical Atlantic (Fig. 3.11a), indicating the variation for zonal wind is not opposite in the two sides of the tropical Atlantic. Similar to the monopolar mode for the non-ENSO years, the dominant mode for the CAM3-climatology-SST run also exhibits a

similar variation of the subtropical jet and tropical easterly jet at 200hPa (Fig. 3.11b). These results indicate that the dipole pattern of vertical wind shear variations is due to the structure of the mean flow, and not due the structure of the anomalous flow.

III.F. Conclusions

In this chapter, the variability of vertical wind shear, defined as the magnitude of wind vector difference between 850hPa and 200hPa, is analyzed over the northern tropical Atlantic, especially over the MDR (8°N-20°N, 65°W-20°W). At different time scales, from daily to seasonal, the probability density function of vertical wind shear shows nongaussian distribution. As the definition of vertical wind shear involves a nonlinear operation on wind vectors at different levels, different PDFs are obtained when two different methods of computing the vertical wind shear, one where the shear computation is carried out after the time-averaging and one where it is carried out before. On the daily timescale, the differences between the two methods are small. But as the time scale gets longer, the PDF for the vertical wind shear calculated with the first method deviates further from the Gaussian distribution, with larger difference of the mean, STD, skewness and Kurtosis among different sampling groups. However, the PDF for the vertical wind shear calculated using the second method is closer to the Gaussian distribution, with little change of the mean, STD, skewness and Kurtosis for different time scales.

Based on the EOF analysis of NCEP and ECMWF reanalysis data, we find that there is a robust dipole mode of vertical wind shear variation over the northern tropical

Atlantic at different time scales. This dipole mode indicates that the vertical wind shear variation over the western tropical Atlantic is opposite to that over the eastern tropical Atlantic. During the *strong phase* of dipole mode, there is stronger vertical wind shear over the western tropical Atlantic, and weaker vertical wind shear over the eastern tropical Atlantic. Similar to the observations, simulated vertical wind shear in IPCC models also demonstrate the dipole mode, with a significant spatial correlation with the observed dipole mode. This indicates that the dipole mode of vertical wind shear variation is a robust feature of both observations and numerical model simulations.

On the interannual timescale, the SST variability in the Pacific and Indian Oceans affect the dipole shear mode. Warm SST anomalies over the eastern Pacific generate anomalous westerly flow at upper level, which leads to the stronger vertical wind shear over the western tropical Atlantic. Warmer Indian Ocean SST anomalies cause a weakening of the tropical Easterly jet, and further contribute to weakening vertical wind shear over the eastern tropical Atlantic. On the multi-decadal timescale, there is no significant influence of tropical SST on the dipole mode. However, the North Pacific SST and North Atlantic SST are correlated with tropical vertical wind shear, indicating the influence of modes of decadal variability such as the PDO and the AMO.

Even in the absence of the ENSO influence, such as during non-ENSO years, vertical wind shear variability over the northern tropical Atlantic still demonstrates a dipole structure. To investigate this further, we carried out an uncoupled numerical model simulation where CAM3 was forced with repeating climatological annual cycle of SST. It turns out that the internal atmospheric variability is sufficient is able to generate

58

a dipole mode of vertical wind shear variability over the northern tropical Atlantic, albeit with slightly different spatial structure as compared to observations. This suggests that the dipole shear mode could be an intrinsic mode of atmospheric variability.

It is noteworthy that the upper level jets are the main contributor to the dipole mode of vertical wind shear. Analysis of vertical wind profiles shows that there are prevailing westerlies over the northwestern MDR and prevailing easterlies over the southeastern MDR, which are under the influence of the subtropical jet and tropical easterly jet, respectively. Due to the nonlinear superposition of the mean flow and anomalous flow, even with a monopolar structure in the flow variability associated with the upper level jets, the vertical wind shear over northern tropical Atlantic can exhibit a dipolar structure.

In general, the nonlinearity inherent in the definition of vertical wind shear implies that not only the anomalous flows but also the mean flows are important in determining variability of vertical wind shear. The dipolar structure vertical wind shear variability over the northern tropical Atlantic further highlights the importance of mean flow in modulating climate variability.

CHAPTER IV

INFLUENCE OF MEAN SURFACE WIND SPEED ON DECADAL VARIABILITY

IV.A. Introduction

The mean surface wind plays a vital role in climate variability, as has been shown in the literature (Richter et al. 2012, Grodsky et al. 2012). To study the reasons for poor simulations of tropical Atlantic variability, Richter et al. (2012) carried out a set of sensitivity experiments using the Geophysical Fluid Dynamics Laboratory (GFDL) coupled GCM, and found that the equatorial SST bias over the eastern tropical Atlantic is due to weaker equatorial easterlies during boreal spring. By replacing the weaker simulated easterlies with observed surface wind, a more realistic SST simulation was obtained over the tropical Atlantic. In another study (Grodsky et al. 2012), the twentieth-century simulation of the Community Climate System Model, version 4 (CCSM4) was shown to have overestimated surface wind over tropical Atlantic. As a result, there is additional cooling north of the equator, which leads to a cooler SST, with the opposite effect leading to warmer SST south of the equator.

An important mechanism for the influence of surface wind on climate variability is the Wind-Evaporation-SST (WES) feedback (Xie and Philander, 1994; Chang et al., 2001; Xie, 1999; Chiang and Bitz 2005; Mahajan et al., 2009, 2010). It is a positive thermodynamic feedback between surface wind, evaporation, and SST. Considering the cross-equatorial SST gradient, for example, over the eastern tropical Pacific, when there is a warm SST anomaly north of the equator and a cold SST anomaly south of the

equator. This SST gradient generates a northward cross-equatorial anomalous wind. When flowing across the equator, the northward wind anomaly is acted upon by the Coriolis force. The northward wind anomaly in the southern hemisphere turns northwestward, while the anomaly in the northern hemisphere turns northeastward. When this anomaly is superposed on the prevailing trade winds, the wind speed south of the equator increases, while the wind speed north of the equator decreases. As the evaporation and the associated latent heat release are proportional to the wind speed, the evaporation is enhanced in the southern hemisphere and attenuated in the northern hemisphere. As a result, the colder SST anomaly in the southern hemisphere becomes colder, while the warmer SST in the northern hemisphere becomes warmer, resulting in a positive feedback.

The WES feedback has been used to explain many phenomena over the tropical oceans. Over the eastern tropical Pacific, with the cross-equatorial SST gradient, the WES feedback is used to explain the northward-displacement of the InterTropical Convergence Zone (ITCZ) (Xie and Philander, 1994; Xie 1996). Over the tropical Atlantic, where the cross-equatorial SST gradient also exists, the WES feedback plays a role in modulating a tropical Atlantic inter-hemispheric gradient mode (previously known as the "dipole mode") (Chang et al. 1997). Other than its local influence on the climate variability, the WES feedback also has non-local impacts on climate (Xie 1994; Chiang and Bitz, 2005; Mahajan et al. 2009, 2010), such as the westward propagation of equatorial SST anomaly (Xie 1994, Mahajan et al. 2009) and equatorward propagation of high-latitude anomalies (Chiang and Bitz, 2005; Mahajan et al. 2010). In projections

of the global warming scenario, over the subtropical southeast Pacific where trade wind prevails, cold SST anomalies can cause an enhanced trade wind. This enhanced trade wind increases the evaporation and latent heat release, leading to further cooling of the SST (Xie et al., 2010). The key feature of the WES feedback is the superposition of mean wind and anomalous wind. Anomalous winds of the opposite sign superposed on same mean winds give rise to latent heat anomalies of the opposite sign, resulting in positive SST feedback.

In this chapter, we consider the possible role of the WES feedback on climate predictability, which is usually associated with modes such as the Pacific Decadal Oscillation (PDO, Trenberth and Hurrel 1994), and the Atlantic Multi-decadal Oscillation (AMO, Knight et al. 2005). Based upon CMIP3 control runs, Boer and Lambert (2008) find that long timescale predictability mainly exists over the oceans, particularly in the middle latitudes. Due to the larger thermal inertia of the ocean, long-term 'memory' in the ocean serves as the source for decadal predictability in the atmosphere. Hence, Smith et al. (2007) proposed an improved decadal prediction system by initializing a coupled ocean-atmosphere model with assimilated atmospheric and oceanic observations.

There are three sources of uncertainty in climate prediction (Hawkins and Sutton 2009). The first source is the internal variability, which causes large uncertainties in climate prediction at short timescales. Improving the accuracy of initial conditions can reduce the errors associated with internal variability. The second source of prediction uncertainty is model error, which is associated with numerical discretization and

parameterization error. The third error source is the scenario uncertainty, which is related to the boundary conditions for the projection of future climate. The shorter-term interannual climate prediction relies on the initial condition ('initial value problem'), while the longer centennial timescale climate prediction depends on the boundary forcings ('boundary value problem') (Meehl el al. 2009). Decadal prediction fills the gap between short-term and long-term prediction, by considering both initial conditions and the boundary forcings.

In this chapter, we analyze a set of numerical experiments carried out to study decadal predictability in the climate system. We assess the role of the WES feedback by carrying out sensitivity experiments where the mean surface frictional velocity is prescribed, thus eliminating the influence of mean surface wind on surface flux variability. In section B, the numerical model set up is described and a modified version of the Hasselmann stochastic climate model is introduced. In section C, the forecasts of SST are analyzed to quantify the decadal prediction skill and the influence of WES feedback. The effect of WES feedback is further analyzed using signal-to-noise ratio metrics section D. Finally, conclusions are presented in section E.

IV.B. Methods

IV.B.1. Numerical model setup

For decadal prediction, initial conditions and boundary conditions are both considered important. To assess the role of the WES feedback, we use a simplified coupled model where an atmospheric GCM, the Community Atmospheric Model version

3 (CAM3) is coupled to a slab ocean model, rather than use a comprehensive coupled general circulation model. The horizontal model resolution is 2.815° latitude by 2.815° longitude, which corresponds to a spectral resolution of T42. The mixed-layer slab ocean model assumes a simple balance between mixed layer heat content, surface heat fluxes and a flux correction term representing oceanic heat transport.

The decadal prediction experiments were initialized at each January from 1951 to 1999, with the observed oceanic initial condition and a perturbed atmospheric initial condition. For the oceanic state, for each January, CAM3 is initialized with observed SST from 1951 to 1999. Furthermore, three sets of perturbed atmospheric initial conditions for 49 January's are generated from a branch run of CAM3. These are used to initialize three ensemble members of decadal prediction for January from 1951 to 1999, but using same observed SST initial condition. Each ensemble contains 49 hindcasts, which are 10-year predictions from 49 initial times.

The boundary conditions considered in our study are the Greenhouse Gas (GHG) forcing, solar constant, ozone mixing ratio and stratospheric volcanic aerosols. In order to make true predictions, without using information from the future, we linearly extrapolated the external forcings 10 years into the future, using information for the 10 years preceding the initial time. For the GHG forcing, the linear trend for the preceding 10-year period is computed and used to extrapolate into the future. Figure 18a shows an example of the projected GHG forcing from 1975 to 1984 for the hindcast starting from January 1975. This GHG forcing starts from the observed GHG level at 1975, and then increases with the trend computed from the previous 10-year period (Fig. 4.1a). Thus, a

10-year GHG forcing time series is generated based on the information from 1965 to 1974.

Instead of the annual data that was used to extrapolate the GHG forcing, monthly data are used for the volcanic aerosol forcing. Between 1950 and 2000, there were several major volcanic eruptions, such as the eruption of Mount Pinatubo at April 1991 (Fig.4.1b). After a volcanic eruption, the volcanic aerosol concentration decays slowly. So if there is a volcanic eruption at an initial year, the volcanic aerosol is projected as an exponential decay with an e-folding time of 1 year. Figure 4.1b shows an example of the volcanic forcing for the 1992 hindcast. After the Pinatubo eruption at 1991, considerable amount of volcanic aerosol is still present in the atmosphere in January 1992. So the volcanic aerosol is presumed to be decay exponentially from its initial level at January 1992, with a 1-year e-folding damping time (Fig. 4.1b). If there is no volcanic aerosol at the initial time, the volcanic aerosol projection for the future 10 years is assumed to be zero.
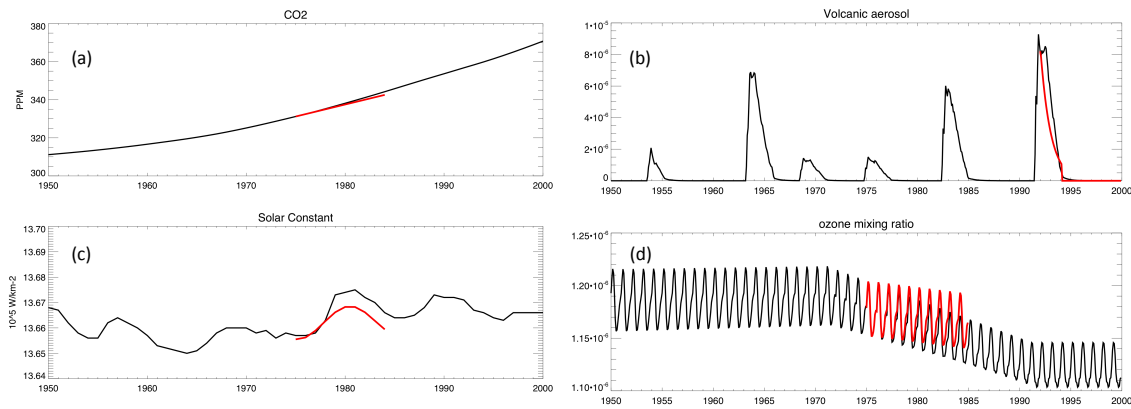
Figure 4.1. (a) Observed annual GHG concentration (black line) and projected annual GHG concentration for the 1975 hindcast (red line). (b) Observed volcanic aerosol (black line) and projected volcanic aerosol for the 1992 hindcast (red line). (c) Observed annual solar constant (black line) and projected annual solar constant for the1975 hindcast (red line). (d) Observed ozone mixing ratio (black line) and projected ozone mixing ratio for the 1975 hindcast (red line)

Similar to the prescribed GHG forcing, the projected 10-year solar constant also uses the trend from previous 10 years. But as the solar constant has an 11-year cycle (Fig. 4.1c), the historical 10-year dataset prior to initial time is fitted with a sinusoidal function with an 11-year period, in addition to the trend. Then this sinusoidal fitted function is extrapolated into the future 10-year period to prescribe the solar constant (Fig. 4.1c). The monthly ozone mixing ratio prescribed in the CAM3 has latitudinal and vertical distribution, as well as temporal variation. Figure 4.1d shows the globally and vertically averaged ozone mixing ratio. As the ozone mixing ratio shows a clear seasonal

cycle, the ozone mixing ratio is fitted with sinusoidal function for the seasonal cycle, as well as a linear trend. Then the future 10-year ozone mixing ratio is linearly extrapolated based upon the previous 10-year linear trend, with a superimposed annual cycle (Fig. 4.1d).

The control experiment in our study consists of 49 hindcasts of decadal prediction with the CAM3 coupled to a slab ocean (the SOM run). In the control run, the latent and sensible heat fluxes over the ocean are computed using a standard bulk formulation:

$$Latent\ heat(E) = \rho u^* L_{vap} C_e \Delta q$$
$$Sensible\ heat(H) = \rho u^* C_p C_h \Delta \theta$$

Here, ρ is the density, L_{vap} is the latent heat of evaporation, Cp is the specific heat capacity of water, Δq is the specific humidity difference between the surface air humidity and the saturation specific humidity at surface temperature, and $\Delta \theta$ is the potential temperature difference between the atmosphere and ocean surface. The surface friction velocity (turbulent velocity scale) is $u^* = C_D^{1/2} |\Delta v|$ (USTAR), which is the product of transfer coefficient of momentum and wind speed. At each time step, CAM3 calculates the surface wind speed, updates the surface friction velocity, and then calculates the latent and sensible heat flux. So the surface friction velocity exhibits a high frequency variation in the SOM run.

For studying the WES feedback, we follow the mechanistic approach used by Mahajan et al. (2009, 2011). Instead of allowing the model to update the frictional velocity at each time step, we prescribe the climatological annual cycle surface frictional velocity (USTAR) for the computation of latent and sensible heat flux. As a result, the

evaporation is not affected by any changes in the surface wind, and the WES feedback can be suppressed for sensitivity experiments. In order to test the impact of switching off the WES feedback, the annual cycle of SST over the tropical Pacific (4°N-4°S) is analyzed as in Mahajan et al. (2009). For the control simulation with the WES feedback, it shows a clear westward propagation of eastern Pacific SST signal. When the climatological annual cycle of USTAR is prescribed in CAM3, the simulated SST anomaly over eastern tropical Pacific does not propagate westward any more (Mahajan et al. 2009). We can therefore carry out a sensitivity experiment for decadal prediction where the WES feedback is turned off (the WESOFF run).

In summary, two sets of decadal prediction experiments are carried out: the SOM run (including the WES feedback,) and the WESOFF run (without the WES feedback). Each decadal prediction experiment has 3 ensemble members, with 3 sets of perturbed observed atmospheric condition and same observed SST as the initial conditions. For each ensemble member, we have 49 hindcasts of 10-year prediction starting at each January from 1951 to 1999 (Fig. 4.2). In order to compare with observations, the first year prediction in the 49 hindcasts can be presented as a time series from January 1951 to December 2000, which is called the first year prediction. Similarly, we can present the time series of the second to the 10th year prediction. Table 4.1 shows the prediction lead times and starting years for each lead time..
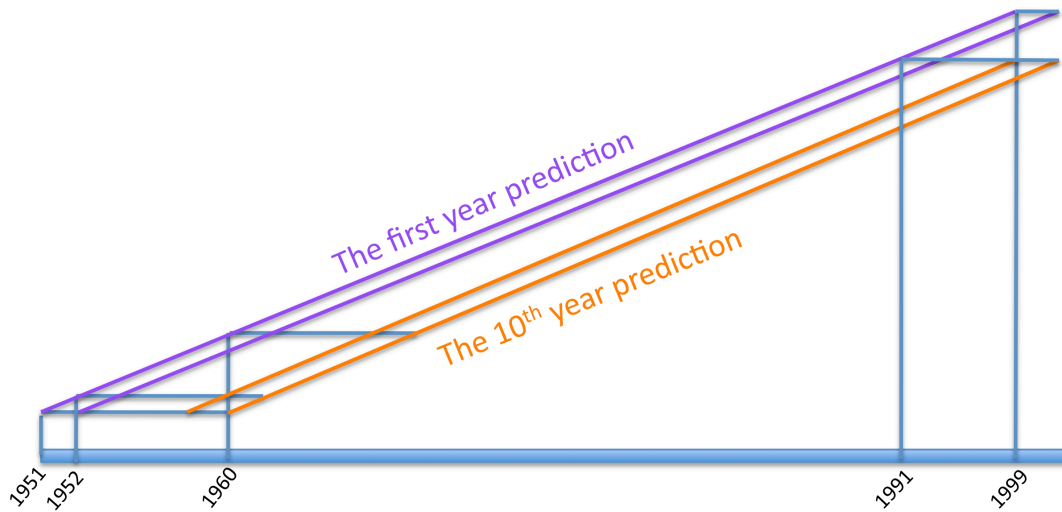
Figure 4.2. Schematic illustration of the 49 hindcasts from 1951 to 1999 and the time series of the 1st year and the 10th year prediction

Table 4.1. Summary of prediction lead times (years) and the starting years

Lead time	1	2	3	4	5	6	7	8	9	10
Starting year	1951-1999	1952-2000	1953-2000	1954-2000	1955-2000	1956-2000	1957-2000	1958-2000	1959-2000	1960-2000

IV.B.2. Modified Hasselmann model

The Hasselmann model is a simple model of the climate variability driven by air-sea interaction (Frankignoul and Hasselmann, 1977). Unlike the general circulation models, which are deterministic dynamical systems, the Hasselmann model is a stochastic system, based upon physical conservation of energy at the air-sea interface.

The governing equation of the oceanic mixed layer describes the balance between SST change and net surface heat fluxes, which is shown in the equation:

$C_p H \dfrac{dT}{dt} = SW - LW - \lambda(T - T_a)$, where T represents the SST or the mixed layer temperature, C_p is the heat capacity, H is the mixed layer depth, SW denotes the net surface shortwave radiation and LW denotes the net longwave radiation.

For the latent heat flux, the bulk formulation can be simplified as the following:

$$E = L\rho C_E \, | \Delta v \, | (q_s(T) - q_a(T_a))$$
$$= L\rho C_E \, | \Delta v \, | (q_s(T) - RH \cdot q_s(T + T_a - T))$$

Using the Clausius-Clapeyron equation, saturation humidity of air temperature can be expressed as the following:

$$q_s(T_a) = q_s(T + T_a - T)$$
$$= q_s(T) \cdot \exp\{ -\frac{L}{R_v}(\frac{1}{T} - \frac{1}{T_a - T}) \}$$
$$\approx q_s(T) \cdot \exp\{ -\frac{L}{R_v T}(1 - (1 - \frac{T_a - T}{T})) \}$$
$$= q_s(T) \cdot \exp\{ -\frac{L}{R_v T^2}(T_a - T) \}$$

where, R_v is the gas constant for water vapor, $L/(R_v T^2) \sim 0.06\text{K}^{-1}$ (Xie et al. 2010). As a result, the latent heat flux can be approximated simply as a function of (T-Ta). Here, T

denotes SST and Ta denotes air temperature. Thus, the $-\lambda(T - T_a)$ term in the governing equation represents the effect of latent and sensible heat flux, which represents the damping effect of atmospheric feedback on the SST.

After linearizing the governing equations, we obtain the Hasselmann model equation $\dfrac{dT'}{dt} = -\mu T' + N$, where μ represents the linear damping coefficient and N represents the random atmospheric forcing. In our study, switching the WES feedback on or off affects the latent and sensible heat flux. Therefore, the Haaselmann model can be used as a diagnostic tool to evaluate the change in surface fluxes and the impact of the WES feedback.

For recent climate variability, external forcings contribute to the evolution of SST, as well as the internal stochastic variations. Figure 4.3 shows the observed global (60S-60N) annual-mean SST from 1950 to 2000, as well as the GHG forcing and the variations of the solar constant, ozone concentration and volcanic aerosol concentration. The SST exhibits correlations with the GHG forcing and solar constant. The SST shows a warming trend, while the GHG forcing and the solar constant also display an increasing trend. The classical Hasselmann model assumes a stationary climate. To take climate trends into account, we add an external forcing term F to the model as follows:

$$\frac{dT'}{dt} = -\mu T' + N + F$$
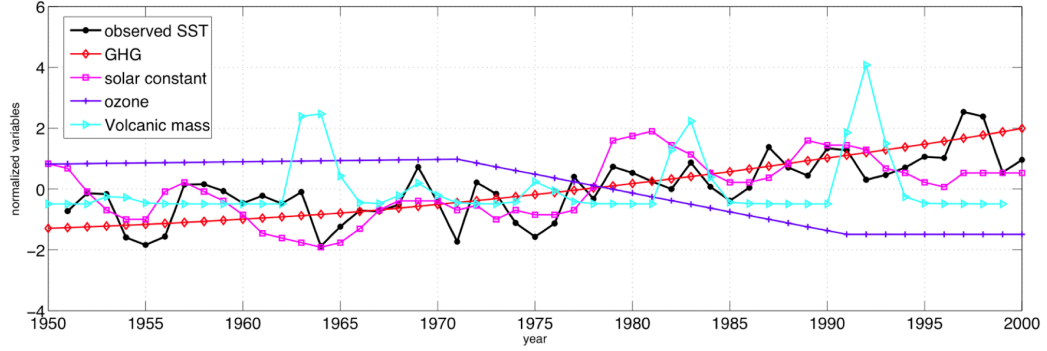
Figure 4.3. The observed global annual SST (black), the GHG forcing (red), solar constant (purple), ozone concentration (blue) and Volcanic aerosol concentration (cyan).

As the SST trend is strongly correlated with the forcing terms, especially the GHG forcing, we assume that the forcing term F results in a linear SST trend. Therefore we express the time evolution of SST as a linear combination of a stochastic anomaly, the mean value and a trend as follows:

$$T = T' + \overline{T} + T_{trend}$$

Hence, we obtain a modified model of the evolution of SST anomalies as following:

$$\frac{dT'}{dt} = -\gamma T' + N$$

Although the classical Hasselmann model and the modified model equations have same form, the physical interpretation is different. In the classical Hasselmann model, the SST anomaly is computed relative to the mean SST (Fig. 4.4a), while in the modified model, the anomaly is computed relative to the sum of mean SST and SST trend (Fig. 4.4b).
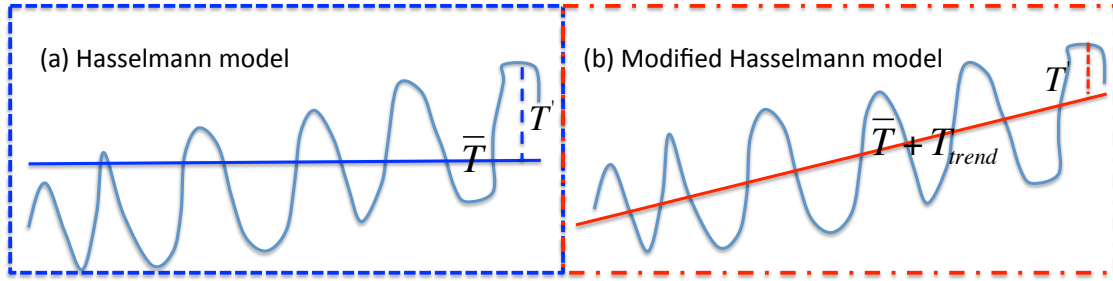
Figure 4.4. Schematic illustration of (a) the Hasselmann model and (b) the modified Hasselmann model

In practice, the damping coefficients for the Hasselman model and the modified model can be computed using the 1-month lagged correlation coefficients. For the Hasselman model or the modified model $\frac{dT}{dt} = -\mu T + N$, we can have a solution $T(t + t_0) = e^{-\mu(t-t_0)} T(t_0) + N(t)$. Then the covariance of T(t+t$_0$) and T(t) gives:

$$< T(t + t_0), T(t) >= e^{-\mu(t-t_0)} < T(t_0), T(t_0) > + < N(t), T(t_0) >$$

As $< N(t), T(t_0) >= 0$, we have $e^{-\mu(t-t_0)} = \frac{< T(t + t_0), T(t) >}{< T(t_0), T(t_0) >} = r(\tau)$. Here, $\tau = t - t_0$ is the lag time interval. Using the lagged auto correlation $r(\tau)$, the damping coefficient can be estimated as: $\mu = -\ln(r(\tau))/\tau$.

In order to validate the models, monthly SST from the Hadley center (HadISST) is used to first compute the damping coefficient and then diagnose the evolution of global mean SST anomaly. For the Hasselman model, the seasonal cycle of SST is removed

first, then the climatological mean SST is removed. The damping coefficients are then calculated from the lag-1 auto correlation coefficient. However, for the modified Hasselmann model, the SST trend is also removed before calculating the lag-1 auto correlation. The global pattern of the damping coefficients in the modified model is quite similar as that in the classical Hasselmann model (not shown). It shows weak damping over tropics, especially over the eastern tropical Pacific.

Next, the averaged SST between 60°S and 60°N is diagnosed in the models. In both models, the random atmospheric forcing part is unpredictable, but averages to zero in the ensemble mean. However, the damping term can be used to diagnose or predict the evolution of SST. In the Hasselmann model, we predict SST as $T = \overline{T} + e^{\mu(t-t_0)}T'(t_0)$, which is the sum of climatology mean and the damped initial signal. In the modified Hasselmann model, the SST can be predicted as $T = \overline{T} + T_{trend} + e^{\mu(t-t_0)}T'(t_0)$, which is the sum of climatological mean, damped initial signal plus the trend. We then compare the evolution of SST into 1 year and 10 years later in both models (Fig. 4.5). For short prediction lead times (1-year), both models show similar skill (Fig. 4.5a), with correlation coefficients between predictions and observation of 0.83 and 0.87, respectively. But for longer prediction lead times (10 years), the prediction using the modified model captures the trend (Fig. 4.5b). As a result, the SST 10-year later in the modified Hasselmann model is better correlated with the observations than the classical Hasselmann model.
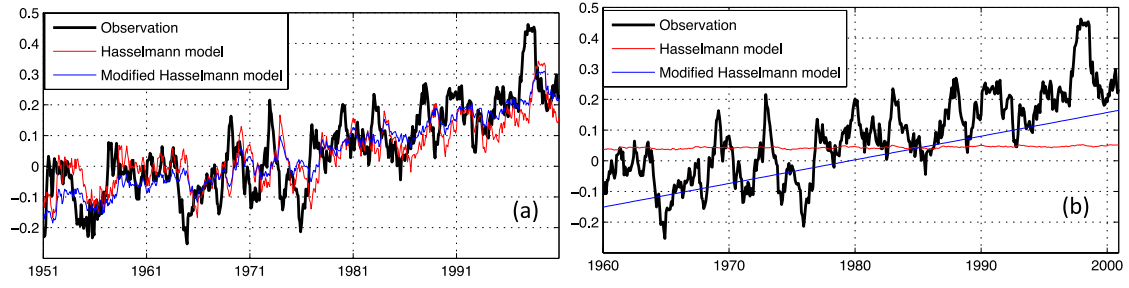
Figure 4.5. The (a) 1-year and (b) 10-year diagnostic predictions of global mean SST (seasonal cycle removed) using the Hasselmann model (red lines) and the modified Hasselmann model (blue lines). Black lines denote observational data.

Therefore, the modified Hasselmann model can be used to predict future SST and evaluate the change in damping when the WES feedback is turned off. Following the design of the decadal prediction experiment using CAM3, 49 hindcasts for 10-year prediction are initialized from 1951 to 1999 respectively in the modified Hasselmann model. However, unlike the diagnostic predictions of SST (Fig. 4.5), all the parameters used in these predictions, such as the climatology mean, seasonal cycle, trend and damping coefficients, are computed using only the information for the 10 years prior to initial time. Hence, we can compare the predictions using the modified Hasselmann model to those obtained using CAM3. Moreover, the modified Hasselmann model can be used as a diagnostic tool to evaluate the damping term of the predictions in the CAM3, and provide a quantitative measure of how the WES feedback affects decadal predictions.

IV.C. Prediction of SST

At first, the global mean SST is analyzed in section 1, to evaluate the skill of predictions from CAM3 and the modified Hasselmann model. The impact of WES feedback on the global mean SST predictions is also analyzed. As the trend is one of the important contributors to skill in decadal prediction, the predicted trends in the control run and the WESOFF sensitivity run are compared with observations in section 2. Then the prediction skills for regional patterns of SST are compared between the SOM run and the WESOFF run in section 3.

IV.C.1. Global mean SST

The model SST climatology is well simulated between 60°S and 60°N, with biases less than 0.5°C comparing to observation. But in the polar regions, where sea ice shows a strong seasonal cycle, the predicted annual SST shows warm biases. Since our focus is on the tropical and subtropical regions, we focus on the region between 60°S and 60°N, and refer to averages over this region as "the global mean".

Figure 4.6 shows the time series of observed and predicted global mean SST for decadal predictions. For the first year predictions of global mean SST, the results for the SOM run, the WESOFF run and the modified Hasselmann model are very close to the observations. All predictions capture certain large historical events, such as the 1982/83 El Nino, Mt. Pinatubo volcanic eruption in 1991 and the long-term warming trend. However, the predicted global mean SST in the CAM3 is not very sensitive to switching off the WES feedback. There are slight differences in the global mean SST between the

prediction with and without the WES feedback for the 1st year prediction (Fig. 4.6a). And the differences between the SOM run and the WESOFF run do not increase for longer prediction times (Fig. 4.6b to Fig. 4.6i).

Compared to the CAM3 predictions, the modified Hasselmann model gives similar predictions for the first year, but better prediction for longer lead times (Fig. 4.6). Based on the modified Hasselmann model, the damping from the initial signal captures the predictability of SST to certain extent. The predicted SST for the modified Hasselmann model range from 290.6K to 291K, which is similar to the range for observed SST. However, the predicted SSTs for both the CAM3 experiments exhibit a larger warming trend longer prediction lead times. Hence, the predicted SST ranges between 290.4 K and 291K for the 1st year prediction, and between 290K and 290.8K for the 9th year prediction. (This systematic discrepancy between the CAM3-SOM predictions and observation is analyzed further in Chapter V.)

In order to quantitatively evaluate the prediction skill, we use correlation coefficients and the root mean square error (RMSE) between predicted SST and observed SST as our metrics. We use the persistence forecast, where we assume that the initial SST remains constant for the duration of the forecast, as a baseline for measuring prediction skill. It turns out that the CAM3 runs and the modified Hasselmann model have better prediction skill than persistence. But the prediction skill measured by the correlation coefficients is not sensitive to switching off the WES feedback, as the SOM run and WESOFF run show similar results (Fig.4.7a). Moreover, the predictions in both numerical model and the modified Hasselmann model show similar prediction skill as

measured by correlation coefficients (Fig. 4.7a). However, the CAM3 predictions beat the modified Hasselmann model for lead times longer than 7 years.
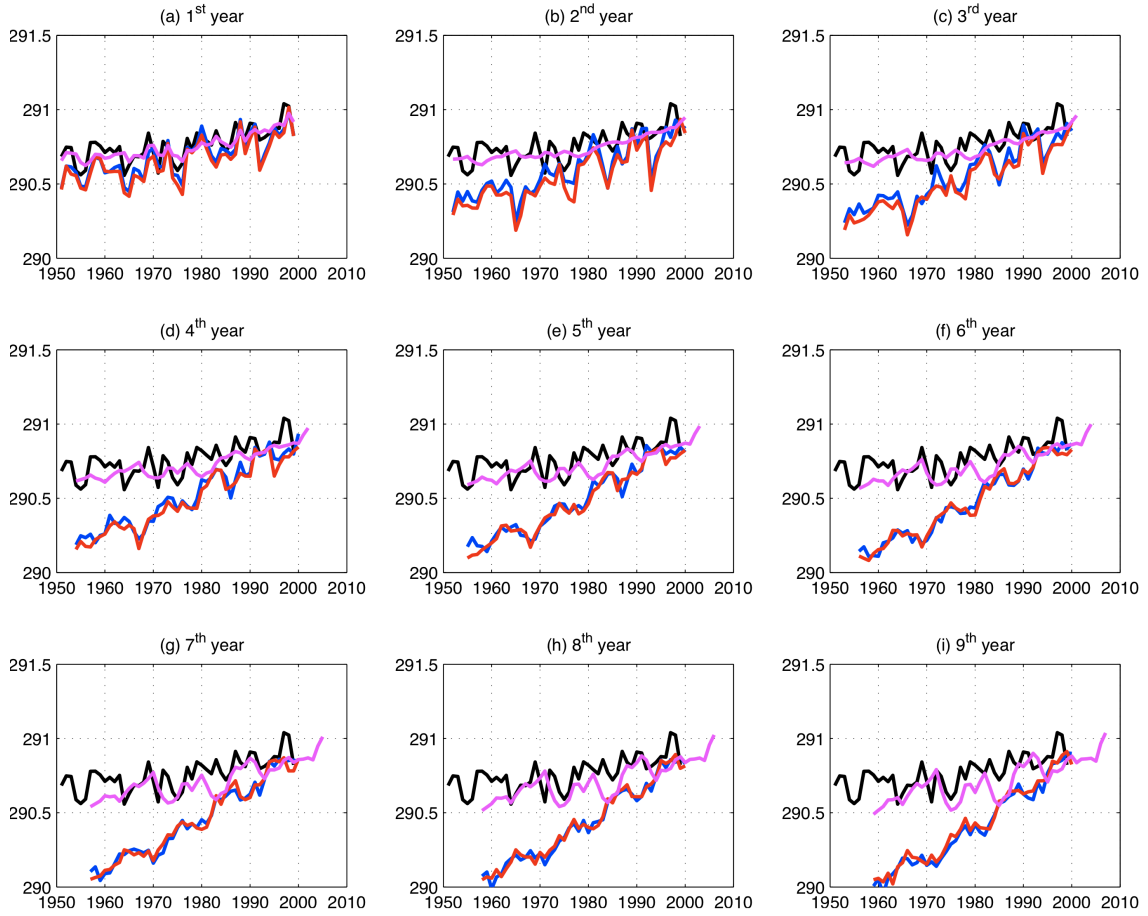
Figure 4.6. Observed and predicted global mean SST for lead times of 1 year to 9 years respectively in figure (a) to (i), for observations (black), the SOM run (blue), the WESOFF run (red), and the modified Hasselmann model (purple).
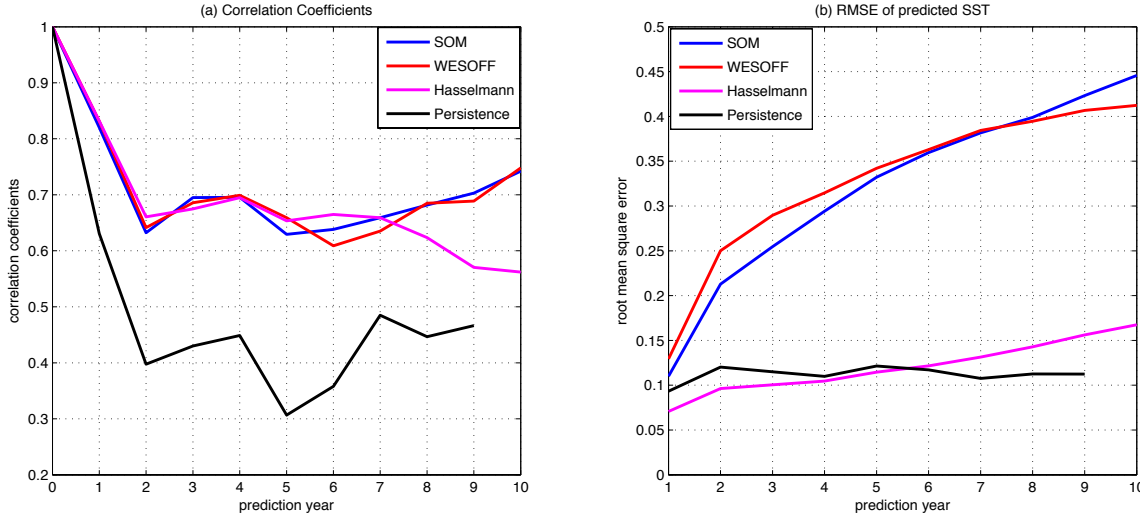
Figure 4.7. The prediction skill of (a) correlation coefficients and (b) RMSE for the first year prediction to 10th year prediction, for persistence (black), SOM run (blue), WESOFF run (red) and the modified Hasselmann model (purple).

As measured by the RMSE metric, the modified Hasselmann model shows better prediction skill than the CAM3 runs. The RMSE in the modified Hasselmann model is less than 0.1°C, while the RMSE in the CAM3 reaches to 0.45°C (Fig. 4.7b). The RMSE is much smaller for the modified Hasselmann model because its predictions exhibits trends similar to that in the observation (Fig. 4.6). However, the RMSE for numerical model's predictions increase from 0.15°C to 0.45°C, which is related to the overestimated trend in the CAM3 runs (Fig. 4.6). This overestimated trend is related to the Q-flux specification in the slab ocean, and will be discussed in Chapter V. Furthermore, there are small differences between RMSE prediction skill for the SOM run and the WESOFF run (Fig. 4.7b), with slightly higher RMSE for the predicted SST

in WESOFF run at short lead times and lower RMSE for the longer lead times. The prediction skills in terms of correlation coefficients and RMSE indicate that the predictions of global mean SSTs in the CAM3 are not very sensitive to switching off the WES feedback.

IV.C.2. Spatial structure of the trend

Thus far, we have considered globally-averaged metrics for evaluating prediction skill. Now we consider the spatial structure of the predictions, focusing on the SST trend, which can play a critical role in decadal prediction. We consider the following question: How well does the numerical model predict the SST trend, and to what extent does the WES feedback affect it? First, the SST trend in observation from 1951 to 2000 is computed (Fig. 4.8). For the last 50 year in the 20th century, a overall warming trend for SST is seen over the global ocean. Enhanced equatorial warming pattern occurs over Pacific and Atlantic (Liu et al. 2005; Xie et al. 2010). However, a cooling trend occurs over the north Pacific and north Atlantic, which may be related to dynamical effects from changes in the ocean circulation (Xie et al. 2010).

Compared to the observed SST trend, both the SOM run and the WESOFF run predict realistic SST trend for the 1st year prediction (Fig. 4.8b and Fig. 4.8c). The SST trend of 10th year prediction in the SOM run (Fig. 4.8d) and in the WESOFF run (Fig. 4.8e) shows similar patter as observation, but with much stronger warming trend. But over the tropical Pacific, the 1st year prediction of SST in both runs exhibits a weaker

warming trend than the observation. The reason for this could be the lack of ocean dynamics in the SOM.
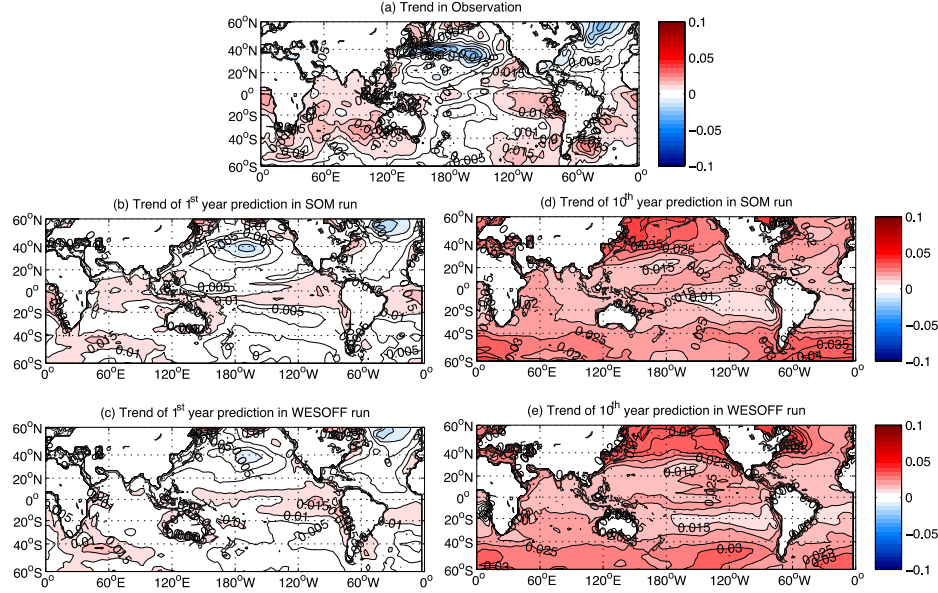
Figure 4.8. (a) Observed SST trend from 1951 to 2000. SST trend of (b) 1st year prediction and (d) 10th year prediction in the SOM run, and SST trend of (c) 1st year prediction and (e) 10th year prediction in the WESOFF run. Contour interval is 0.005°C per year.

Considering the sensitivity to the WES feedback, the WESOFF run has a larger SST warming trend in the 1st year prediction than the SOM run (Fig. 4.9a). Similar to the 1st year prediction, the 5th and 10th year predictions in the WESOFF run also show larger warming trends than the SOM run (Fig. 4.9b and 4.9c). As the WES feedback is switched off, the signal over the eastern tropical Pacific cannot propagate westward

81

effectively. As a result, the excess heating caused by external forcing accumulates over

the eastern tropical Pacific in the WESOFF run, resulting in a warmer trend.
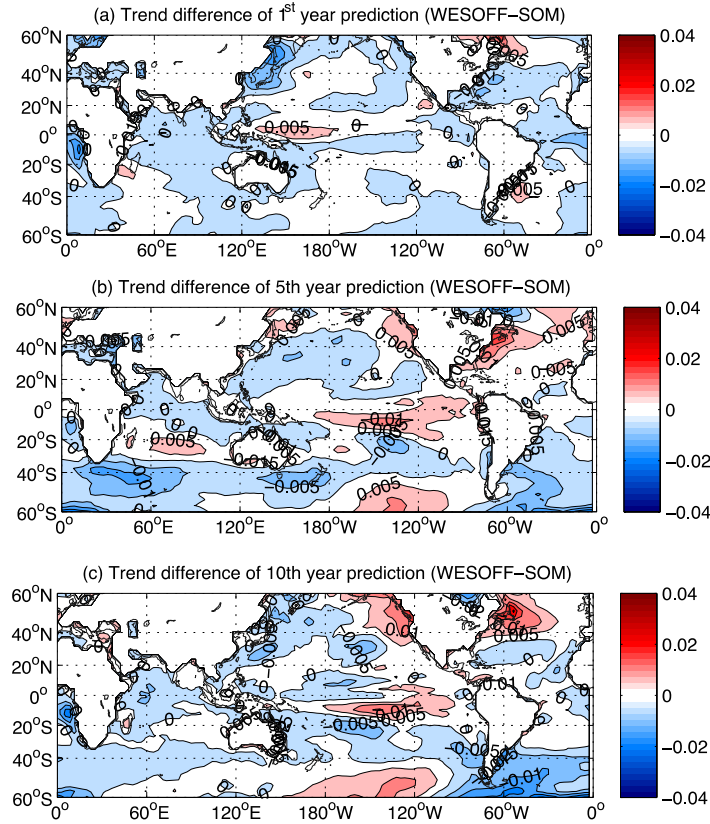
Figure 4.9. The difference in SST trend (WESOFF-SOM) for (a) the 1st year prediction,

(b) the 5th year prediction and (c) the 10th year prediction.

IV.C.3. Regional prediction skill

For the global mean SST, the predictions do not show large differences between the

SOM run and the WESOFF run (Fig. 4.7). The regional SST trend pattern predicted in

the two experiments shows some differences, especially over the tropical Pacific. Hence, the spatial patterns of prediction skill are analyzed in this section. The 1st year predictions show significant prediction skill over the whole globe in both runs, and do not show large regional differences between the SOM run and the WESOFF run (Figure not shown). However, for longer lead times, the predictions start to show some differences between the SOM run and the WESOFF run. Figure 4.10 shows the correlation coefficients between observation and the 5th year and 10th year prediction in the SOM and the WESOFF run.
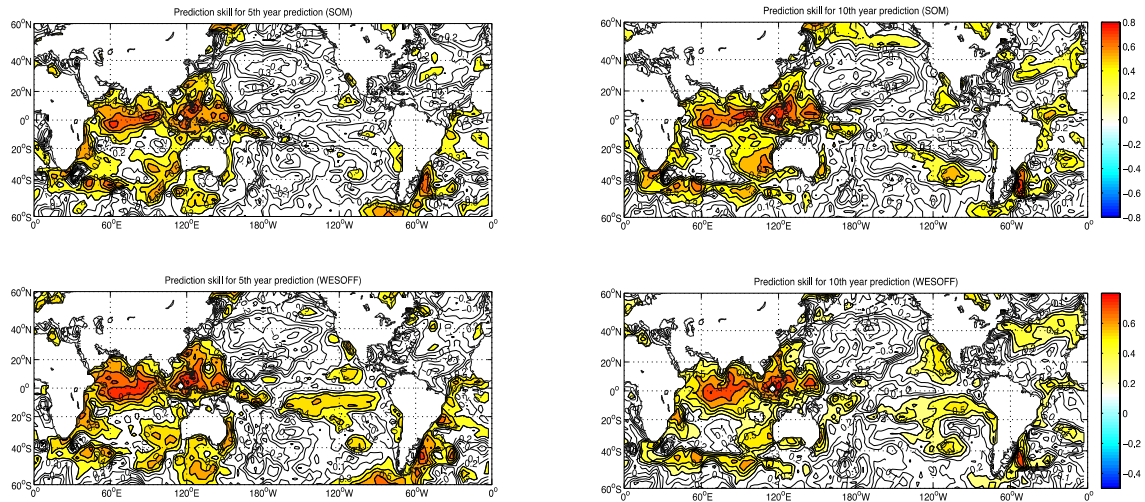
Figure 4.10. The correlation coefficients between observations and simulations for the 5th year prediction (left column) and the 10th year prediction (right column). The first row is for the SOM run and the second row is for the WESOFF run. Color shading indicates statistically significant correlations.

For the 5th year prediction, the global patterns of correlation coefficients are broadly similar between the SOM run and the WESOFF run. Predictions for both runs show significant skill over the western Pacific warm pool and the Indian Ocean (Fig. 4.10a and 4.10c). However, there are some differences over the eastern tropical Pacific. The WESOFF run shows significant prediction skill over eastern tropical Pacific (Fig. 4.10c), while the SOM run does not have significant prediction skill (Fig. 4.10a). The 10th year prediction of SST shows similar spatial pattern of significant prediction skill as that for the 5th year prediction (Fig. 4.10). Over the eastern tropical Pacific, the WESOFF run still exhibits better skill than the SOM run (Fig. 10d). This indicates that the SST variability over the eastern tropical Pacific is more sensitive to the WES feedback
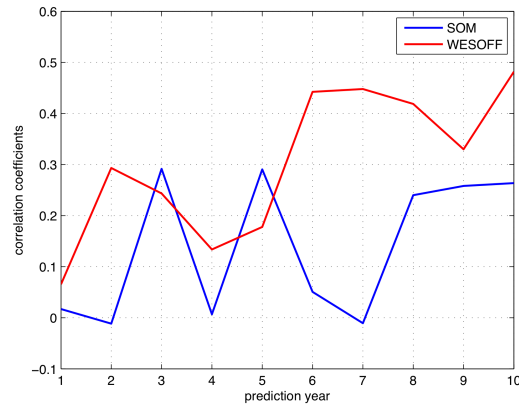
Figure 4.11. The correlation coefficient between the predicted and observed surface heat flux averaged over the eastern tropical Pacific for the SOM run (blue) and the WESOFF run (red).

In order to understand why the WESOFF run has better prediction skill over the eastern tropical Pacific, the latent and sensible heat flux in both runs are compared with the observations. Figure 4.11 shows the correlation coefficients between the simulated and observed surface heat flux averaged over the eastern tropical Pacific. When the WES feedback is switched off, the predicted latent and sensible heat flux exhibit stronger correlations with the observed values, especially at longer lead times (Fig. 4.11). This can help explain why the SST variation in the WESOFF run is better predicted than that in the SOM run. Further discussion of improved predictability over the tropical Pacific in the WESOFF run will be presented in Section D of this chapter.

The other metric for evaluating the predictions is the root-mean-square error (RMSE), which measures the magnitude of the deviation of the predictions from observations. There is fairly large RMSE over the tropical Pacific and the tropical Atlantic at all lead times, where ocean dynamics plays an important role in modulating the SST (not shown). But for longer lead times, the RMSE increases dramatically over the north Pacific and the north Atlantic, with maximum magnitude increasing to 2°C. This is perhaps an indication that over north Pacific and north Atlantic, where weather noise is very strong, the prediction skill is quite limited for longer prediction lead times.
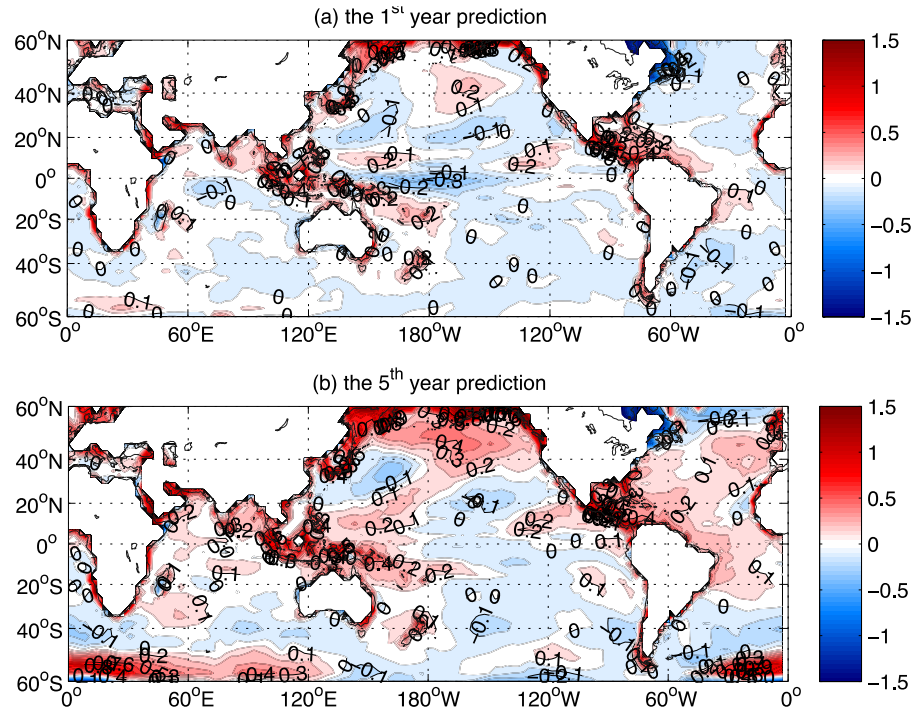
Figure 4.12. The SST RMSE difference (WESOFF – SOM) for (a) the 1st year prediction and (b) the 5th year prediction. Units: K

The difference in RMSE between the SOM run and the WESOFF run (WESOFF – SOM) is shown for the 1st year and 5th year prediction in Figure 4.12. The RMSE difference for the 10th year prediction shows a similar pattern as that in the 5th year, but with stronger magnitude (not shown). The differences between the WESOFF run and the SOM run are of the order of 0.25°C. Over the eastern tropical Pacific, where the prediction skill of correlation coefficients showed a large difference between the two runs, the differences in RMSE are small at all prediction lead times, with magnitude around 0.1°C. But over the North Pacific and the tropical Atlantic, the prediction in the WESOFF run shows increased RMSE, as prediction lead time increases. The increased

RMSE over the North Pacific in the WESOFF run may be related to the oceanic heat transport or in other word, the Q-flux, prescribed in the slab ocean model. Over the tropical Atlantic, the climatology SST is about 0.3C colder than observation in the SOM run, and about 0.6C colder than observation in the WESOFF run (Figure not shown). This indicates there is systematic error over the tropical Atlantic, which results in large RMSE for both the SOM run and the WESOFF run.

IV.D. Signal VS noise

Climate variability can be decomposed into two parts: the signal, which is predictable, and the noise, which is unpredictable. In decadal prediction, the skill of the numerical model is closely related to the signal portion of climate variability. The statistics of signal and noise are further investigated in this section, in order to understand the influence of the WES feedback on decadal predictions.

IV.D.1. Ensemble methods

A variable X can be separated into the mean, the internally generated predictable component, and the short timescale unpredictable 'noise' component (Boer and Lambert, 2008). The associated variances then have following relationship $\sigma^2 = \sigma_s^2 + \sigma_n^2$, here σ^2 represents the total variance, σ_s^2 for the variance of the predictable 'signal' and σ_s^2 for the variance of the unpredictable 'noise'. In numerical model simulations, one experiment can have several ensemble members with perturbed initial condition. Each ensemble member is a simulation containing the predictable signal and a different

realization of the unpredictable noise. The ensemble average can eliminate the unpredictable 'noise', and retain the predictable 'signal'.

Although we only have a 3-member ensemble for the SOM run and the WESOFF run, a diagnostic of the signal percentage can be computed. By considering the ensemble run of the 1st year prediction, the total variance of the predicted SST can be calculated. Furthermore the variance of predictable signal is computed based on the ensemble average of the 1st year prediction. Then the signal percentage can be evaluated as the ratio of the variance of signal to the total variance, which is also called the potential predictability variance function (Boer and Lambert, 2008):

$$Signal\ fraction = \sigma_s^2 \Big/ \sigma^2$$

Figure 4.13 shows the signal fraction for the 1st year prediction in the SOM run and the WESOFF run. Over the tropics, especially over the tropical Pacific, there is large signal fraction, which indicates strong potential predictability (Fig. 4.13a). While in the mid-latitudes, due to the presence of stronger weather noise, the potential predictability is pretty low. Moreover, comparing to the signal percentage in the SOM run, the WESOFF run shows similar spatial pattern of signal fraction over most of the tropical Pacific (Fig. 4.13b). However, the region with signal fraction exceeding 0.7 is much wider over the tropical Pacific in the WESOFF run (Fig. 4.13b). The signal fraction for the 5th year and 10th year prediction also shows similar patterns for the two runs (not shown).
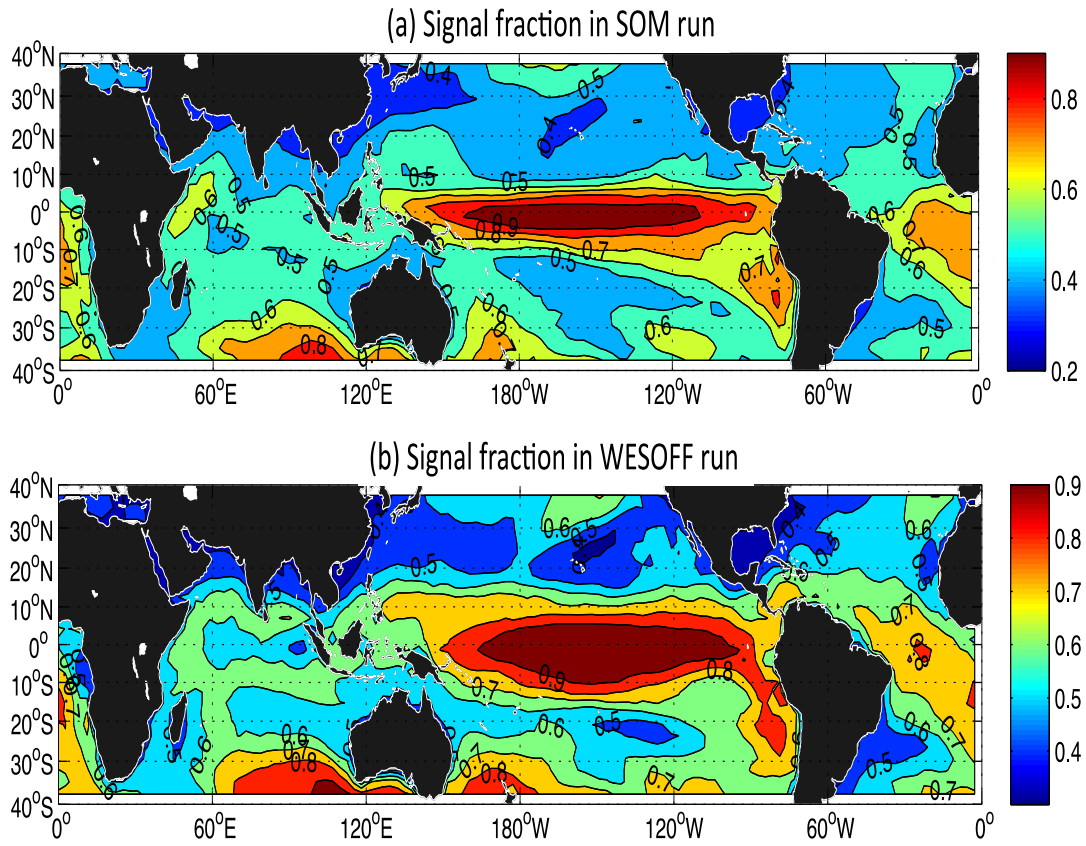
Figure 4.13. Signal fraction for the 1st year prediction in (a) the SOM run and (b) the WESOFF run. Contour interval is 0.1.

Although there are considerable similarities in spatial patterns, there are also notable differences in the signal fraction between the WESOFF run and the SOM run (Fig. 4.14). The signal fraction in the WESOFF run is generally larger than that in the SOM run, indicating increased potential predictability in the WESOFF run. The largest differences in signal fraction occur over the tropical Pacific. For the 1st year prediction, the signal in the WESOFF run is about 30% larger than that in the SOM run over

tropical Pacific (Fig. 4.14a). As longer prediction times, the signal percentage in the WESOFF run is up to 50% larger for the 5th year prediction (Fig. 4.14b) and 40% larger for the 10th prediction (Fig. 4.14c). This indicates that switching off the WES feedback results in an increase in the signal fraction over tropics becomes larger, which can lead to improved predictability.
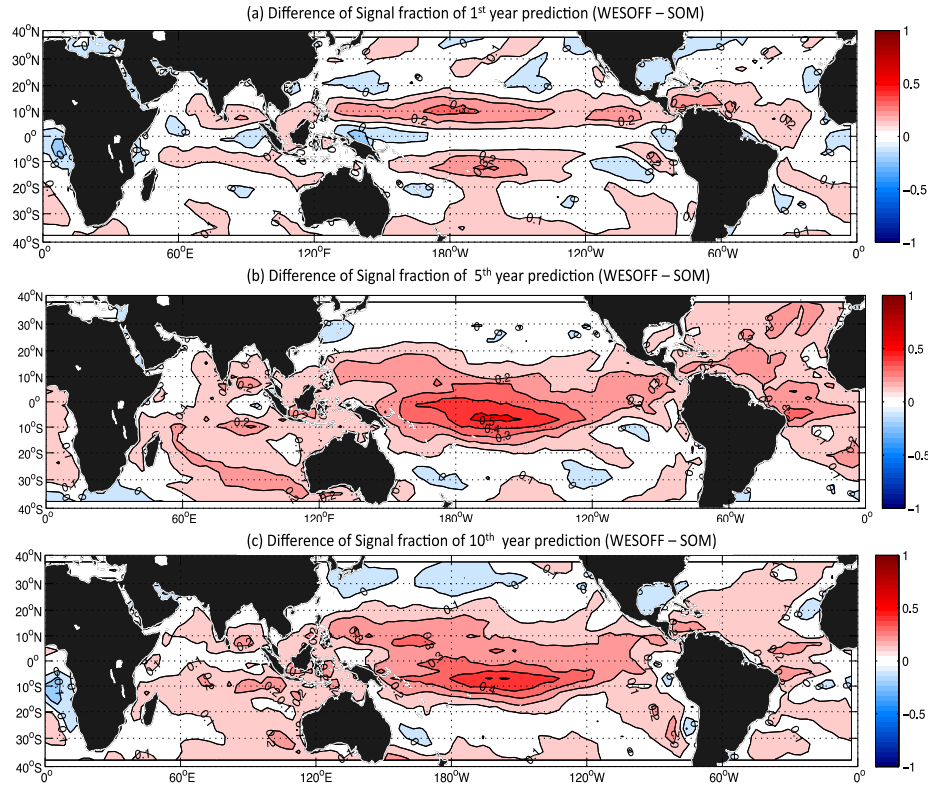
Figure 4.14. The difference of signal fraction (WESOFF – SOM) for (a) the 1st year prediction, (b) the 5th year prediction and (c) the 10th year prediction. Contour interval is 0.1.

IV.D.2. Modified Hasselmann model

In the modified Hasselmann model, the predictability of SST arises primarily from the damping term, which is related to the surface heat flux loss. The damping coefficients for the SOM run and the WESOFF run can be computed from the lag-1 autocorrelation coefficients. So for the 49 hindcasts, we compute the correlation between the initial SST and the predicted SST one month later, after removing the annual cycle and the linear trend (Fig. 4.15).

The damping coefficients over the tropics are small, especially over the eastern tropical Pacific (Fig. 4.15). Over the southern ocean (40°S-60°N), there is no ocean dynamics in the slab ocean model. Hence, the damping of the predicted SST in slab ocean model is weaker than that in observation (Fig. 4.15a). The damping over the ITCZ is much stronger, with damping coefficients values of around 0.3. Compared to the SOM run, there are similar spatial patterns of damping coefficients in the WESOFF run (Fig. 4.15b), but the magnitude of the damping is smaller. The fractional difference between the WESOFF run and the SOM run, (WESOFF − SOM)/SOM, is about -0.3 over the tropical Pacific (Fig. 4.15c), indicating weaker damping in the WESOFF run. Hence, the signal persists longer in the WESOFF run, which is consistent with the increase in signal fraction (Fig. 4.14).
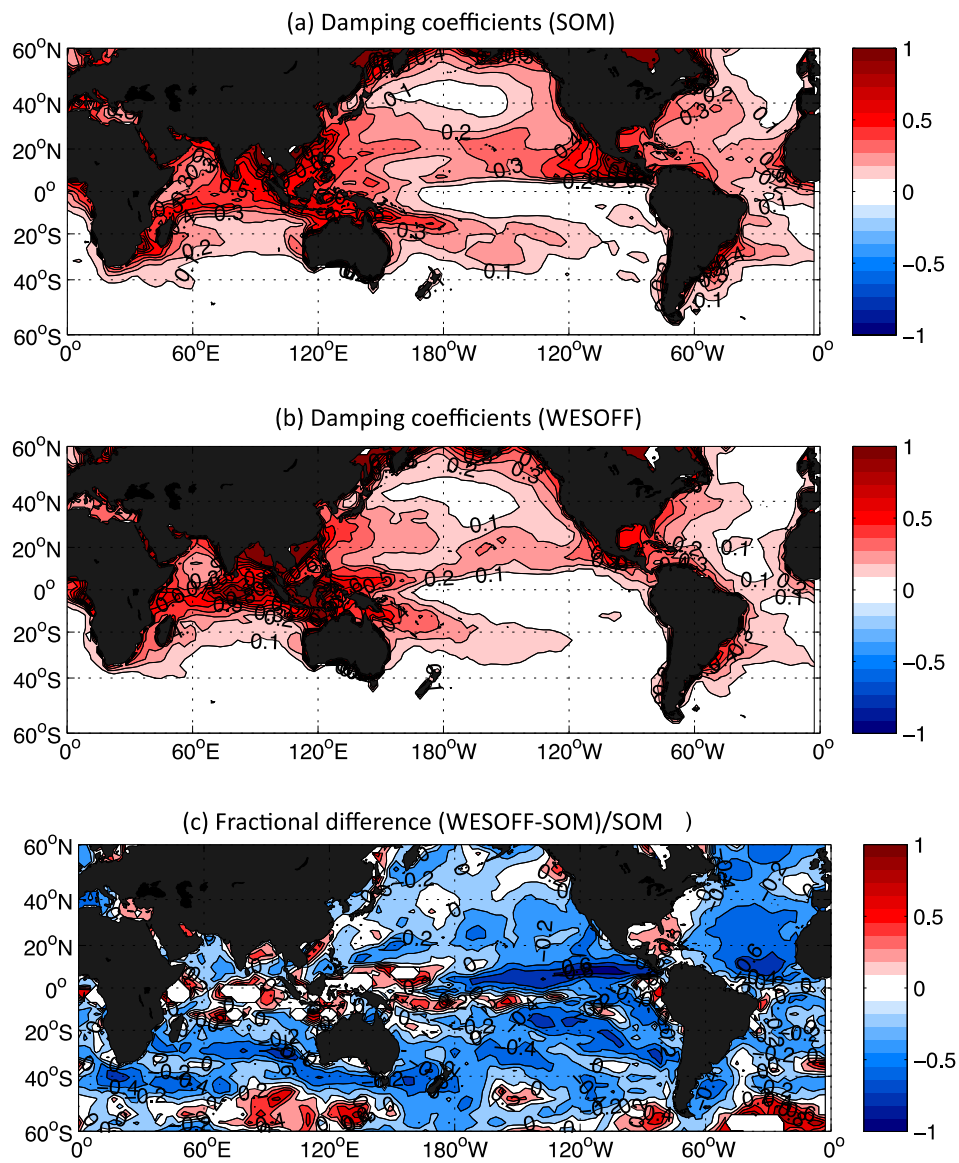
Figure 4.15. The damping coefficients for (a) the SOM run and (b) the WESOFF run, and the fractional difference of the damping coefficients (WESOFF − SOM)/SOM.

IV.E. Conclusions

In this chapter, the influence of the WES feedback on decadal prediction is studied using the CAM3 coupled to slab ocean model. For decadal prediction, 49 hindcasts from 1951 to 1999 are initialized with observed SST and integrated using projected future 10-year external forcings (the SOM run). Additionally, we carried out an additional set of hindcasts, but using a version of the CAM3 where the climatological annual cycle of frictional velocity was prescribed, thus eliminating the WES feedback (the WESOFF run). Apart from the numerical model predictions, a statistical model, the modified Hasselmann model, was also used to predict the evolution of SST, as well as to compute diagnostics related to the damping coefficient.

For the prediction of global mean SST, the numerical model and the statistical model provide predictions close to observations for short lead times (i.e., 1 year). For longer prediction times, the modified Hasselmann model remains close to observations, but the numerical model tends to have a cold SST bias in the early decades and therefore predict a larger warming trend. Hence, the prediction skills as measured by correlation coefficients are similar between the numerical and statistical models, but the RMSE in the numerical model predictions are considerably larger. Furthermore, the difference in prediction skill between the SOM run and the WESOFF run is quite small for the global mean SST, indicating that is not sensitive to switching off the WES feedback.

The SOM run and the WESOFF run do exhibit regional differences in the spatial patterns of prediction skill.. Both runs show significant prediction skill over the western Pacific warm pool and Indian Ocean. However, in the SOM run, there is no significant

prediction skill over the eastern tropical Pacific after 5 years. When the WES feedback is turned off in the WESOFF run, there is still significant prediction skill over the eastern tropical Pacific. Further investigation of averaged fluxes over the tropical Pacific region shows that the latent and sensible heat fluxes are better simulated in the WESOFF run. It suggests that when turning off the WES feedback, the damping related to heat fluxes becomes weaker. As a result, the influence of initial condition may last longer, which further causes better prediction skill in the WESOFF run.

By decomposing the prediction into the signal and noise components, the influence of WES feedback on decadal predictability is further investigated. The analysis of the prediction ensemble shows that the signal fraction in the WESOFF run is larger than that in the SOM run, especially over the tropical Pacific. This indicates that when the WES feedback is switched off, the signal from the initial condition lasts longer. To investigate this further, the damping coefficients in the SOM run and the WESOFF run are evaluated using the modified Hasselmann model. This analysis confirms that when the WES feedback is switched off, the damping coefficients indeed becomes smaller.

In summary, the WES feedback influences the prediction of SST through the latent and sensible heat fluxes, which act to damp SST anomalies. For the global mean SST, the switching off the WES feedback does not significantly alter the prediction skill. But over specific regions, such as the tropical Pacific, the switching off the WES feedback attenuates the damping of initial SST anomalies and increases the signal persistence, thus leading to improved prediction skill over those regions.

CHAPTER V

IMPORTANCE OF MEAN OCEAN HEAT TRANSPORT IN DECADAL

PREDICTION

V.A. Introduction

Ocean heat transport helps distribute the energy from the tropics to the polar regions, and is stronger than the atmospheric heat transport between 0° and 17°N (Trenberth and Carton, 2001). The ocean heat transport exhibits trends in observations, such as a weakened Meridional Overturning Circulation (MOC) leading to a decreased heat transport to the Antarctic (Kawano, 2011). A recent study by Yang et al. (2013) finds that initialization of the oceanic state over the North Atlantic, which has multidecadal variations, significantly improves the prediction skill of the multidecadal pattern of SST and air temperature in decadal predictions using the GFDL coupled model. In the slab ocean model, however, ocean heat transport is represented simply as a correction to the surface fluxes from CAM3. This flux correction term, usually referred as the Q-flux, parameterizes the missing ocean dynamics. In this chapter we address the following question: Can improvements in the computation of the prescribed Q-flux help improve the decadal prediction skill in the CAM3 coupled to slab ocean model? It is worth noting that in recent versions of CAM, i.e. CAM4 and CAM5, the formulation used for computing the Q-flux has been revised, to take into account some of issues relating to the sea-ice distribution (Kay et al. 2012 and Bitz et al. 2012).
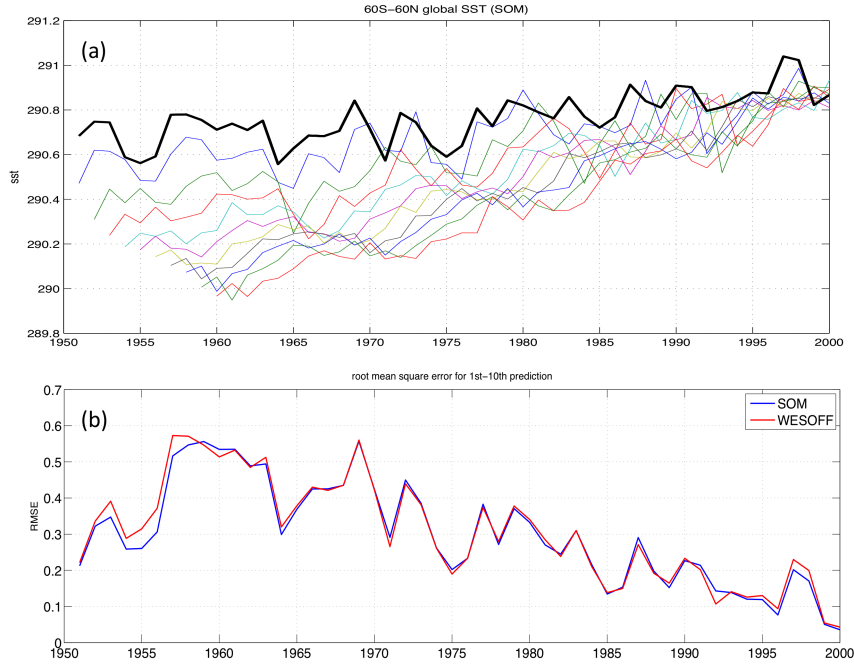
Figure 5.1. (a) Observed and predicted global mean SST in the SOM run and (b) the RMSE for predicted global mean SST for each year. The first blue line beneath the observed SST (black line) is the 1st year prediction of annual global mean SST. It shows a warming of 0.1C between the first decade and the last decade. The green line beneath the 1st year prediction is the 2nd year prediction, the red line beneath the 2nd year prediction is the 3rd year prediction, and so on. Units: K

In the decadal prediction experiments discussed in Chapter IV, the Q-flux is computed using the standard formulation, i.e., by carrying out an uncoupled CAM3 integration using the climatological SST boundary condition and using its surface fluxes. It was noted that the prediction of SST in the SOM run shows stronger-than-observed warming trend for longer prediction times. Figure 5.1a shows the time series of observed

and the predicted SST from 1st year to the 10th year. For the 10th year prediction, the last decade is about 0.7C warmer than the first decade, resulting in significant systematic error in the predictions.

It is interesting to note that the spreading of the 10-year prediction starting in the early years is wider than that in the later years. For example, the predictions of SST at 1960 range from 290.0 to 290.6 K, while the prediction of SST at 290.85 to 290.95K. The RMSE can be used to quantitatively describe the spreading. It can be seen that the RMSE decreases from 1960 to 2000, in both SOM run and WESOFF run (Fig. 5.1b). (Before 1960, the RMSE is smaller because of smaller prediction samples.)

One hypothesis for explaining the improved prediction during the last decades of the 20th century is that there are stronger external forcings in recent decades. As the external forcings change, the ocean heat transport is expected to change as well, which should be represented in the Q-flux of the slab ocean model. But for the SOM run, the Q-flux is set as a constant for all the 49 hindcasts. This fixed Q-flux may be unable to capture the decreasing trend in oceanic heat transport for the decadal prediction. So in this chapter, we investigate the role of mean ocean heat transport in decadal prediction by varying how we compute the Q-flux for the slab ocean model.

In section B, the Q-flux formulation for the slab ocean model is discussed, and then several numerical model experiments are carried out. At first, five sensitivity experiments are carried out to compare the influence of external forcing and Q-fluxes on decadal prediction. After testing our hypothesis regarding the role of Q-flux in decadal prediction, three additional sets of Q-flux patterns are generated and used in three

decadal prediction experiments respectively. Then the predictions of SST using the different Q-flux formulations are compared in Section C, and conclusions are drawn in Section D.

V.B. Numerical model setup

V.B.1. Q-flux in slab ocean model

The Q-flux term is required to compensate for the lack of ocean heat transport in the slab ocean model (e.g., Kiehl, 1996; Mahajan et al., 2009). At each ocean grid point, the following balance is assumed: $\rho CH \frac{\partial T}{\partial t} = F + Q$. Here, ρ is the density of sea water, C is the specific heat capacity, H is the mixed layer depth, F is the net downward surface heat flux and Q is the Q-flux correction term representing the mean oceanic heat transport. When a critical climate feedback is turned off in the model, it is necessary to compute a new Q-flux to ensure an equilibrium state for the new experiment.

In order to generate the Q-flux for the SOM run, the CAM3 is forced with climatological SST and external forcings at the 1991 level for 50 years. This is an uncoupled atmosphere-only integration using the data ocean model (DOM) to prescribe the SST. Using the monthly climatology surface fluxes, such as the latent heat flux, the sensible heat flux, the net surface longwave radiation and the net surface shortwave radiation from this integration, as well as the monthly climatology of SST, the monthly mean Q-flux can be calculated using the following equation:.

$$Q^n = \rho CH \frac{T^{n+1} - T^n}{\Delta t} - F^n \tag{5.1}$$

Positive Q-flux values indicate the divergence of heat due to ocean dynamics, and vice versa for negative values. The annual mean Q-flux for the SOM run is shown in Figure 5.2. Over the tropics, especially over the tropical Pacific, there is positive Q-flux, taking heat out of the ocean, to represent the northward oceanic heat transport (Trenberth and Carton, 2001). Negative Q-flux values dominate the mid latitudes, which represents the heat transported by west boundary current from tropics to mid latitude, such as in the Kuroshio and Gulf Stream regions,. With this prescribed Q-flux, the influence of oceanic heat transport on the evolution of mixed-layer SST can be captured in the SOM model.
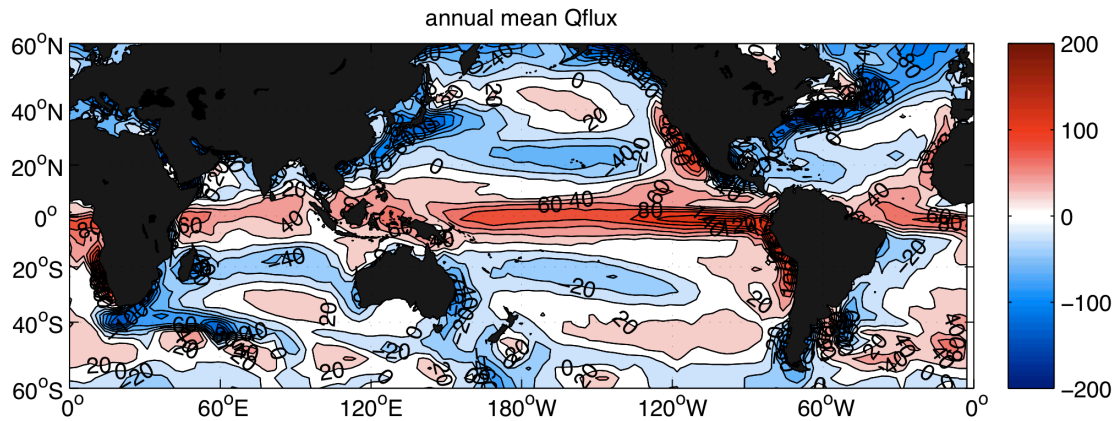
Figure 5.2. Annual mean Q-flux for the SOM run.

V.B.2. Sensitivity experiments

In order to investigate the impact of external forcing on the predictions, three additional sensitivity hindcast experiments are carried out for the 1951 initial condition with same Q-flux used in the SOM run. The initial condition is set to the observed SST at 1951, but different GHG forcings are prescribed (Fig. 5.3). The projected GHG forcings have two parts: a starting level and a projected trend. For the control 1951 hindcast in the SOM run, the GHG forcing is prescribed as the GHG level at 1951 plus 1X linear trend computed using previous ten years of data. For the first sensitivity hindcast experiment, we used the same starting GHG level at 1951, but changed the projected trend to zero (0X). For the second sensitivity experiment, we used a tripled (3X) projected trend. For the third sensitivity experiment, we changed the starting GHG level to 1991 GHG concentration, but kept the same projected trend as that in the SOM run (1X). By comparing the four hindcasts for 1951 initial condition, we can compare the influence of the mean and the trend of external GHG forcings on decadal prediction.

The predicted annual SSTs from 1951 to 1960 in the four experiments are shown in Figure 5.4. For the predictions with same starting GHG level but with different trends, the predicted SSTs in these experiments show similar cooling trend. The predicted SSTs decrease about 0.6K from 1951 to 1960. However, in the prediction with projected external forcing starting at 1991 GHG level, the decreasing trend is much weaker, leading to predictions that are much closer to observations. This indicates that prescribing GHG forcings at the 1991 GHG concentration level gives better prediction

even for the 1951 initial condition. Increasing the trend in the prescribed GHG forcings does not eliminate the unrealistic cooling trend in the predicted SST.
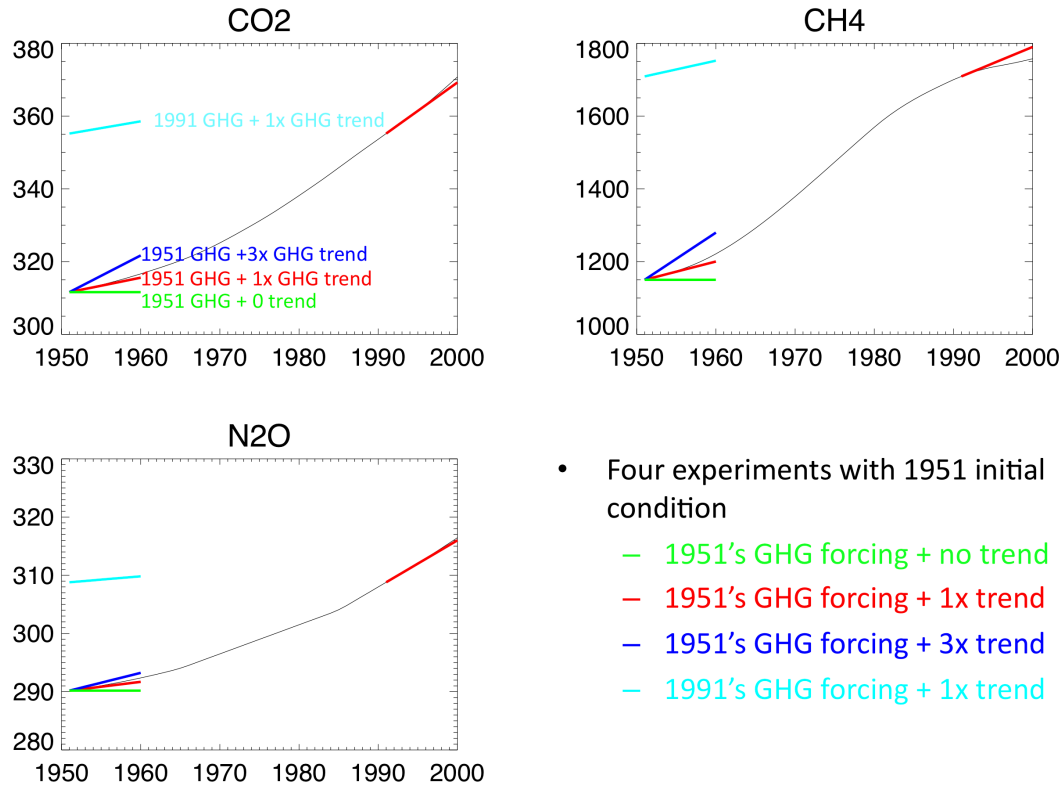
Figure 5.3. The GHG forcings. Black line is the observation. The red, blue and green lines are the prescribed GHG starting from 1951 GHG level, but with 1X time trend, 0X trend and 3X times trend respectively. The cyan lines are the prescribed GHG forcing starting from 1991 GHG level with 1X time trend.

How does the starting GHG level in the prescribed GHG forcings affect the decadal prediction? Note that the Q-flux used for the control 1951 hindcasts is the same as that in the SOM run, which is computed using the GHG concentration at the 1991 year. This suggests the GHG level used in the Q-flux computations affects the decadal prediction. Therefore, we carried out a 4th sensitivity hindcast experiment for 1951 by computing a new Q-flux using the 1951 GHG level. The only difference between the 4th experiment and the control 1951 hindcast in the SOM run is the Q-flux, which is generated with different GHG levels. With the new Q-flux, the predicted annual SST (Fig. 5.4) shows similar results as the one in the 3rd sensitivity experiment, which uses the control Q-flux but the 1991 GHG concentration levels. This demonstrates that the new Q-flux computed using the 1951 GHG concentration can improve the prediction by eliminating the systematic cold bias in the early years. The external forcing affects the Q-flux, and can affect the systematic errors in the prediction of SST. As the external forcings, especially the GHG forcings, show an increasing trend, the Q-flux used for the decadal predictions in the slab ocean model may need to vary to represent the change of ocean heat transport.
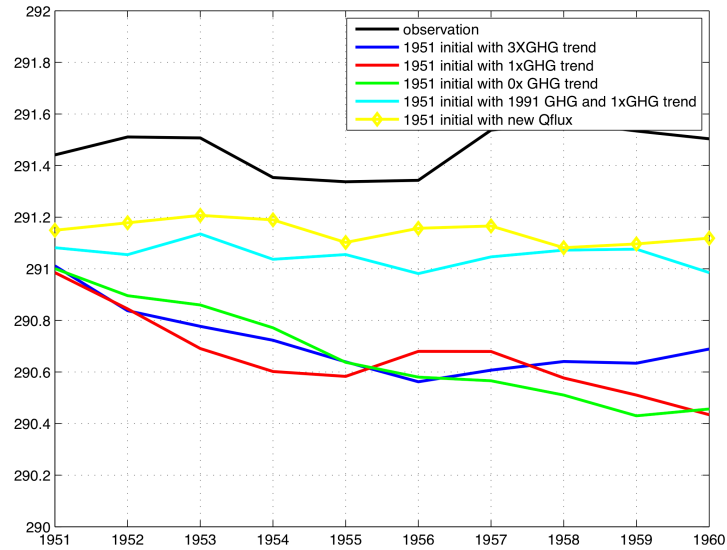
Figure 5.4. Observed and predicted SST for the 1951 hindcast from 1951 to 1960. Black line is for observation. All hindcasts are carried out with 1951 initial condition. The red, blue and green lines are for predicted SST in the 1951 hindcast with projected GHG forcings of 1951 GHG concentration plus 1X trend, 0X trend and 3X trend respectively. The cyan line is the predicted SST in the experiment with projected GHG forcings of 1991 GHG concentration plus 1X trend. The yellow line is the prediction with projected GHG forcings of 1951 GHG concentration plus 1X trend, but using the new Q-flux computed using the 1951 GHG forcing.

V.B.3. Q-flux experiments

The discussion in the previous section suggests that instead of using a *fixed* climatological Q-flux to represent oceanic heat transport in decadal predictions, which leads to systematic errors, it might be better to use an *adaptive* Q-flux that is more consistent with the initial conditions. In section, we evaluate three different Q-flux formulations that address this issue.

To compute the first set of Q-flux patterns (**Q-flux1**), a CAM3 integration forced with observed SST and external forcings from 1940 to 2000 is carried out. Using surface fluxes from this AMIP-style integration, the 10-year information prior to each initial year is used to compute the Q-flux for predictions starting at that initial condition, using equation (5.1). For example, the 1951 predictions use Q-flux computed using surface flux data from years 1941-1950. Thus, Q-flux1 uses a *fully adaptive,* time-varying approach based only on the preceding 10 years, instead of the climatological approach in the control run.

The second set of Q-flux (**Q-flux2**) uses a *partially adaptive* approach, where climatological SST is prescribed for computing the Q-flux, but the external GHG forcing is varied to be consistent with the initial condition for the prediction. To compute Q-flux2 for the 1951 predictions, we carry out a 30-year CAM3 integration with climatological SST, but with GHG forcing set at the 1951 level. The last 20 years of this integration are used to compute the Q-flux using equation (5.1). We repeat this for each of the 49 hindcasts, thus using 49 different Q-flux patterns for the hindcasts.

As discussed below, Q-flux2 appears to overcorrect for the systematic error in the forecasts. Therefore, we compute a third set of Q-fluxes (**Q-flux3**), which is simply the average of the Q-flux2 and the fixed Q-flux patterns used in the SOM run.

The dominant spatial mode of variability for the 49 Q-flux patterns in the Q-flux1 and the Q-flux2 datasets are captured by the leading EOF mode (Fig. 5.5a and 5.5c), which shows a similar spatial pattern as the fixed Q-flux in the SOM run (Fig. 5.3). Although the Q-flux1 and the Q-flux2 show similar spatial patterns, the PC1 for Q-flux1 shows much lower frequency variation (Fig. 5.5b). In contrast, the PC1 in Q-flux2 has stronger interannual variation (Fig. 5.5d). However, both Q-flux datasets indicate a decreasing trend in the Q-flux from 1951 to 1999 (Fig. 5.5b and 5.5d). This is consistent with a decrease in the oceanic heat transport, which may be related to increasing GHG forcings from 1951 to 2000.

We carried out three sets of decadal prediction experiments, using the same initial conditions and external forcings as the SOM run, but using the new Q-flux: the SOM-Qflux1 run, the SOM-Qflux2 run and the SOM-Qflux3 run. The predictions in the experiments with varied Q-fluxes are compared with the SOM run, which used a fixed Q-flux for all 49 hindcasts.
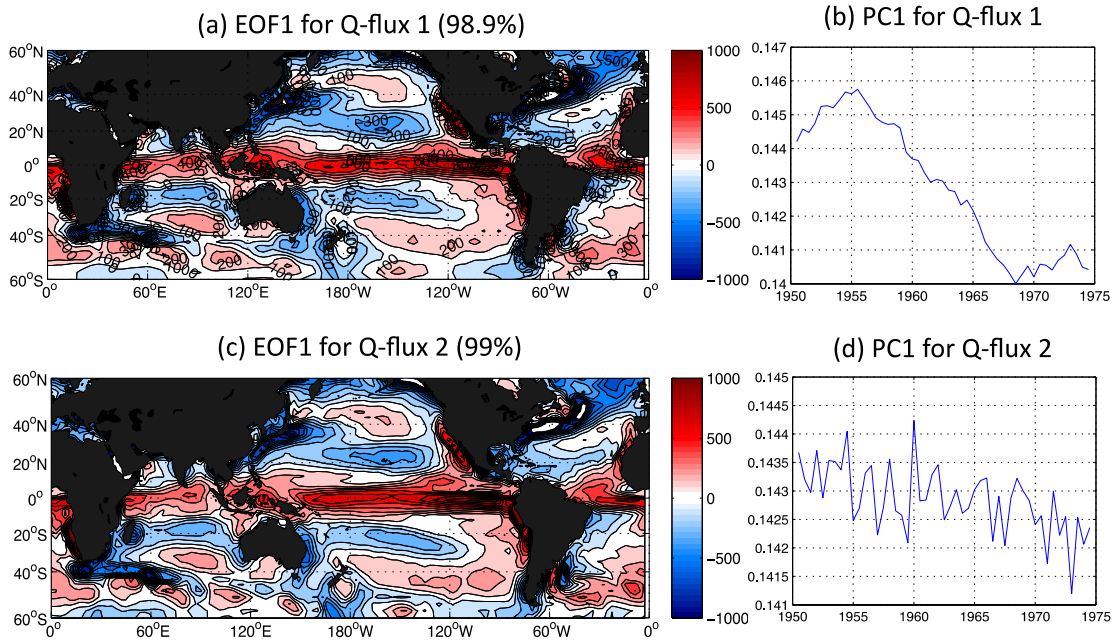
Figure 5.5. EOF analysis of 49 Q-fluxes in the Q-flux1 and the Q-flux2 datasets. (a) The leading EOF mode, and (b) the leading Principal Component (PC1) for the Q-flux1; (c) the leading EOF mode, and (d) the first PC for the Q-flux2.

V.C. Prediction of SST

The time series of predicted global mean SST in the four decadal prediction experiments with different Q-fluxes are shown in Fig. 5.6. For the first year, all predictions are close to the observations, with only slight differences during the early decades of the prediction time frame (Fig. 5.6a). However, the differences among the predictions with different Q-fluxes increase for longer prediction times. From the 1st year prediction to the 9th year prediction, the prediction with fixed Q-flux (the SOM run) becomes systematically colder than the observations, especially over the early decades.

In contrast, the predictions using Q-flux1 and the Q-flux2 become warmer than observations as prediction time goes longer. This suggests that the Q-flux1 and Q-flux2 formulations overcorrect for the cooling bias seen in SOM run. Since Q-flux2 performs slightly better than Q-flux1, we created a new set of Q-flux patterns, Q-flux3, by averaging the Q-flux2 and the fixed Q-flux from the SOM run. As we see in Figure 5.6, predictions using Q-flux3 are the closest to observations.

We use the correlation coefficient and RMSE metrics, as well as the mean, the standard deviation (STD) and the trend, to evaluate the quantitative skill associated with decadal predictions using the different Q-flux formulations (Fig. 5.7). Compared to persistence, SST predictions in the SOM run, the SOM-Qflux1 run and the SOM-Qflux3 run all show skill (Fig. 5.7a). However, SST predictions in the SOM-Qflux2 run fail to beat persistence, due to underestimated trend in the SOM-Qflux2 run (Fig. 5.7f). This is verified by repeating the correlation analysis using de-trended observations and de-trended predictions (Fig. 5.7c). The de-trended correlation coefficients between observation and prediction are lower and not significant at the 95% significance level for prediction times longer than 2 years. This demonstrates that the trend makes a large contribution to the prediction skill beyond two years.
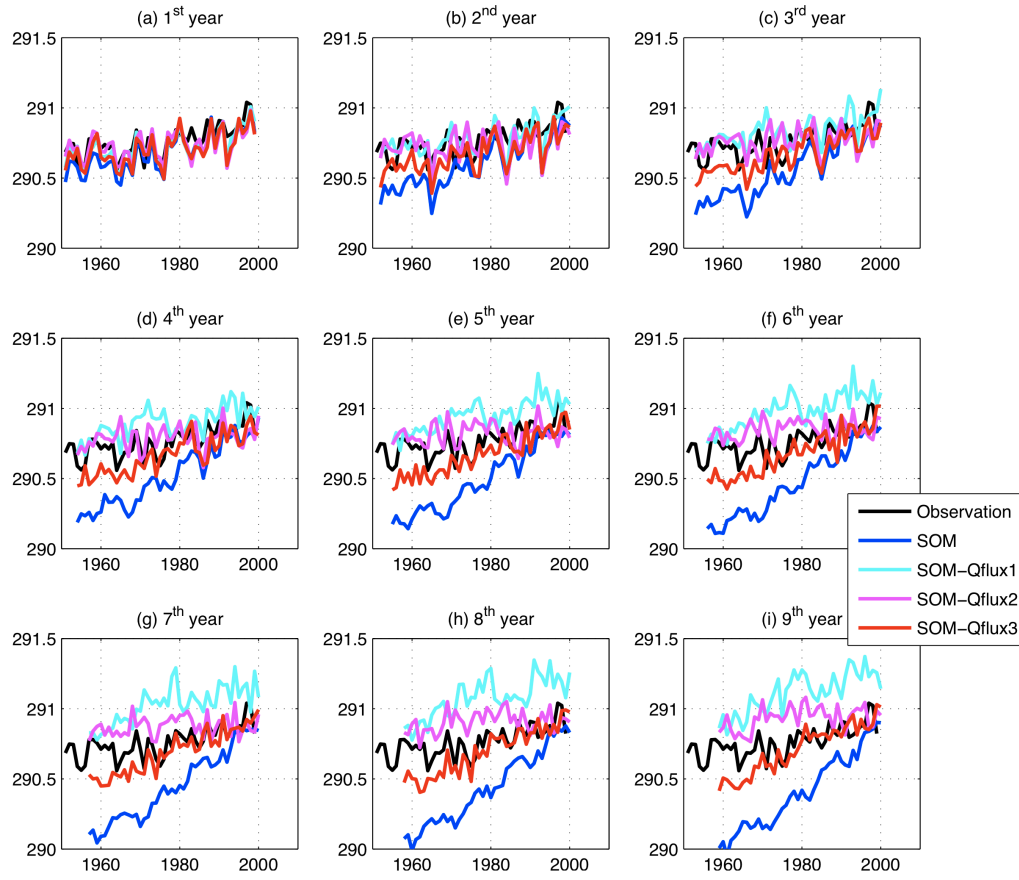
Figure 5.6. Observed and predicted SST for the 1st to the 9th year prediction for observations (black), SOM run (blue), SOM-Qflux1 (cyan), SOM-Qflux2 (magenta), and SOM-Qflux3 (red)

The magnitude of the deviation between predictions and observation is captured by the RMSE metric (Fig. 5.7b). The RMSE in the SOM run increases from 0.13C to 0.45C as the prediction time increases. This increase in RMSE is related to the increase of the systematic cold bias (Fig. 5.7d) and overestimated trend (Fig. 5.7f). The RMSE in the SOM-Qflux1 run also shows a steady increase of the RMSE. But unlike the SOM run,

this increasing RMSE in the SOM-Qflux1 run is due to an increase of the systematic warm bias (Fig. 5.7d).

However, the predictions using the SOM-Qflux2 run and the SOM-Qflux3 run exhibit a much smaller RMSE with maximum around 0.15K from the 1st year to the 10th year prediction (Fig. 5.7b). But the similarities in RMSE in the SOM-Qflux2 run and the SOM-Qflux3 run are due to different reasons. Compared to observations, the climatological mean of predicted SST exhibits a warm bias in the SOM-Qflux2 run, but a cold bias in the SOM-Qflux3 run (Fig. 5.7d). It is also worth noting that the standard deviation of predicted SST in the SOM-Qflux3 run is larger than in the observations, while the SOM-Qflux2 run has a smaller standard deviation (Fig. 5.7e). Furthermore, the trend is underestimated in the SOM-Qflux2 run, but overestimated in the SOM-Qflux3 run (Fig. 5.7f).

Considering all the metrics in Fig. 5.7, the SOM-Qflux3 provides the best overall performance for prediction of the global mean SST. It clearly shows better prediction skill than the SOM run for longer prediction times, and its prediction errors are also generally smaller than all the other Q-flux formulations. The comparisons among the 4 decadal prediction experiments with different Q-flux formulations indicate that the proper representation of Q-flux, which essentially parameterizes the mean ocean heat transport, is important for decadal prediction. Using an adaptive Q-flux that varies with the initial condition can significantly improve the skill of decadal prediction using the slab ocean model.
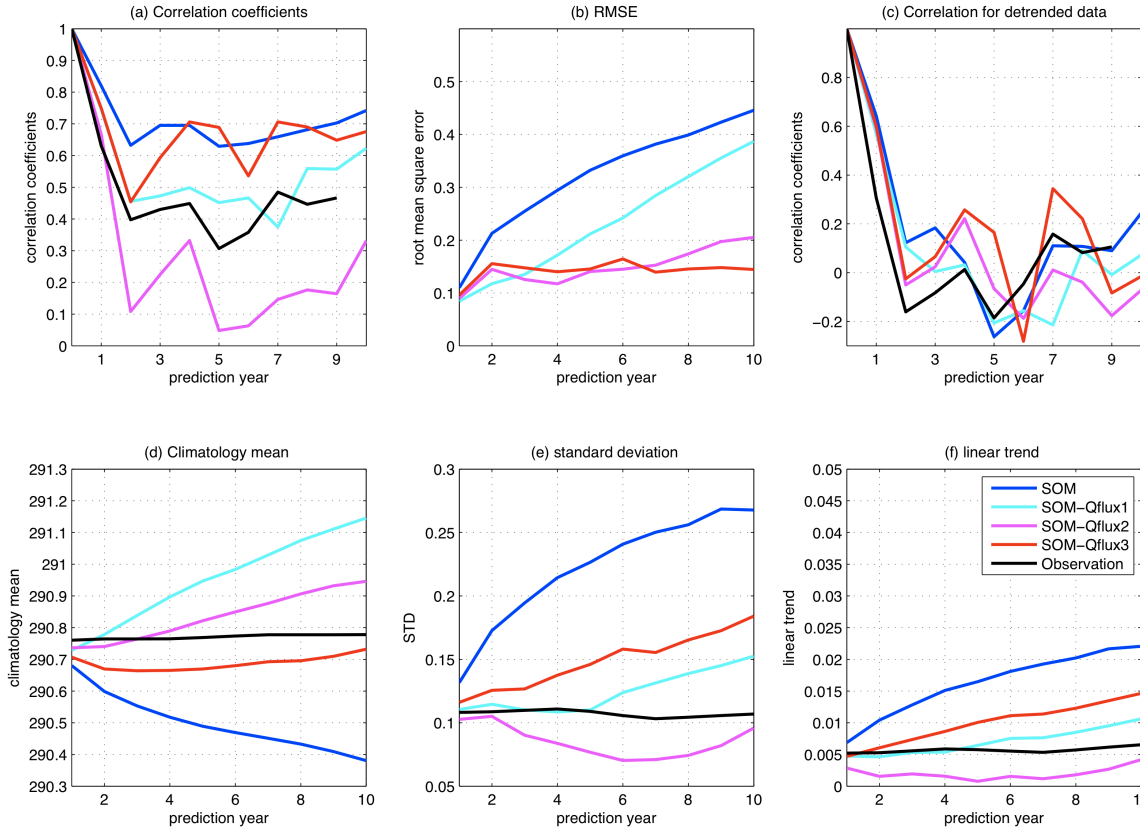
Figure 5.7. Prediction skill of (a) correlation coefficients and (b) RMSE for the 1st year to the 10th year prediction. (c) Correlation coefficients between detrended observed SST and detrended predictions. (d) The climatological mean, (e) the standard deviation and (f) the linear trend for observed and predicted SST. The black line shows the persistence and the indices for observation. The different runs are SOM run (blue), SOM-Qflux1 (cyan), SOM-Qflux2 (magenta), and SOM-Qflux3 (red).

Next we analyze the spatial patterns of prediction skill for different Q-flux formulations. Figure 5.8 shows the spatial pattern of skill as measured by correlation coefficients for the 5th year prediction. The prediction skills for the 1st year to the 10th year prediction display similar patterns with different significance levels (not shown). The prediction over the western Pacific warm pool in the SOM run shows significant prediction skill (Fig. 5.8a). However, the region of significant prediction skills over the western Pacific warm pool and Indian Ocean shrinks in the SOM-Qflux1 run (Fig. 5.8b), the SOM-Qflux2 run (Fig. 5.8c) and the SOM-Qflux3 run (Fig. 5.8d). The SOM-Qflux2 run barely shows significant prediction skill over the western Pacific warm pool, presumably due to the underestimated SST trend. The SOM-Qflux1 run (Fig. 5.8b) shows similar prediction skill over the western Pacific warm pool and Indian Ocean as that in the SOM-Qflux3 run. However, the SOM-Qflux3 shows improved prediction skill over the eastern tropical Pacific. Overall, the SOM-Qflux3 run demonstrates the best prediction skill in terms of correlation coefficients.

The RMSE for the 5th year prediction in all four decadal prediction experiments is shown in Figure 5.9. The RMSE for the 1st year prediction to the 10th year prediction (not shown) displays a similar spatial pattern as that for the 5th year prediction. For the 5th year prediction, the spatial patterns of RMSE in all 4 decadal predictions are similar. There is large RMSEs over the North Pacific and the equatorial Pacific, and small RMSE over the Indian Ocean, the tropical Atlantic and the southern Pacific (Fig. 5.9). The RMSE over the tropical Pacific are between 0.75°C and 1°C for all 4 decadal

predictions. However, over the north Pacific, the SOM run exhibits a larger RMSE than the other runs.

Next, we examine the RMSE differences between the SOM run and all the other runs (Fig. 5.10). The RMSE differences for all the decadal predictions with adaptive Q-flux have similar spatial patterns, with negative values dominating over positive values. The maximum reduction of RMSE occurs over the north Pacific,. However, there are some regions with increased RMSE, such as the circumpolar current region and the southern Pacific Ocean. The reduced RMSE in the SOM-Qflux3 run indicates that using adaptive Q-flux generally results in lower regional RMSE than using fixed Q-flux.

Figure 5.8. Correlation coefficients for the 5th year prediction in (a) the SOM run, (b) the SOM-Qflux1 run, (c) the SOM-Qflux2 run and (d) the SOM-Qflux3 run. Shading represents the 95% significance level.
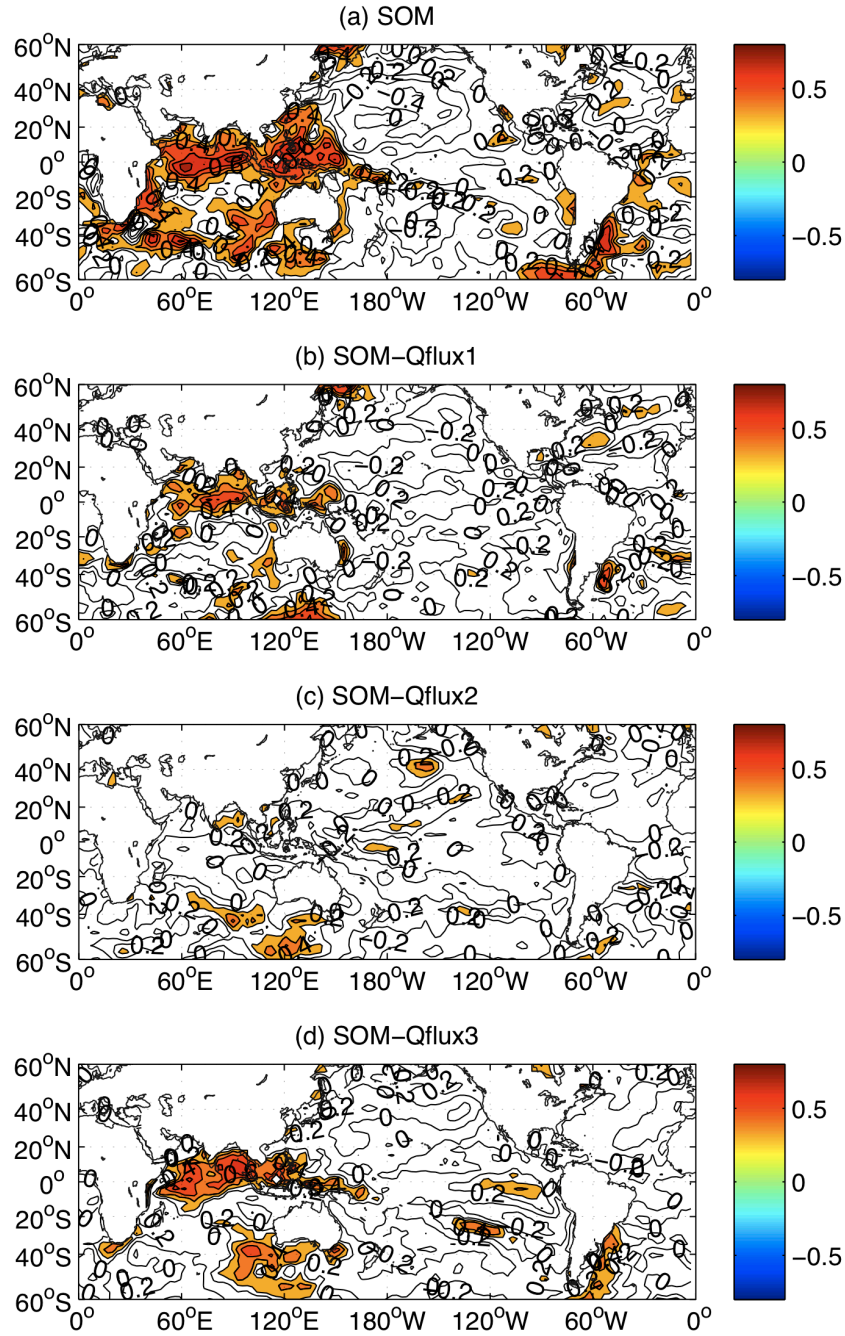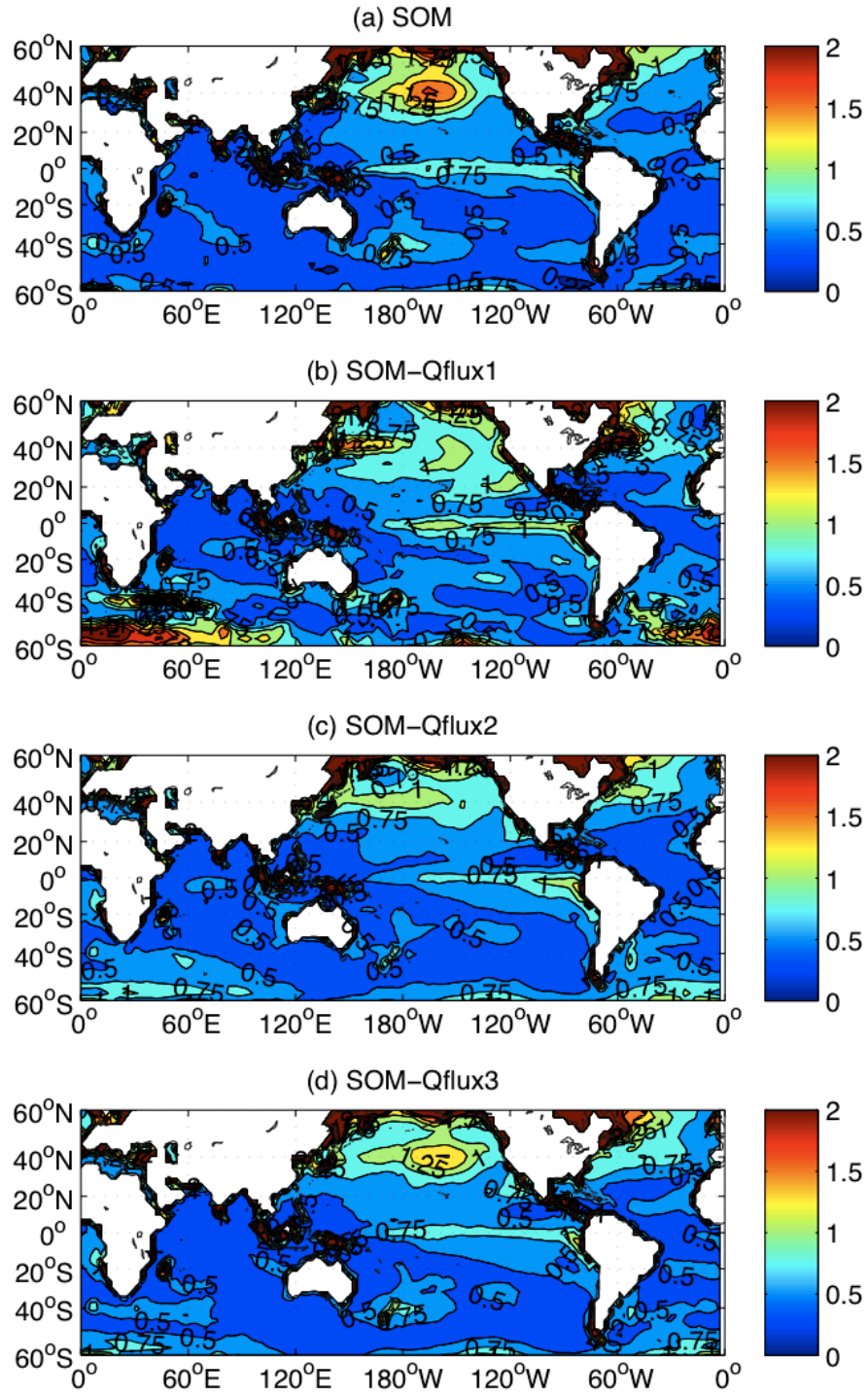
Figure 5.9. RMSE for the 5th year prediction in (a) the SOM run, (b) the SOM-Qflux1 run, (c) the SOM-Qflux2 run and (d) the SOM-Qflux3 run. Unit: °C
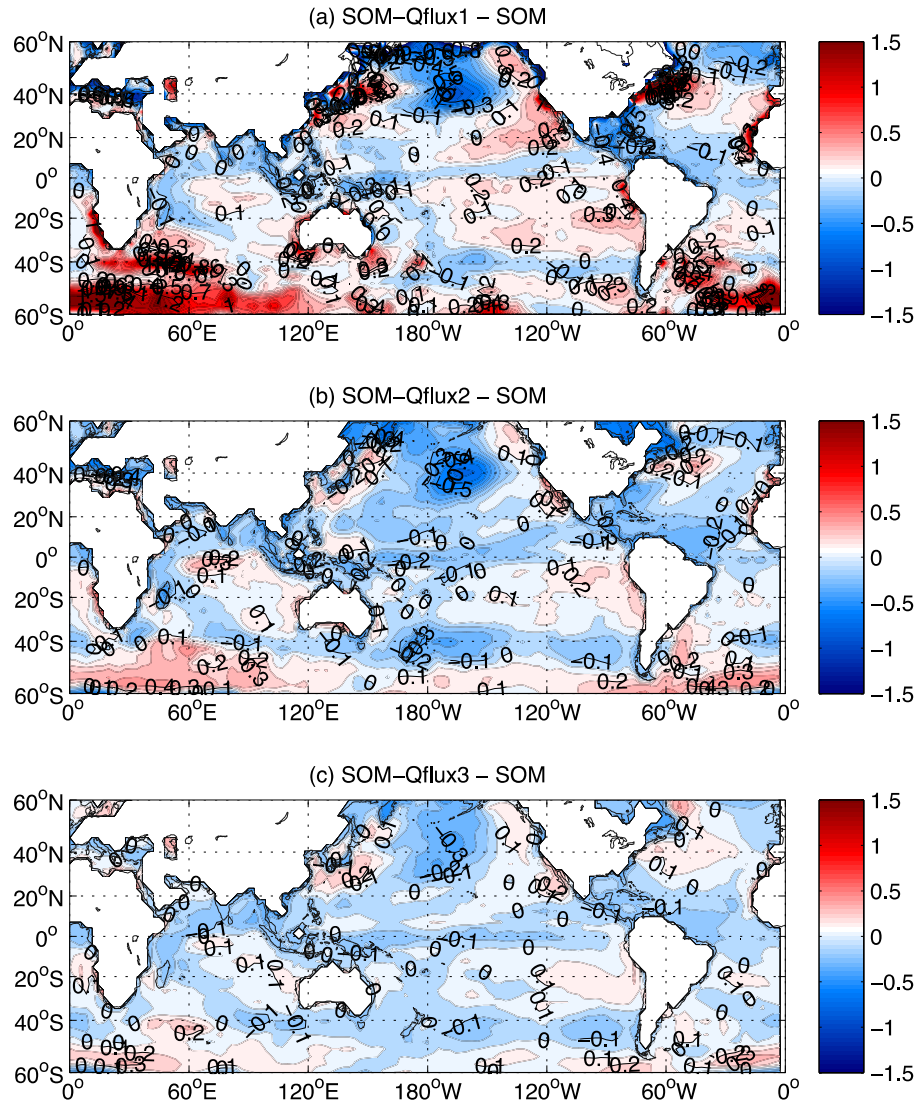
Figure 5.10. The difference of RMSE between the decadal predictions with adaptive Q-flux formulations and the SOM run. (a) SOM-Qflux1 – SOM, (b) SOM-Qflux2 – SOM and (c) SOM-Qflux3 – SOM. Unit: °C.

V.D. Conclusions

In this chapter, we investigated role of mean ocean heat transport in decadal predictability. In decadal prediction experiments using the slab ocean model, the ocean heat transport is represented by the Q-flux term, which is essentially a flux correction representing the missing ocean dynamics. In the decadal prediction run with fixed Q-flux for the 49 hindcasts analyzed previously (the SOM run), the predicted SSTs show a strong cooling bias in the early decades, with the cold SST bias decreasing from 1951 to 2000.

From the sensitivity experiments for the 1951 hindcast, discussed in the previous section, it was shown that the hindcasts with Q-flux generated using observed external forcings at 1951 gave a better prediction of global mean SST than hindcasts with Q-flux generated with observed external forcing at 1991. Due to the increase of external GHG forcings, the fixed Q-flux generated at 1991 external forcing level underestimated the mean ocean heat transport for the 1951 hindcast , resulting in a strong cooling bias. These sensitivity experiments suggested that for each hindcast, a different Q-flux should be used to represent the ocean heat transport that is consistent with the external GHG forcing for that initial condition.

To explore the sensitivity of decadal prediction skill to the Q-flux formulation. three sets of adaptive Q-flux patterns were generated to represent the ocean heat transport at each year from 1951 to 1999: Q-flux1 which uses a *fully adaptive,* time-varying formulation based only on the observed SST and external forcings over the 10 years preceding the initial condition; Q-flux2 which is *partially adaptive*, using

climatological SST but with external forcing set to its initial condition value, and Q-flux3, which is the average of Q-flux2 and the fixed Q-flux of the SOM run.

For the predictions of global mean SST, the strong cooling noted in the SOM run is eliminated in predictions using the adaptive Q-fluxes (Fig. 5.6, 5.7). The trend for the 1st year prediction to the 10th year prediction, as well as several other metrics such as the RMSE, are closer to the observations in decadal predictions with adaptive Q-fluxes. However, the correlation skill in the SOM run is still higher than that in the SOM-Qflux1 run and the SOM-Qflux2 run, due to the overestimated trends. But the prediction skill in the SOM-Qflux3 run is closer to that in the SOM run for the prediction lead times longer than 3 years (Fig. 5.7a). Moreover, the RMSE in the SOM-Qflux3 is considerably lower than that in the SOM run. Thus, predictions using the partially adaptive Q-flux3 formulation maintain the same correlation skill as the SOM run, but improve the RMSE, climatological mean, standard deviation and the trend. This implies that the decadal prediction with an adaptive Q-flux can give better prediction than the decadal prediction with fixed Q-flux, underscoring the importance of the mean ocean transport for decadal prediction. In order to have optimal skill for decadal predictions using a slab ocean model, the Q-flux should varied for each hindcast to represent the changes in ocean heat transport due to time-varying external forcing.

CHAPTER VI

SUMMARY AND CONCLUSIONS

This dissertation research addresses the influence of the mean state on climate variability at interannual and decadal time scales. In the atmosphere, there are many nonlinear variables, as well as nonlinear mechanisms. Hence, the superposition of climate anomalies on the mean state could result in a nonlinear response. For this study, we have focused on the vertical wind shear over the northern tropical Atlantic, which is considered as an important factor for hurricane development (DeMaria 1996; Goldenberg et al. 2001; Vecchi and Soden 2007), the surface wind speed, which is a critical factor for the Wind-Evaporation-SST (WES) feedback (Xie and Philander, 1994; Chang et al., 2001; Mahajan et al. 2009, 2010), as well as the role of the surface heat flux in affecting climate variability and predictability.

Vertical wind shear is conventionally defined as the magnitude of the wind vector difference between 850hPa and 200hPa. As hurricane activity is strongly impacted by the vertical wind shear, we focused on the tropical Atlantic hurricane season, from July to October. The ability of global climate models to simulate the observed variation of North Atlantic vertical wind shear is analyzed, using the suite of model integrations performed for the IPCC-AR4 assessment. At first, we examined the climatology of vertical wind shear in observations as well as coupled and uncoupled model simulations. It is found that coupled models tend to overestimate the strength of vertical wind shear over the northern tropical Atlantic, as a result of the tropical SST bias present in coupled

models. Compared to observations, the tropical SSTs simulated in the IPCC models are colder over the western tropical Atlantic warm pool (Richter et al. 2012), and warmer over the eastern tropical Pacific (Fig. 6.1). The warmer eastern tropical SST bias causes weaker Pacific Walker circulations, and leads to westerly anomalies over the tropical Atlantic (Vecchi et al. 2006). Hence, the vertical wind shear in coupled model tends to be stronger. Furthermore, the models with the strongest SST biases tend to have strongest tropical Atlantic vertical wind shear (Fig. 2.2).
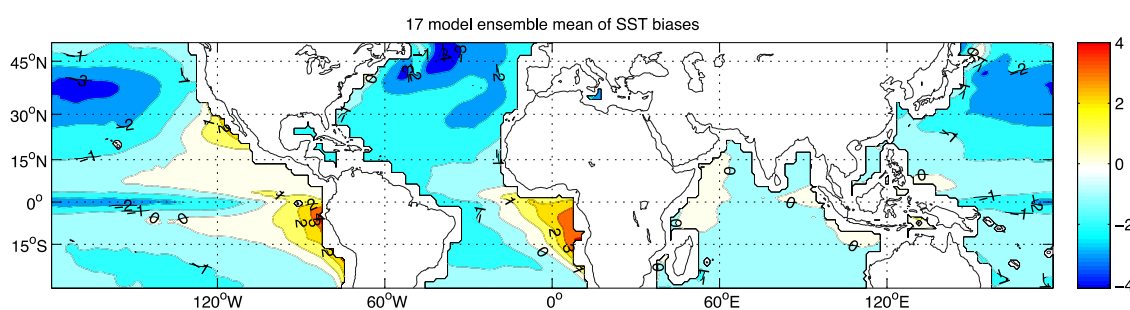
Figure 6.1. Ensemble mean of SST biases in the 17 IPCC models. Unit:C

The variability of vertical wind shear over the Main Development Region for Atlantic hurricanes is affected by local factors as well as the remote influence of the ENSO phenomenon, as noted in several observational and modeling studies (Goldenberg et al., 2001; Shame et al., 2009). When climate model simulations of the ENSO-shear relationship are compared to observations, it is found that the simulated ENSO-shear relationship in some uncoupled models, such as the CAM3 and the GFDL AM2, is of

opposite sign as compared to observations and coupled model simulations. The anomalous Walker cell response to ENSO is well simulated in the uncoupled models, but the mean zonal flow at 200hPa is easterly in the uncoupled atmospheric model simulations, whereas it is westerly in the observations. As a result of the nonlinear superposition of mean flow and anomalous flow when computing vertical wind shear, the ENSO-shear relationship in the uncoupled CAM3 integrations is opposite of that in observation. This indicates that the mean flow could significantly alter the ENSO-shear relationship, even though the anomalous upper level flow response to warm ENSO event is simulated correctly. The modulating effect of the mean flow is further verified using a simple linear regression model that captures many features of ENSO-shear relationship. This finding about the importance of mean flow reminds us that not only climate trends, but also the mean state bias should be considered when evaluating climate projections. Climate models with large climatological mean biases may need to be excluded for the estimation of vertical wind shear trends in the IPCC climate projections.

Analyzing the spatial and temporal characteristics of vertical wind shear variability, it is shown that the mean wind at 200hPa plays an important role. The JASO mean vertical wind shear over the northern tropical Atlantic exhibits a dipole mode, characterized by opposite variation of vertical wind shear in the southeastern and northwestern tropical Atlantic. This dipole mode of vertical wind shear variation is a robust feature at interannual and multi-decadal timescales, both in observations and in numerical model simulations. At interannual timescales, this dipole mode has a strong relationship to the remote SST forcing from the Pacific Ocean and the Indian Ocean. At

multi-decadal time scales, this dipole mode appears to have a weaker relationship to multi-decadal variations in the North Atlantic SST.

The dipole mode is shown to exist even during non-ENSO years and in uncoupled atmospheric model simulations forced by climatological annual cycle of SST. This suggests that the dipole mode of vertical wind shear over the northern tropical Atlantic could be an internal atmospheric mode, although its spatial structure shows some sensitivity to the presence of air-sea coupling. There are different prevailing upper level (200hPa) winds over the western and eastern tropical Atlantic. This means that even a monopolar mode of upper level wind variability can manifest itself as a dipolar mode of vertical wind shear, with opposite phase over the western and eastern tropical Atlantic. The study of vertical wind shear underscores the importance of climatological mean state for explaining the variation of nonlinear atmospheric variables.

To study the effect of surface wind speed, decadal prediction experiments were carried out using the CAM3 atmospheric model coupled to a slab ocean model, with simple projections of external forcings and using observed initial conditions. A set of 49 decadal predictions, each 10-year long, was carried out starting from January 1950 to January 1999. These decadal predictions exhibit significant skill when compared to persistence. In addition to numerical predictions, a modified version of Hasselmann's stochastic climate model is constructed and applied to decadal predictions. Unlike the classical Hasselmann model, which assumes a stationary climate, the modified Hasselmann model takes into account climate trends induced by the external forcings. The modified Hasselmann model also shows better prediction skill than persistence. This

decadal prediction system fills the gap between short-term climate predictions and the century-long projections (Smith et al. 2007; Meehl et al. 2009).

In order to study the influence of mean surface wind on decadal prediction, an additional set of decadal predictions was carried out, where the WES feedback was suppressed in CAM3 by prescribing the climatological annual cycle of the surface wind speed. It is found that the prediction skill for global mean SST is not sensitive to the presence of the WES feedback. However, examining the spatial pattern of decadal prediction skill, it is found that in the eastern tropical Pacific SST, suppressing the WES feedback improves the predication skill. This improvement in skill is associated with an increased signal-to-noise ratio as well as increased correlations between the simulated and observed latent and sensible heat flux. Using the modified Hasselmann model to diagnose decadal predictions of the numerical model, it is found that switching off the WES feedback reduces the damping coefficient, thus leading to increased persistence of the initial signal. This suggests that by prescribing the climatological mean surface wind, the damping of the initial perturbation can be mitigated, especially over the tropical Pacific, thus reducing the uncertainty arising from internal variability.

During the analysis of the decadal prediction experiments using the slab ocean model coupled to CAM3, it was noticed that the Q-flux term, which represents oceanic heat transport in the slab ocean model, had a significant impact on systematic errors in the prediction. In particular, decadal predictions with earlier start dates (say 1950) exhibited a strong cooling bias. To further investigate the role of the mean oceanic heat

transport, three additional sets of decadal prediction sensitivity experiments were carried out using *adaptive* formulations for the Q-flux that varied with initial conditions.

Comparing the decadal prediction using the adaptive Q-fluxes to the control prediction experiment using the fixed Q-fluxes, it is found that the RMSE is reduced significantly when an adaptive Q-flux formulation is used. This improvement in prediction skill implies that unlike decadal prediction carried out using fully coupled models (e.g., Smith et al. 2007), decadal prediction using the slab ocean model needs to take explicitly into account the change of ocean heat transport.

REFERENCES

Aiyyer, A. R. and C. Thorncroft, 2006: Climatology of vertical wind shear over the tropical atlantic. *J. Climate*, **19**, 2969–2983.

Aiyyer, A. R. and C. Thorncroft, 2011: Interannual-to-Multidecadal Variability of vertical shear and tropical cyclone activity. *J. Climate*, **24**, 2949-2962.

Bengtsson, L., K. Hodges, M. Esch, N. Keenlyside, L. Kornblueh, J. J. Luo, and T. Ya- magata, 2007: How may tropical cyclones change in a warmer climate? *Tellus*, **59A**, 539–561.

Bitz, C. M., K. M. Shell, P. R. Gent, D. A. Bailey, G. Danabasoglu, K. C. Armour, M. M. Holland and L. T. Kiehl, 2012: Climate sensitivity of the community climate system model, version 4. *J. Climate*, **25**, 3053-3070

Boer, G. J. and S. J. Lambert, 2008: Multi-model decadal potential predictability of precipitation and temperature, *Geo. Res. Lett.*, **35**, L05706

Bretherton, C. S., C. Smith, and J. M. Wallace, 1992: An intercomparison of methods for finding coupled patterns in climate data. *J. Climate*, **5**, 541–560.

Chang, P., L. Ji and H. Li, 1997: A decadal climate variation in the tropical Atlantic ocean from thermodynamic air-sea interactions, *Nature,* **385**,517-518

Chang, P., L. Ji, and R. Saravanana, 2001: A hybrid coupled model study of tropical Atlantic Variability, *J. Climate*, **14**, 361-390.

Chiang, J. C. H. and C. Bitz, 2005: Influence of high latitude ice cover on the marine intertropical convergence zone. *Climate Dynamics*, **25**, 477-496.

Cole, J. E. and E. R. Cook, 2012: The changing relationship between ENSO variability and moisture balance in the continental united States, *Geophy. Res. Lett.*, **25**, 4529-4532

DeMaria, M., 1996: The effect of vertical shear on tropical cyclone intensity change. *J. Atmos. Sci.*, **54**, 2076-2087.

Donnelly, J. P. and J. D. Woodruff, 2007: intense hurricane activity over the past 500 years controlled by El Nino and the west African monsoon. *Nature*, **447**, 465–468.

Elsner, J. B., B. H. Bossak, and X. Niu, 2001: Secular changes to the enso-us hurricane relationship. *Geophy. Res. Lett.*, **28**, 4123–4126.

Emanuel, K., 2005: Increasing destructiveness of tropical cyclones over the past 30 years. *Nature*, **436**, 686–688.

Emanuel, K., R. Sundararajan, and J. Williams, 2008: Hurricanes and global warming. *Bull. Amer. Meteor. Soc.*, **89**, 347–367.

Frankignoul, C., and K. Hasselmann, 1977: Stochastic Climate models, Part II: Application to sea-surface temperature anomalies and thermocline variability. *Tellus*, **29**, 289-305

Garner, S. T., I. M. Held, T. Knutson, and J. Sirutis, 2009: The role of wind shear and thermal stratification in past and projected changes of Atlantic tropical cyclone activity. *J. Climate*, **22**, 4723–4734.

Giannini, A., R. Saravanan, and P. Chang, 2003: Oceanic forcing of Sahel rainfall on interannual to interdecadal time scales. *Sciences*, **302**, 1027–1030.

Goldenberg, S. B., C. Landsea, A. M. Mestas-Nunez, and W. M. Gray, 2001: The recent

increase in Atlantic hurricane activity. *Science*, **293**, 474-479.

Goldenberg, S. B. and L. J. Shapiro, 1996: Physical mechanisms for the association of El Nino and West African rainfall with Atlantic major hurricane activity. *J. Climate*, **9**, 1169-1187.

Gray, W. M., 1984: Atlantic seasonal hurricane frequency. Part I: El Nino and 30mb quasi-biennial oscillation influences. *Mon. Weather Rev.*, **112**, 1649-1668.

Hastenrath, S., 2000: Interannual and longer term variability of upper-air circulation over the tropical Atlantic and west Africa in boreal summer. *Int. J. of Climatol.*, **20**, 1415–1430.

Honda, Meiji, Shozo Yamane, Hisashi Nakamura, 2005: Impacts of the Aleutian–Icelandic Low Seesaw on Surface Climate during the Twentieth Century. *J. Climate*, **18**, 2793–2802.

Jordi, Antoni, Sultan Hameed, 2009: Influence of the Icelandic Low on the Variability of Surface Air Temperature in the Gulf of Lion: Implications for Intermediate Water Formation. *J. Phys. Oceanogr.*, **39**, 3228–3232.

Kalnay, E., et al., 1996: The NCEP/NCAR 40-year reanalysis project. *Bull. Amer. Meteo. Soc.*, **77**, 437-470.

Kawano, T., 2011: Trends in observation and research of deep ocean circulation and heat transport. *Quarterly Review*, **39**, 65-76

Kay, J. E., M. H. Holland, C. M. Bitz, E. Blanchard-Wrigglesworth, A. Gettelman, A. Conley and D. Bailey, 2012: The influence of Local feedbacks and northward heat transport on the equilibrium Arctic climate response to incrased greenhouse gas

forcing. *J. Climate*, **25**, 5433-5450

Kerr, R. A., 2000: A north Atlantic climate pacemaker for the centuries. *Sciences*, **288**, 1984-1986.

Kerr, R., 2003: Warming Indian Ocean wringing moisture from the Sahel. *Sciences*, **302**, 210-211.

Kiehl, J. T., J. J. Hack, G. B. Bonan, B. A. Boville, B. P. Briegleb, D. L. Williamson, and P. J. Rasch, 1996: Description of the NCAR community climate model. *Technical Note TN-420+SR, NCAR*

Klein, S. A., B. J. Soden, and N.-C. Lau, 1999: Remote sea surface temperature variations during ENSO: Evidence for a tropical atmospheric bridge. *J. Climate*, **12**, 917-932.

Knight, J. R., R. J. Allan, C. K. Folland, M. Vellinga, and M. E. Mann, 2005: A signature of persistent natural thermohaline circulation cylcones in observed climate. *Geophys. Res. Lett.*, **32**, L20 708.

Knight, J. R., C. K. Folland, and A. A. Scaife, 2006a: Climate impacts of the Atlantic multidecadal oscillation. *Geophy. Res. Lett.*, **33**, L17 706.

Knight, J. R., C. K. Folland, and A. A. Scaife, 2006b: Climate impacts of the Atlantic multidecadal oscillation. *Geophy. Res. Lett.*, **33**, L17 706.

Kossin, J. P. and D. J. Vimont, 2007: A more general framework for understanding Atlantic hurricane variability and trends. *Bull. Amer. Meteor. Soc.*, **88**, 1767-1781.

Landsea, C. W., C. Anderson, N. Charles, G. Clark, J. Dunion, J. Fernandez-Partagas, P. Hungerford, C. Neumann, and M. Zimmer, 2004: The Atlantic hurricane database re-

analysis project: Documentation for the 1851-1910 alterations and additions to the HURDAT database. *Hurricanes and Typhoons: Past, Present and Future*, R. J. Murname and K.-B. Liu, Eds., Columbia University Press, 177-221

Latif, M., N. Keenlyside, and J. Bader, 2007: Tropical sea surface temperature, vertical wind shear, and hurricane development. *Geophy. Res. Lett.*, **34**, L01 710.

Madden, R. A. and P. P. Julian, 1994: Observations of the 40-50-day tropical oscillation – a review, *Monthly weather review*, **122**, 814-836

Mahajan, S., R. Saravanan, and P. Chang, 2009: The role of the wind-evaporation-sea surface temperature feedback in air-sea coupled tropical variability. *Atmospheric Research*, **94**, 19-36.

Mahajan, S., R. Saravanana, and P. Chang, 2010: Free and forced variability of the tropical Atlantic Ocean: Role of the wind-evaporation-sea surface temperature feedback. *J. Climate*, **23**, 5958-5977.

Meehl, G. A., L. Goddard, and coauthors, 2009: Decadal prediction: can it be skillful? *Bull. Ame. Met. Soc.*, **90**, 1467-1485

North, G. R., T. L. Bell, R. F. Cahalan and F. J. Moening, 1982: Sampling errors in the estimation of Empirical Orthogonal Functions. *Monthly Weather Review*, **110**, 699 – 706

Palmer, T. N., 1986: Influence of the Atlantic, Pacific and Indian oceans on Sahel rainfall. *Nature*, **322**, 251–253.

Philander, S. G., 1990: El Nino, La Nina and the Southern Oscilation. *International geophysics series*, Volume **46**.

Philip, S. and G. J. Van Oldenborgh, 2009: Significant atmospheric nonlinearities in the ENSO cycle. *J. Climate*, **22**, 4014-4028

Pielke, J. R. A. and C. N. Landsea, 1999: La Nina, El Nino and Atlantic hurricane damages in the United States. *Bull. Amer. Meteor. Soc.*, **80**, 2027-2033.

Rayner, N. A., D. E. Parker, E. B. Horton, C. K. Folland, L. V. Alexander, D. P. Rowell, E. C. Kent, and A. Kaplan, 2003: Global analyses of sea surface temperature, sea ice and night marine air temperature since the late nineteenth century. *J. Geophys. Res.*, **108**, 4407.

Richter, I. and S.-P. Xie, 2008: On the origin of equatorial Atlantic biases in coupled general circulation models, *Climate Dynamics*, **31**, 587-598

Richter, I., S.-P. Xie, A. T. Wittenberg and Y. Masumoto, 2012: tropical Atlantic biases and their relationship to surface wind stress and terrestrial precipitation. *Climate Dynamic*, **38**, 985-1001

Ropelewski, C. F., M. S. Halpert, 1986: North American Precipitation and Temperature Patterns Associated with the El Niño/Southern Oscillation (ENSO). *Mon. Wea. Rev.*, **114**, 2352–2362

Saravanan, R. and P. Chang, 1999: Oceanic mixed layer feedback and tropical Atlantic variability. *Geophys. Res. Lett.*, **26**, 3629-3632.

Saravanan, R. and P. Chang, 2004: Thermodynamic coupling and predictability of tropical sea surface temperature. *Earth's climate: The Ocean-Atmosphere Interaction*, C. Wang and S.-P. Xie and J. A. Carton (Eds.), *Geophysical Monograph*, No. 147, American Geophysical Union, 171-180.

Saunders, M. A. and A. S. Lea, 2008: Large contribution of sea surface warming to recent increase in Atlantic hurricane activity. *Nature*, **451**, 557–560.

Shaman, J., S. K. Esbensen, and E. D. Maloney, 2009: The dynamics of the ENSO-Atlantic hurricane teleconnection: Enso-related changes to the north African-Asian jet affect Atlantic basin tropical cyclogenesis. *J. Climate*, **22**, 2458-2482.

Smirnov, D. and D. J. Vimont, 2010: Variability of the Atlantic meridional mode during the Atlantic hurricane season. *J. Climate*, **29**,1402-1424

Smith, Shawn R., Justin Brolley, James J. O'Brien, Carissa A. Tartaglione, 2007: ENSO's Impact on Regional U.S. Hurricane Activity. *J. Climate*, **20**, 1404–1414.

Smith, D. M., S. Cusack, A. W. Colman, C. K. Folland, G. R. Harris and J. M. Murphy, 2007: Improved surface temperature prediction for the coming decade from a global climate model. *Science*, **317**, 796-799

Tang, B. H. and J. D. Neelin, 2004: Enso influence on Atlantic hurricanes via troposhpheric warming. *Geophy. Res. Lett*., **21**, L2404.

Trenberth, K.E. and J.W. Hurrell, 1994: Decadal atmosphere-ocean variations in the Pacific. *Climate Dynamic,* **9**, 303-319.

Trenberth, K. E. and J. M. Caron, 2001: Estimates of meridional atmosphere and ocean heat transport. *J. Climate*, **14**, 3433-3443

Uppala, S. M. and Coauthors, 2005: The ERA-40 reanalysis. *Q. J. R. Meteorol. Soc.*, **131**, 2961-3012.

Vecchi, G. A., B. J. Soden, A. T. Wittenberg, I. M. Held, A. Leetmaa and M. J. Harrison, 2006: Weakening of tropical Pacific atmospheric circulation due to

anthropogenic forcing, *Nature*, **441**, 73-76

Vecchi, G. A. and B. J. Soden, 2007a: Effect of remote sea surface temperature change on tropical cyclone potential intensity. *Nature*, **450**, 1066–1070.

Vecchi, G. A. and B. J. Soden, 2007b: Increased tropical Atlantic wind shear in model projections of global warming. *Geophys. Res. Lett*., **34**, L08702.

Vecchi, G. A. and T. R. Knutson, 2008: On estimates of historical north Atlantic tropcical cyclone activity. *J. Climate*, **21**, 3580–3600.

Wallace, J. M. and P. V. Hobbs, 2006: Atmospheric sciences, an introductory survey, second edition.

Wallace, J. M., C. Smith, and C. S. Bretherton, 1992: Singular value decomposition of wintertime sea surface temperature and 500-mb height anomalies. *J. Climate*, **5**, 561–576.

Wang, C., S.-K. Lee, and D. B. Enfield, 2008: Atlantic warm pool acting as a link between Atlantic multidecadal oscillation and Atlantic tropical cyclone activity. *Geochemistry Geophysics Geosystems*, **9**, doi:10.1029/2007GC001 809.

Wheeler, M. C. and H. H. Hendon, 2004: An all-season real-time multivariate MJO index: development of an index for monitoring and prediction. *Monthly Weather review*, **132**, 1917-1932

Xie, S.-P., 1994: On the genesis of the equatorial annual cycle. *J. Climate*, **7**, 2008-2013.

Xie, S.-P., 1996: Westward propagation of latitudinal asymmetry in a coupled ocean-atmosphere model. *J. Atmos. Sci.*, **53**, 3236-3250.

Xie, S.-P., 1999: A dynamic ocean-atmosphere model of the tropical Atlantic decadal variability: Interhemispheric tropical-Extratropical, and cross-basin interactions. *J. Climate*, **20**, 856-870.

Xie, S.-P. and S. Philander, 1994: A coupled ocean-atmosphere model of relevance to the ITCZ in the eastern Pacific. *Tellus*, **46A**, 340-350

Xie, S.-P., C. Deser, G. A. Vecchi, J. Ma, H. Teng and A. T. Wittenberg, 2010: Global warming pattern formation: sea surface temperature and rainfall, *J. Climate*, **23**, 966-986.

Yang, J., Q. Liu, S. Xie, Z. Liu, and L. Wu, 2007: Impact of the Indian ocean SST basin mode on the Asian summer monsoon. *Geophy. Res. Lett.*, **34**, L02 708.

Yang, X., A. Rosati, S. Zhang, T. L. Delworth, R. G. Gudgel, R. Zhang, G. Vecchi, W. Anderson, Y.-S. Chang, T. Delsole, K. Dixon, R. Masadek, W. F. Stern, A. Wintternberg and F. Zeng, 2013: A predictable AMO-like Pattern in the GFDL fully coupled ensemble initialization and decadal forecasting system. *J. Climate*, **26**, 650-661.

Zhang, R. and T. L. Delworth, 2006: Impact of Atlantic multidecadal oscillations on India/Sahel rainfall and Atlantic hurricanes. *Geophys., Res. Lett.*, **33**, L17 712.

Zhu, X., J. Sun, Z. Liu, Q. Liu and J. E. Martin, 2007: A synoptic analysis of the interannual variability of winter cyclone activity in the Aleutian Low region. *J. Climate*, **20**, 1523-1538

Zhu, X. and Z. Liu, 2009: Tropical SST response to Global warming in the twentieth century, *Journal of Climate*, Vol. 22, 1305-1312

Zhu, X., R. Saravanan and P. Chang, 2012: Influence of mean flow on the ENSO-Vertical wind shear relationship over the northern tropical Atlantic. *J. Climate*, **25**, 858-864.